High-power frequency combs for precision spectroscopy in the extreme ultraviolet

Haydar Sarper Salman

Universität Hamburg
DER FORSCHUNG | DER LEHRE | DER BILDUNG

Hamburg 2023

High-power frequency combs for precision spectroscopy in the extreme ultraviolet

Dissertation

zur Erlangung des Doktorgrades
an der Fakultät für Mathematik, Informatik und
Naturwissenschaften
Fachbereich Physik der
Universität Hamburg

vorgelegt von
Haydar Sarper Salman
aus
Dinar, Türkei

Hamburg
2023

Gutachter der Dissertation:	Dr. Christoph M. Heyl Prof. Dr. Franz X. Kärtner
Zusammensetzung der Prüfungskommision:	Prof. Dr. Arwen R. Pearson Prof. Dr. Nina Rohringer Prof. Dr. Tobias Herr Prof. Dr. Franz X. Kärtner Dr. Christoph M. Heyl
Vorsitzende der Prüfungskommision:	Prof. Dr. Arwen R. Pearson
Datum der Disputation:	01. November 2023
Vorsitzender des Fach-Promotionsausschusses PHYSIK:	Prof. Dr. Günter H. W. Sigl
Leiter des Fachbereichs PHYSIK:	Prof. Dr. Wolfgang J. Parak
Dekan der Fakultät MIN:	Prof. Dr.-Ing. Norbert Ritter

Eidesstattliche Erklärung
Declaration on oath

Hiermit erkläre ich an Eides statt, dass ich die vorliegende Dissertationsschrift selbst verfasst und keine anderen als die angegebenen Quellen und Hilfsmittel benutzt habe.

I hereby declare upon oath that I have written the present dissertation independently and have not used further resources and aids than those stated in the dissertation.

Hamburg, July 2023

Haydar Sarper Salman

Abstract

Ultra-high-resolution spectroscopy provides the basis behind multiple scientific fields and in particular, for frequency metrology. The required techniques usually involve optical frequency combs, which are well established in the visible and infrared spectral regions. In contrast, the Vacuum- and Extreme Ultraviolet (VUV and XUV) are barely explored spectral ranges, mainly due to the lack of a suitable light source. However, many atoms and in particular ions of fundamental interest await to be analyzed. Additionally, prospective nuclear clocks based on optically driving the low energy ^{229}Th nuclear transition (about 8.3 eV), set high demands on dedicated VUV sources. A possible solution can be provided by high-power frequency combs combined with cavity-enhanced high-harmonic generation (HHG). However, this combination represents a highly complex approach with great challenges if long-term stable, low-noise operation is required. This is particularly important should ultra-narrow transitions such as the ^{229}Th transition be targeted. This dissertation addresses these challenges, describing the complete development of a fully-stabilized high-power femtosecond frequency comb centered at 1 µm wavelength with 65 MHz comb line spacing and more than 70 W output power. Furthermore, important features including a new oscillator design, wavelength tuning, adaptation for remote computer control and a technical interlock, which ensures fail-safe and stable long-term operation of the system, are implemented. The dissertation shows for the first time that a fully-stabilized high-power frequency comb can be operated continuously over multiple days without interruption, setting the stage for VUV conversion and ultra-high-resolution spectroscopy in this spectral region.

Zusamenfassung

Die ultrahoch auflösende Präzisionsspektroskopie bildet das Fundament mehrerer Wissenschaftsfelder und insbesondere für die Frequenzmetrologie. Die dafür angewendeten Techniken nutzen üblicherweise optische Frequenzkämme, die sich im sichtbaren und nahen infraroten Spektralbereich etabliert haben. Im Gegensatz dazu sind Vakuum- und Extremultraviolett (VUV und XUV) kaum erforschte Spektralbereiche; Grund dafür ist das Fehlen einer geeigneten Lichtquelle. Allerdings warten gerade dort Atome und Ionen auf Analyse, die von fundamentalem Interesse ist. Weiterhin gibt es die Aussicht auf Kernuhren auf Basis des niedrigenergetischen ^{229}Th Kernübergangs, ein Unterfangen, das hohe Ansprüche an dafür notwendige VUV-Quellen stellt. Eine mögliche Herangehensweise kann aus einer Kombination aus einem Hochleistungsfrequenzkamm und resonatorgetriebener Generation hoher Harmonischer (HHG) bestehen. Dieser Ansatz ist hochkomplex, er beinhaltet große Herausforderungen wie Lang- und Kurzzeitstabilität und ultrarauscharmen Betrieb. Das ist besonders wichtig wenn schmalbandige Übergänge wie der ^{229}Th-Übergang angeregt werden sollen. Diese Dissertation adressiert diese Herausforderungen und beschreibt die komplette Entwicklung eines vollständig stabilisierten Hochleistungsfrequenzkamms mit einer Zentralwellenlänge von 1 µm, einem Kammlinienabstand von 65 MHz und mehr als 70 W Ausgangsleistung. Weiterhin werden wichtige Merkmale einschließlich einer neuartigen Oszillatorarchitektur, Wellenlängendurchstimmbarkeit, Anpassung für computerbasierte Steuerung und ein technisches Interlocksystem für ausfallsicheren und langfristigen Betrieb implementiert. Diese Dissertation zeigt damit erstmals, dass ein vollständig stabiliserter Hochleistungsfrequenzkamm über Tage ununterbrochen betrieben werden kann und öffnet damit neue Möglichkeiten für die VUV-Konversion und damit für die Ultrahochpräzisionsspektroskopie in diesem Spektralbereich.

Contents

List of Figures

List of Tables

List of Abbreviations

AOI	angle of incidence
AOM	acousto-optic modulator
APC	amplifier protection circuit
APD	avalanche photodiode
ccw	counter-clockwise
CEO	carrier-envelope offset
CFBG	chirped fiber Bragg grating
CPA	chirped pulse amplification
CPS	cladding power stripper
Cs	Cesium
CW	continous-wave
cw	clockwise
DCF	dispersion compensation fiber
DM	dichroic mirror
EOM	electro-optic modulator
FPGA	field programmable gate array
FROG	frequency resolved optical gating
fsEC	femtosecond enhancement cavity
FWHM	full width at half maximum
GDD	group-delay dispersion
GPS	global positioning system
GVD	group-velocity dispersion
HHG	high-harmonic generation
HNLF	highly nonlinear fiber
HWP	half waveplate

KLM	Kerr-lens mode-locking
MLL	mode-locked laser
MMF	multi-mode fiber
MOSFET	metal-oxide-semiconductor field-effect transistor
MPC	multi-pass cell
MPSC	multi pump and signal combiner
NA	numerical aperture
NALM	nonlinear amplifying loop mirror
NHM	nuclear hyperfine mixing
NOLM	nonlinear optical loop mirror
NPRO	non-planar ring oscillator
NSE	nonlinear Schrödinger equation
OFC	optical frequency comb
PAS	phase and amplitude shaper
PBS	polarizing beam splitter
PCB	printed circuit board
PCF	photonic-crystal fiber
PD	photodiode
PDH	Pound-Drever-Hall
PER	polarization extinction ratio
PID	proportional-integral-derivative
PLC	programmable logic controller
PLL	phase-locked loop
PM	polarization maintaining
PPLN	periodically poled lithium niobate
PPS	pulse per second
PSD	power spectral density
PZT	piezoelectric actuator
QWP	quarter waveplate
RBW	resolution bandwidth
RF	radio frequency
RIN	relative intensity noise
RMS	root-mean-square

SA	saturable absorber
SBS	stimulated Brillouin scattering
SESAM	semiconductor saturable absorber
SI	International System of Units
SMF	single-mode fiber
SPM	self-phase modulation
SRS	stimulated Raman scattering
SSA	signal source analyzer
TMI	transverse mode instabilities
TOD	third-order dispersion
VCO	voltage-controlled oscillator
VUV	vacuum ultraviolet
WDM	wavelength division multiplexer
XGM	cross-gain modulation

1 Introduction

The history of lasers dates back to the Nobel Prize-winning discovery of energy quanta by Max Planck in the early 20th century [1]. In his work, Planck studied the relationship between energy and the frequency of radiation, concluding that energy can only be emitted and absorbed in discrete chunks, which he called *quanta*. His theory inspired many physicists, including Albert Einstein, who published a paper on the photoelectric effect in 1905 [2], suggesting that light transmits its energy as quanta, in this case discrete quantum particles, called *photons*. Moreover, in 1917 Einstein suggested that, in addition to spontaneous absorption and emission, electrons could be stimulated to emit light of a specific wavelength [3].

In 1951, Charles Townes laid the theoretical foundation for the *maser* (microwave amplification by stimulated emission of radiation) proposing a new way to generate coherent radiation based on Einstein's predictions. Following this idea, Townes, together with Herbert Zeiger and James Gordon, implemented the first ammonia based maser. Although Gordon Gould theorized in the 1950s that stimulated emission could be used to amplify light and called it a *laser*, the first working laser prototype was built by Theodore Maiman in 1960 [4]. Maiman's laser used a synthetic ruby as the active medium, which also served as the laser cavity, by silver coating the surfaces of the ruby. It could be used as a Fabry-Perot resonator, and emit coherent light at a wavelength of 694.3 nm. After the first demonstration of the laser, its progress and applications accelerated rapidly.

Especially the telecommunications industry advanced the development of pulsed laser technology. The first implementation of a pulsed laser was achieved by placing a mechanical chopper in the beam path of a continuous wave laser. It was soon discovered, that so-called giant pulses could be generated by manipulating the reflective surfaces at the end of the active medium with a method called Kerr-cell switching [5]. Here, a fast attenuator initially generates a high level of loss in the cavity (low Q-factor), which magnifies the population inversion, then the attenuator is suddenly turned off (high Q-factor), which leads to the release of all stored energy and subsequently a short pulse. The typical pulse duration of Q-switched lasers is in the nanosecond range. The mode-locking technique [6] enabled the generation of even shorter pulses in the regime of picoseconds or less. In particular, the use of Ti:Sapphire crystals [7] as a laser gain medium has made it possible to achieve pulses shorter than 100 fs at the cavity output [8]. While for some applications the output pulse energies of Ti:Sapphire lasers of a few nanojoules are sufficient, other applications require higher energies. The intuitive way of amplification to reach higher

pulse energies is to add another optically pumped Ti:Sapphire to the system. However, there is a limit to the amplification caused by high intensities inside the crystal as a result of nonlinear processes such as self-focusing, which results in damage to the crystal. The demonstration of chirped-pulse amplification (CPA) by Donna Strickland and Gerard Mourou in 1985 [9], a Nobel Prize-winning technique, provided a concrete path to ultrafast laser amplification, which alleviated the self-focusing problem to some extent. The CPA technique relies on stretching ultrafast pulses in time before amplification to reduce peak power and hence nonlinearities. After amplification, they are compressed back to their input duration, resulting in peak powers that are orders of magnitude higher than initially.

Soon after the first demonstration of lasers by Maiman, fiber lasers were proposed and studied as a promising laser configuration [10], [11]. Although again first introduced and optimized for optical telecommunications [12], today fibers are used as various laser elements such as optical cavities, waveguides, active media and even optical pumps. Due to their geometry and high surface-to-volume ratio, fibers can steer light steadily over very long distances. Due to technological advancements enabling the production of highly-doped active fibers, it is not only possible to build simple laser oscillators, but also reach high-power outputs using double-clad fibers [13]. Today, continuous wave fiber lasers can reach more than 10 kW of average optical power, while ultrafast fiber lasers have entered the kW range [14].

Optical frequency combs (OFCs) [15], [16] were first developed by John Hall and Theodor Hänsch to support optical atomic clocks, enabling absolute frequency referencing between the optical and the radio frequency (RF) regimes. However, they quickly found many more applications, such as trace gas detection [17], ranging [18], molecular fingerprinting [19], optical communication [20] and calibration of atomic spectrographs [21]. OFCs are phase-stabilized mode-locked lasers and can be realized by stabilizing two degrees of freedom; the carrier envelope offset frequency and the pulse repetition frequency. The mode-locked optical spectrum has attractive features useful for precision optical metrology, such as all optical modes being equidistant in frequency and phase-coherent with each other. As a result, the phase and frequency dynamics of each optical mode in the OFC spectrum are deterministic. Thus, determining the absolute frequency of any mode is only possible with knowledge of the absolute frequency of a mode.

Clocks are essential for any time-dependent process and have played a major role in the development of humanity. The history of clocks begins with obelisks and sundials dating back to 3500 BC and 1500 BC, respectively. While their accuracy is not comparable to the advanced clocks we use today, the two main ingredients remain unchanged. First, a system that provides a regular periodic event with a fixed frequency is required. This system serves as a stable frequency reference. Second, counting the cycles of this periodic event or fixed frequency reference, which forms the basis of the corresponding timescale. In the past, frequency standards were based on celestial observations, but there was a dramatic

change in precision in the mid-1950s with the introduction of the *cesum atomic clock* [22]. In 1967, the International System of Units (SI) standardized the second according to the properties of cesium (Cs), where one second is defined as 9 192 631 770 cycles of radiation, reaching a fractional frequency uncertainty of almost 10^{-12}. Atomic clocks are based on the resonant interaction of atoms with a microwave, where the interacting atoms change their energy state. The detector placed after the interaction, counts only those atoms that have changed their energy state. The information is fed back to the microwave source and the microwave frequency is synchronized with the highest number of atoms, whose energy state has changed. For ^{133}Cs atom, the resonant frequency for the relevant hyperfine transition is $\approx 9.19\,\mathrm{GHz}$. Today, a state-of-the-art Cs fountain clocks reaches a fractional frequency uncertainty of 10^{-16} [23], reaching its practical limits.

To overcome this limit, a new type of clock that uses optical frequencies instead of microwaves was introduced, the optical atomic clock. The benefit of using higher frequencies can be explained by the clock instability σ_y [24]; $\sigma_y(\tau) \propto \frac{\Delta\nu}{\nu_0}$, where $\Delta\nu$ is the spectroscopic linewidth of the clock system, ν_0 is the absolute frequency. From the clock instability formula, it is easy to conclude that the instability can be reduced by increasing the absolute frequency. However, there was no way to detect optical frequencies using standard electronics, so there was no way to measure the absolute frequency, except with a very complex chain of frequency synthesizers and an array of phase-locked oscillators. OFCs mitigated this and ultimately served as a bridge, by linking optical frequencies to the microwave regime. Shortly after the introduction of OFCs, they became standard tools for frequency metrology. Today, optical lattice clocks using OFCs as frequency synthesizers are the most precise clocks, achieving frequency uncertainties of 10^{-18} [25], [26]. Optical clocks, like atomic clocks, use an oscillator fixed to an atomic resonance, but unlike atomic clocks the oscillator is optical, typically a laser. Counting is also done differently, instead of using a frequency counter, optical atomic clocks count using an OFC that reduces optical frequencies to countable microwave signals. A depiction of an optical atomic clock is provided in Fig. 1.1.

To push the limits of state-of-the-art optical clocks, another type of clock has been proposed - the nuclear clock. Conceptually, instead of driving atomic shell transitions, it is proposed to use a nuclear transition. Nuclear transitions provide three advantages [27]: First, the nucleus is five orders of magnitude smaller than the atomic shell, so it is less affected by external disturbances leading to higher stability. Second, the transition frequencies are higher, resulting in less clock instability. Finally, the nuclei density is much larger compared to that of the atomic shell, resulting in improved statistical uncertainties for solid-state nuclear clocks based on Mössbauer spectroscopy. Given the advantages listed above, nuclear clocks are expected to improve frequency uncertainty by at least one order of magnitude compared to optical atomic clocks. In addition, opening the door to probing nuclear transitions with a laser is expected to unlock entirely new possibilities for nuclear physics as this would enable highly accurate characterization of atomic nuclei.

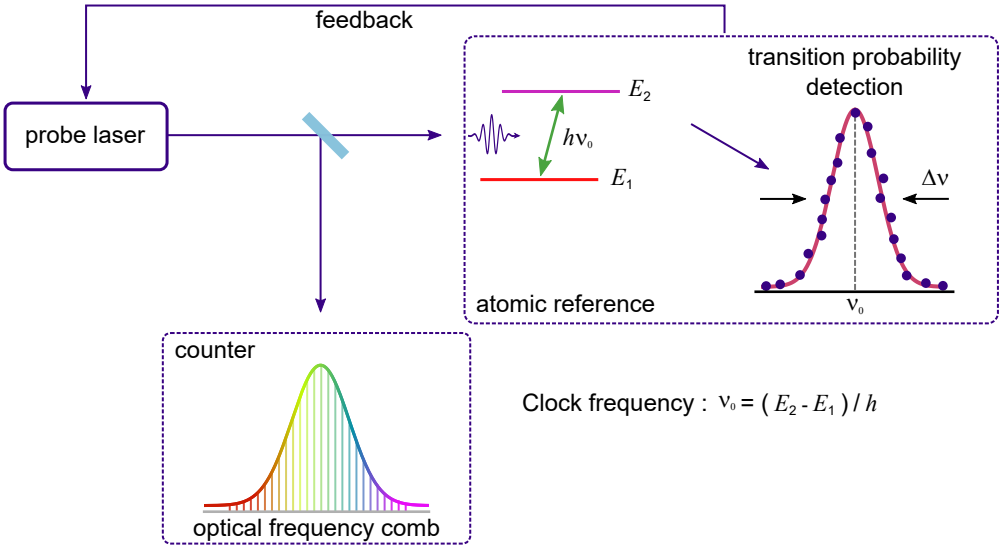

Figure 1.1: Schematic of an optical atomic clock. The probe laser is in resonance with an atomic transition. From the atomic reference, a feedback signal is obtained that corrects the output of the probe laser to match the resonance frequency. The optical frequency comb acts as an optical counter that down-counts optical frequencies to microwave signals.

Considering current available technology, transition energy and lifetime, there is only one viable candidate for direct laser probing of a nuclear transition, the ^{229}Th nuclear isomer [28], [29]. From the most recent studies [30], the low-energy transition of the ^{229}Th nuclear isomer is $8.338 \pm 0.024\,\mathrm{eV}$ measured via vacuum ultraviolet (VUV) spectroscopy of the radiative decay revealing a lifetime of 10^4 s. This transition energy corresponds to $148.7 \pm 0.43\,\mathrm{nm}$. Direct laser excitation of this transition requires a VUV OFC. Today, VUV OFCs rely on highly inefficient high-order optical frequency conversion processes, such as harmonic generation in gases [31]. To carry out this highly nonlinear frequency conversion process, a high-power solid-state (or fiber) laser frequency comb with a pulse repetition rate of typically 100 MHz is required, followed by an femtosecond enhancement cavity (fsEC) for in-cavity high-harmonic generation (HHG). While Ti:sapphire laser systems were proposed as driving laser sources too [32], [33], Yb-fiber laser systems provide many advantages including in particular much higher average powers [34]–[36].

It is important to note that OFCs are attractive sources for spectroscopy and have a multitude of appliances. In turn, spectroscopy is a fundamental measuring technique, which is flexibly used across many scientific fields. Some experiments might be highly demanding, regarding sensitivity and stability, especially in the field of precision spectroscopy. Depending on the experiment, data extraction can take hours, if not days and its conclusiveness relies on the stability of the probing laser system over the entire acquisition process. If a high-power OFC is used for a spectroscopic experiment, the output

power and especially the frequency comb stabilization must be stable throughout the entire data acquisition process. While high-power OFCs have been demonstrated in several laboratories [36]–[40], a remaining challenge but important demand for highest precision measurements such as ^{229}Th probing is the highly stable and reliable operation of such rather complex laser systems.

This thesis addresses the development of a fully-stabilized high-power femtosecond frequency comb centered at 1 µm wavelength, with a comb line spacing of 65 MHz and more than 70 W average output power. Furthermore, implementation of important features including a new oscillator design, wavelength tuning, adaptation for remote computer control and a technical interlock that ensures fail-safe and stable long-term operation of the system are discussed. The dissertation demonstrates for the first time that a fully-stabilized high-power frequency comb can be operated continuously over several days, paving the way for VUV conversion and ultra-high-resolution spectroscopy in this spectral region.

The following two chapters discuss basic principles of extreme ultraviolet optical frequency comb laser systems and high-power ultrafast lasers. With the foundation laid, chapter 4 and 5 describe the development of the high-power frequency comb laser system and discuss long-term stability and fail-safe operation, as well as remote control. Chapter 6 finally outlines center wavelength tuning capabilities of the laser system, the first steps taken towards intra-cavity high-harmonic generation as well as a complementary experiment targeting laser probing of the ^{229}Th transition inside an ion storage ring.

2 Extreme ultraviolet optical frequency comb laser systems

This chapter introduces important concepts and their theoretical framework. The chapter starts with a very brief introduction to precision spectroscopy, then introduces ultrashort pulses and combs, as well as relevant noise properties.

2.1 Precision spectroscopy

The field of spectroscopy studies the interaction between electromagnetic radiation and matter as a function of the frequency of the radiation. It is a long-established method and provides important information concerning kinetics of chemical reactions, the structure and many other properties of matter. One of the oldest spectroscopy technique is absorption spectroscopy, which is based on studying the wavelength dependence of the absorption by the matter. Nowadays, a large variety of different spectroscopic techniques are developed providing in-depth analysis methods.

Mode-locked lasers (MLLs) generate ultrashort optical pulses relying on a fixed phase relationship across a broad spectrum of frequencies. They can be used for probing and manipulation of the dynamic evolution of a system on ultrashort timescale. Changing the perspective to the frequency domain, energy-level structures of an atomic system may be investigated. Information on optical transitions based on high-precision measurements are particularly important to reveal the composition of matter.

After the groundbreaking invention of optical frequency combs [16], i.e. frequency-stabilized MMLs, the performance of existing spectrometers is dramatically enhanced owing to its ability to provide a precise and direct link between microwave and optical frequencies. They have immediately became a fundamental tool in precision measurements in Rb, Ca, CH_4, H, Sr^+ and Yb^+ [41]. Additionally, ultrashort frequency-comb techniques open new frontiers in ultrafast physics by controlling the phase evolution of few-cycle pulses for exploring highly nonlinear phenomena that depend on the carrier-envelope phase, e.g. above treshhold ionization [42] and high-harmonic generation for attosecond pulse production [43].

2.2 Ultrashort laser pulses

Ultrashort pulses can be defined as laser pulses with pulse duration below a few picoseconds. There has been rapid progress and interest in ultrashort optical pulses in recent years due to their unique properties, which can be listed as follows [44]:

- High time resolution. Owing to their short pulse duration, ultrashort pulses provides very high time resolution enabling access to ultrafast physical processes [45].
- High bandwidth. By the time-bandwidth product, there is an inverse correlation in between the pulse duration and bandwidth. As the pulse duration decreases, bandwidth increases correspondingly. The high bandwidth of ultrashort pulses is important for optical communications [46] and especially for spectroscopy, including frequency comb spectroscopy.
- High intensity. The peak power and peak intensity are inversely proportional to the pulse duration for fixed pulse energy. Combining high-power lasers with ultrashort pulses boosts the peak power enabling petawatt peak power levels [47], which is extremely important for high field science and laser driven nuclear fusion.

2.2.1 Temporal and Spectral Representations

This sections provides a breif introduction into the temporal and spectral representations of ultrashort laser pulses, thereby closely following Ref. [44]. The electric field of an ultrashort pulse can be represented in either temporal or spectral domain. In temporal domain it can be written as

$$E(t) = \mathrm{Re}\{A(t)e^{-i\omega_c t}\} = \frac{1}{2}\left[A(t)e^{-i\omega_c t} + A^*(t)e^{i\omega_c t}\right] \tag{2.1}$$

where $\mathrm{Re}\{\dots\}$ denotes the real part and ω_c is fast varying carrier frequency. $A(t)$ is the slow varying complex pulse envelope and is written as

$$A(t) = |A(t)|e^{-i\phi(t)} \tag{2.2}$$

where $\phi(t)$ is the temporal phase of the complex envelope. In spectral domain, equation 2.1 can be defined via the Fourier transform of $E(t)$

$$\tilde{E}(\omega) = \frac{1}{2}\left[\tilde{A}(\omega-\omega_c) + \tilde{A}^*(-\omega-\omega_c)\right]. \tag{2.3}$$

By definition, $\tilde{E}(\omega)$ is the double-sided spectrum where $\tilde{A}(\omega)$ is the Fourier transform of the complex pulse envelope $A(t)$

$$\tilde{A}(\omega) = \int_{-\infty}^{+\infty} A(t)e^{-i\omega t}\mathrm{d}t \tag{2.4}$$

where complex pulse envelope in the spectral domain $\tilde{A}(\omega)$ is centered at $\omega = 0$ so the term $\tilde{A}(\omega - \omega_0)$ is centered at ω_c thus defining the single-sided spectrum of the pulse. $\tilde{A}(\omega)$ is represented as

$$\tilde{A}(\omega) = |\tilde{A}(\omega)|e^{-i\varphi(\omega)} \tag{2.5}$$

Important parameters can be derived using the equations above. The amplitude of $|A(t)|$ is normalized thus the power averaged over an optical cycle can be written as

$$P(t) = |A(t)|^2. \tag{2.6}$$

The intensity $I(t)$ is the power per unit area and is proportional to $P(t)$.

The most commonly used measure for pulse duration is the intensity full width at half maximum (FWHM), represented as Δt. In the spectral domain $|\tilde{A}(\omega - \omega_c)|^2$ can be attributed a power spectrum $S(\omega)$ and its bandwidth can be measured as FWHM of the positive frequency part of the power spectrum and represented as $\Delta\nu$ where $\Delta\nu = \Delta\omega/2\pi$. Figure 2.1 depicts the temporal and spectral representations of an ultrashort Gaussian

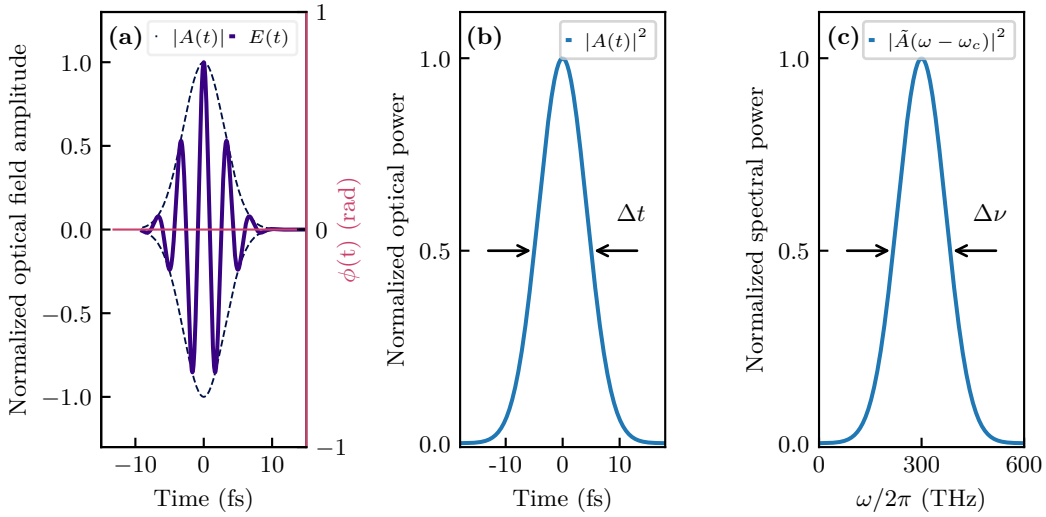

Figure 2.1: The temporal and spectral representations of ultrashort pulses. (a) The optical fields and envelope displayed together with zero temporal phase. (b) The optical power in temporal domain with its FWHM Δt. (c) The spectral intensity of the pulse with its FWHM $\Delta\nu$.

pulse. The carrier frequency (ω_c) is centered around $2\pi 300\,\mathrm{THz}$ which corresponds to a wavelength of $1\,\mu\mathrm{m}$.

Root-mean-square (rms) pulse widths or spectral bandwidths are also commonly used in ultrafast optics which can be defined by

$$\Delta t_{rms} = \sqrt{\langle t^2 \rangle - \langle t \rangle^2} \tag{2.7}$$

$$\Delta\nu_{rms} = \frac{1}{2\pi}\sqrt{\langle\omega^2\rangle - \langle\omega\rangle^2} \tag{2.8}$$

where

$$\langle t^n\rangle = \frac{\int_{-\infty}^{\infty} t^n P(t)\mathrm{d}t}{\int_{-\infty}^{\infty} P(t)\mathrm{d}t} \tag{2.9}$$

and

$$\langle\omega^n\rangle = \frac{\int_{0}^{\infty} \omega^n S(\omega)\mathrm{d}\omega}{\int_{0}^{\infty} S(\omega)\mathrm{d}\omega}. \tag{2.10}$$

2.3 Optical frequency combs

An optical frequency comb (OFC) is an optical source whose spectrum consists of equally spaced narrow lines in the frequency domain. They were initially invented for time and frequency metrology, used as an optical synthesizer to support the world's most precise clocks [48], [49]. After its invention, OFCs quickly found applications beyond their original purpose. They are used for trace gas sensing [50], calibration of atomic spectrographs [51], ranging [52], optical communication [53] and molecular fingerprinting [54].

Although there are several ways to build an OFC, MLLs were the original source for OFCs. MLLs generate short optical pulses by utilizing a fixed phase relationship between all the lasing longitudinal modes [55], which appear as individual well-separated modes in the optical spectrum if the MLL exhibits sufficiently low noise. As a consequence, phase and frequency dynamics of every optical mode in the laser OFC spectrum is are intertwined and deterministic. This leads to determining the absolute frequency of any mode from knowledge of absolute frequency of one mode.

MLLs delivers short optical pulses by utilizing a fixed phase relationship between all the lasing longitudinal modes, which form the comb structure. A train of ultrashort pulses is emitted in the time domain at the output of the MLL's cavity as shown in Fig. 2.2 (a). The period of the envelope of the pulses for cavity round-trip length L and group velocity of the light υ_g is $1/f_{rep} = L/\upsilon_g$. The dispersion in the MLL cavity introduces a pulse-to-pulse phase-shift $\Delta\Phi$ between the envelope and carrier of the electric field of the pulses due to the different group (υ_g) and phase (υ_p) velocities of the pulse. This phase-shift results in a shift of the optical frequencies which is arisen from the pulses which add-up constructively which eventually shifts the entire frequency comb. This phase is called carrier-envelope offset (CEO) phase and it can be written as

$$\Delta\Phi_{\mathrm{CEO}} = L\omega_c(\upsilon_g^{-1} - \upsilon_p^{-1})\mathrm{mod}2(\pi), \tag{2.11}$$

where ω_c is the center frequency of the optical pulse. The carrier-envelope offset phase can be related to a corresponding frequency, describing an offset of the comb from zero frequency:

$$f_0 = \frac{\Delta\Phi_{CEO}}{2\pi T}. \tag{2.12}$$

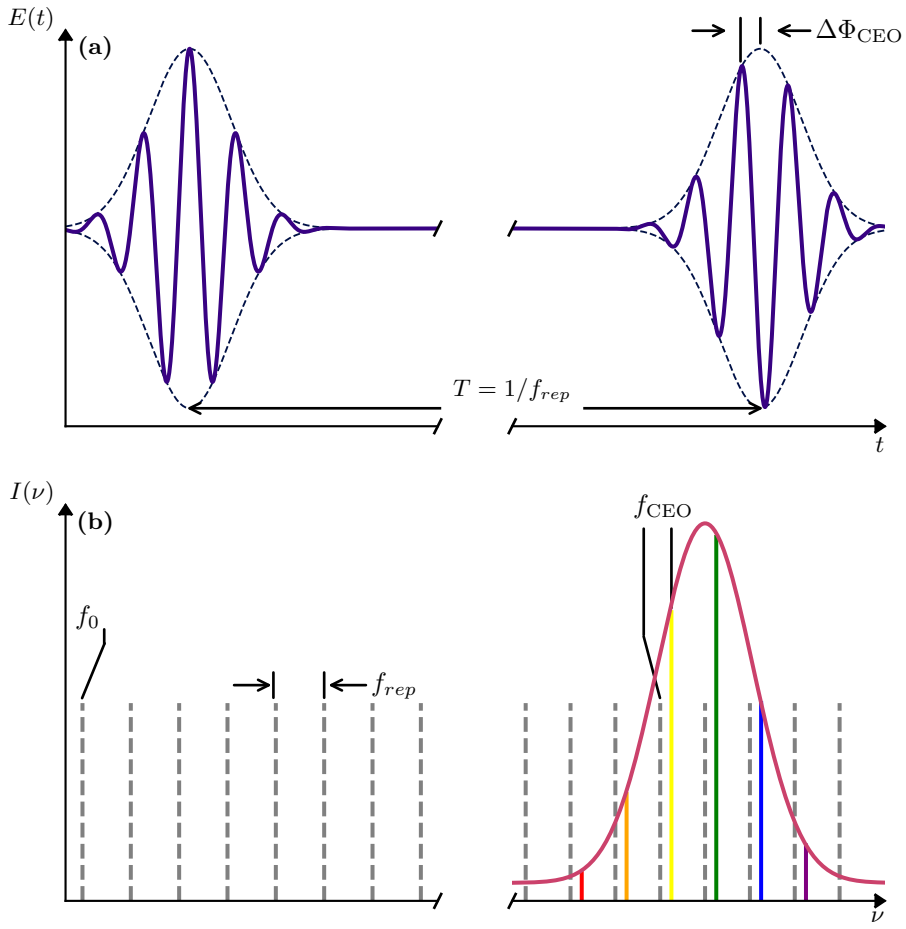

Figure 2.2: Time and frequency domain depiction of the comb structure from mode-locked lasers.

Therefore, in the frequency domain, the optical frequencies of the discrete set of evenly spaced narrow lines ν_n can be written in a comb equation as

$$\nu_n = n f_{rep} + f_0, \tag{2.13}$$

where n is an integer and has typical values in the order of 10^6. From the equation 2.13 it can be seen that if the f_{rep} and f_0 are sufficiently stable (via passive low noise operation of the MML or via active stabilization), a comb structure is formed in the optical domain.

2.3.1 Carrier-envelope offset frequency detection

In order to convert MLLs into OFCs, the pulse repetition frequency and the CEO frequency are typically actively stabilized. However, for stabilization, the frequencies need to be detected first. The pulse repetition frequency is easily detectable by a fast photodiode

since the pulse repetition frequencies are usually in the range of tens or hundreds of MHz. Detection gets more challenging for the CEO frequency. Optical frequencies cannot be directly measured simply due to the lack of fast electronics since they are typically in the range of few hundred terahertz. On the other hand, frequency combs creates a link between optical frequencies and radio frequencies. The distinct frequency of any comb line in the comb spectrum via 2.13 as soon as the CEO frequency is known. CEO frequency detection initially was done in time domain via an interferometric method [56] however, the method was not phase-coherent which brought a large error to the measurement. Later, the heterodyne beating scheme in the frequency domain [57] has proven to be a successful measure for CEO frequency detection.

The general idea of the introduced scheme relies on generating a heterodyne beate note via nonlinear processes from different parts of the comb spectrum. The simplest method uses the second harmonic of the mth mode from the low-frequency side of the comb and the $2m$th mode from the high-frequency side. This can be formulated as

$$\begin{aligned} 2\nu(m) - \nu(2m) &= (2mf_{rep} + 2f_0) - (2mf_{rep} + f_0) \\ &= f_0. \end{aligned} \tag{2.14}$$

The so-called self referenced f_0 detection method which follows Eq. 2.14 is depicted in figure 2.3.

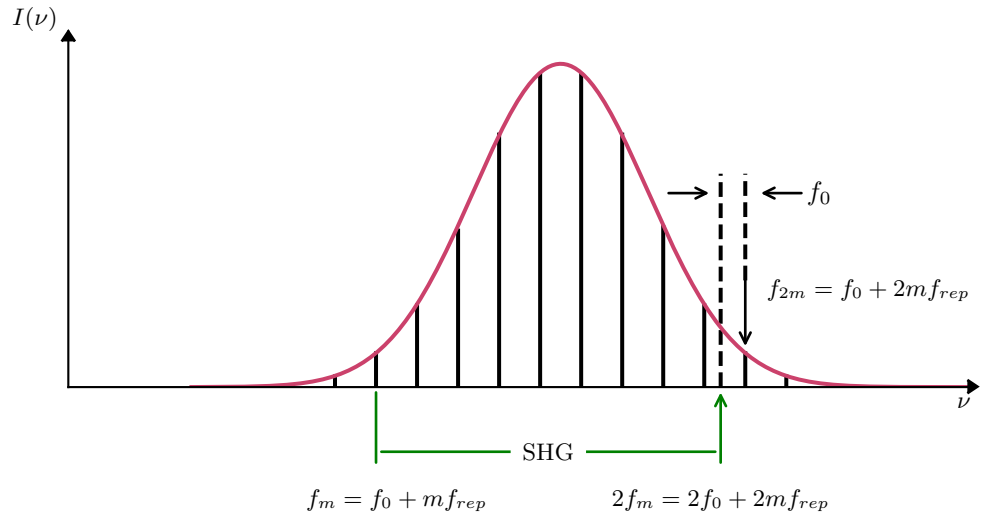

Figure 2.3: Illustration of self referenced CEO frequency (f_0) detection by beat note generation between the second harmonic of m^{th} comb line with the $2m^{\text{th}}$ comb line.

In this method, the spectral coverage of the frequency comb requires to be at least one octave since the frequency ratio between the high and low frequencies needs to be 2:1.

However, MLLs do not necessarily provide an octave-spanning spectrum at the output directly. Supercontinuum generation in optical fibers provides an elegant solution to this issue while maintaining the coherence properties [58]. The method can be realized using an f-$2f$ interferometer which is depicted in Fig. 2.4. In the interferometer, the amplified light from the MLL is coupled into a highly nonlinear fiber (HNLF) in which an at least octave-spanning supercontinuum is generated. The supercontinuum is then split into two parts via dichroic mirror (DM) separating long (red) and short (blue) wavelengths. The short wavelength portion of the supercontinuum passes through wedges used for temporal delay tuning while the long wavelength portion is focused into a nonlinear crystal for SHG. Then both the short wavelength portion and the second harmonic of the long wavelength portion are re-combined in a beam splitter (BS) and then sent on the photo diode (PD) for beat note generation. Before the PD, a bandpass filter (BPS) is used to select the correct wavelength. Filtering out light that does not contribute to beat note generation reduces the background signal on the PD, increasing the signal-to-noise ratio. A radio frequency (RF) analyzer can be used to measure the signal from the PD where f_0, f_{rep} and $f_{\mathrm{rep}} - f_0$ can be detected.

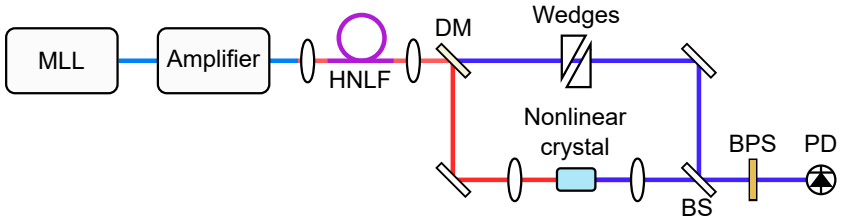

Figure 2.4: Standard f-$2f$ interferometer. HNLF: highly nonlinear fiber, DM: dichroic mirror, BS: beam splitter, BPS: band pass filter, PD: photodiode.

2.3.2 Comb stabilization

As discussed before in the previous section, an optical frequency comb of a modelocked laser has two degrees of freedom: the "comb breathing" which can be described with f_{rep} and the "comb translation" described with f_0 [59]. In order to convert modelocked lasers into optical frequency combs, the mentioned degrees of freedom typically need to be stabilized. Detection and stabilization of f_{rep} is rather straightforward since it is directly related to the cavity length $f_{\mathrm{rep}} = c/\mathrm{L}$ where L is the cavity length. Cavity length stabilization can be realized via piezoelectric actuators made out of lead-zirconium-titanate (PZT). Meanwhile, f_0 is directly related to the difference in group and phase velocities in the MLL cavity and can be controlled for example via feedback to the pump power of the MLL [60]. A phase locked loop (PLL) can be used for feedback. A PLL includes a phase detector and a voltage-controlled oscillator (VCO) as a feedback mechanism to track the frequency or phase of an input (local oscillator or reference) by adjusting the frequency or

phase of the VCO. In the synchronized state, the phase error in-between the input and a reference is either zero or constant. In case the phase error builds up, the control system (loop filter) acts on the input in a way that the phase error in between the input and the reference pulls back to zero or its defined constant value. The circuit consists of a phase detector, which produces a voltage proportional to the relative phase between two RF signals. In the RF domain, the phase detector can be a frequency mixer or in optics it is called an interferometer. A loop filter is used as a controller that generates the control signal for synchronization. A general scheme for a PLL is depicted in Fig. 2.5

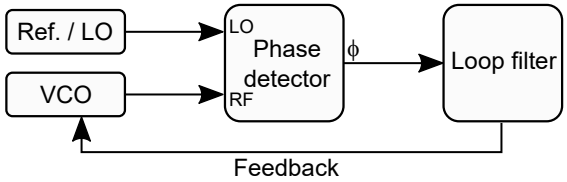

Figure 2.5: Block diagram of a PLL. VCO: voltage-controlled oscillator, Ref.: Reference signal, LO: local oscillator.

As a loop filter, proportional-integral-derivative (PID) controllers are commonly used. A PID controller calculates the error value $e(t)$ in-between the set point and the monitored signal and acts on the signal using proportional, integral and the derivative terms. The overall control signal $u(t)$ can be written as

$$u(t) = K_p e(t) + K_i \int_0^t e(T)dT + K_d \frac{\mathrm{d}e(t)}{\mathrm{d}t}, \tag{2.15}$$

where K_p, K_i and K_d are non-negative coefficients for the proportional, integral and derivative terms, respectively.

For frequency comb stabilization, the simplest method is to feed the measured f_0 or f_{rep} RF signals to a PLL, and phase lock it to an external RF reference. The output of the PID controller is then fed to the respective actuators for stabilization. In order to achieve a stable lock with low-phase noise, the locking bandwidth of the actuators needs to be high in order to compensate for high-frequency errors. High-bandwidth locks, however, suffer from a limited tuning range. In order to achieve both low-noise and long-term frequency comb stabilization, a second low-bandwidth loop is typically introduced to the locking scheme which accommodates low-bandwidth response but a much larger tuning range.

To achieve more robust lock, it makes sense to lock the signal not to the measured fundamental but to its higher harmonics since the error in-between the reference and the input signal is enhanced.

As alternative solution for, f_{rep} stabilization, it is possible to use a CW optical signal as an external reference (local oscillator). Since the lock performance is directly related to the reference signal used in the PLL, it is possible to achieve a tight lock by heterodyne

beating the low-noise single frequency CW laser (ν_{CW}) with a comb line signal. The difference frequency in between the nth comb line and the CW laser and can be expressed as:

$$f_{\mathrm{CW}} = \nu_{\mathrm{CW}} - \nu_n = \nu_{\mathrm{CW}} - f_0 - n f_{\mathrm{rep}}. \tag{2.16}$$

The Eq. 2.16 shows that the f_{rep} can be stabilized by stabilizing the f_{CW}. In addition, a stable CW laser optionally synchronized to an absolute frequency reference that can be used to enable frequency determination with high accuracy using the comb.

2.4 Noise properties

The noise of lasers can be explained in the simplest term as fluctuations of various output parameters. Especially for mode-locked lasers, timing jitter, optical phase noise and CEO noise are particularly important for many applications such as frequency metrology and fast data transmission [61]. The origin of laser noise can be divided into two categories: quantum noise and technical noise. Quantum noise is caused by measurement uncertainties inherent to the theory of quantum mechanics and it can lead to intensity and phase noise [62]. On the other hand, technical noise arises from effects such as temperature fluctuations or vibrations, as well as noise of the pump diode in the laser cavity or gain medium. The fluctuations in the output power of the pump diode leads to intensity noise due to the gain response and saturation dynamics. Also, Kramers-Kroning-related phase changes, which explain the phase changes in the gain medium, can also lead to intensity noise when combined with spectrally limited optical gain [63]. Meanwhile, vibrations of the intracavity mirrors as well as refractive index fluctuations caused by thermal effects can lead to timing jitter as a result of optical cavity length fluctuations.

Finally, for mode-locked lasers, there is a variety of different physical mechanisms, which can couple to different kinds of noise. Intensity noise can couple to optical phase noise via Kerr nonlinearity and to timing jitter via self-steepening, as well as to gain fluctuations and therefore to optical phase noise and pulse timing via refractive-index changes [64]. Accordingly, different noise behavior is expected for different mode-locked laser types and different laser parameters.

In the following subsections, relevant types of noise are discussed within the scope of this thesis. For the mathematical notation, the following sections closely follow Ref. [65].

2.4.1 Power spectral density

For a spectral quantity that exists in finite span of time a frequency-dependent power density $S(f)$ can be defined via the square modulus of the Fourier-transformed data as [65]:

$$S_P(f) \equiv \lim_{T\to\infty} \frac{1}{T} \left| \int_{-T/2}^{+T/2} P(t) \exp\{-i2\pi f t\}\, \mathrm{d}t \right|^2 . \tag{2.17}$$

Based on the Wiener-Khinchin theorem which offers a connection to the autocorrelation function of laser power P, equation 2.17 changes into

$$S_P(f) = \int_{-\infty}^{+\infty} R_P(\tau) \exp\{-i2\pi f \tau\}\, \mathrm{d}\tau \tag{2.18}$$

where $R_P(\tau) = \langle P(t)P(t+\tau)\rangle$. The autocorrelation function can be retrieved with an inverse Fourier transform

$$R_P(\tau) = \int S_P(f) \exp\{-i2\pi f \tau\}\, \mathrm{d}f. \tag{2.19}$$

Finally, the variance can be calculated as

$$\sigma_P^2 \equiv \left\langle P^2 \right\rangle = R_P(0) = \int S_P(f)\, \mathrm{d}f \tag{2.20}$$

which can be integrated for the frequency range of interest.

2.4.2 Intensity noise

The term intensity noise describes the output power variation of a laser. The time varying output power can be written as

$$P(t) = \overline{P} + \delta P(t), \tag{2.21}$$

where $\overline{P}$ is the average power and the δP is the power variation. It is usually statistically quantified as power spectral density of relative intensity ($\delta P/\overline{P}$) and usually referred to as relative intensity noise (RIN). The single-sided power spectral density (PSD), which is dependent on the noise frequency f, can be written as [65]

$$S_I(f) = \frac{2}{\overline{P}^2} \int_{-\infty}^{+\infty} \langle \delta P(t) \delta P(t+\tau)\rangle \exp(i2\pi f\tau) \mathrm{d}\tau. \tag{2.22}$$

The factor 2 in the formula is coming from the fact that the spectrum is single-sided and its unit commonly is dBc/Hz. It can also be integrated over a frequency interval (f_1, f_2) of noise frequencies to obtain an rms value of relative intensity noise

$$\left.\frac{\delta P}{\overline{P}}\right|_{rms} = \sqrt{\int_{f1}^{f2} S_I(f) \mathrm{d}f}. \tag{2.23}$$

2.5 Extreme ultraviolet frequency combs

Amplified ultrafast laser systems driving the HHG process are wide-spread sources for XUV generation [66]. These short-wavelength sources are useful for many interesting applications such as time-resolved attosecond dynamics studies or high-resolution lensless imaging [67]–[70]. However, these sources are typically used in extra-cavity HHG experiments, where the IR pulse with typically less than 100 kHz pulse repetition rate leads to bursts of attosecond XUV emission. The produced XUV pulses are broadband and do not possess defined and stable frequency lines. Using a high pulse repetition rate frequency comb laser to drive the HHG process enables high-precision spectroscopy since the spectral resolution will be limited by a single comb tooth [66]. However, the HHG is very inefficient causing severe power limitations for XUV combs.

From the vacuum ultraviolet (VUV) wavelenghts perspective, the most straightforward approach to generate VUV wavelengths is to use ytterbium (Yb)-based OFCs and convert these sources via harmonic generation into the VUV. Commonly used techniques for ultraviolet and VUV generation employ nonlinear crystals [71], hollow-core fibers [72] and gas jets [73]. Although, VUV generation in hollow-core fibers seems to be the most efficient technique, it is yet to be shown that the coherence properties of the fundamental frequency comb are transferred to the generated VUV. On the other hand, it is shown that, using VUV generation in gas jets the coherence properties of the input light can be transferred to the VUV [74]. However, this technique suffers from low conversion efficiencies and typically reaches 10^{-5}, shown via Krypton gas jet VUV generation [31].

In order to overcome this efficiency limitation and to reach sufficient high laser pulse energies for VUV conversion even at high repetition rate, while keeping the frequency comb structure, an fsEC was proposed [32], [33]. Inside the fsECs the ultrashort pulses from an optical frequency comb add up coherently when the cavity length is matched to the pulse repetition rate of the comb. The enhanced intracavity field is able to provide the necessary peak intensity for harmonic generation. The demonstrated spectral resolution and capability to enhance the peak intensities, extends direct frequency comb spectroscopy into extreme ultraviolet wavelengths [35] as well as improves the performance of high resolution spectroscopy [36] and precision measurements [75] in this spectral region.

3 High-power CPA ultrafast laser systems

In this chapter, an introduction for high-power CPA based ultrafast lasers is provided. First, mode-locking techniques for ultrashort pulse generation are presented. Next, fiber lasers and mode-locked fiber lasers are introduced. Then the nonlinear pulse propagation in optical fibers is discussed. Finally, dispersion and its compensation as well as ultrashort pulse amplification are explained.

3.1 Mode-locking

Mode-locked lasers are the primary sources for ultrashort pulse generation [8], [76] and optical frequency combs. The ultimate goal of mode-locking is to suppress unwanted operation modes of the cavity (e.g. continous-wave), while achieving stable pulsed operation. In order to achieve mode-locking, a scheme supporting decreased cavity losses for pulsed operation is required. It can either be realized by an externally driven intracavity loss modulator (active) or by a nonlinearity-induced (passive) phase or amplitude modulation.

The following derivations closely follow the reference [77]. For a simplified explanation of mode locking, a few assumptions can be made. First, the laser is assumed to operate only in the fundamental transverse mode, the longitudinal modes can be treated similar to the modes of a Fabry-Perot resonator with a constant cavity round-trip length L. Secondly, all the longitudinal modes can be assumed to be lasing in phase, such that superposition of all modes represents a pulse with a spatial extent much shorter than the cavity without the presence of a dispersive element. Finally, it can be assumed that the laser consists of a series of spectral components (frequency lines) of constant amplitude spaced by the cavity free spectral range, ν_c. If the center frequency is ω_0, the total electric field (E_{total}) can be written as

$$E_{\text{total}}(t) = E_0 \sum_{-(N-1)/2}^{+(N-1)/2} \exp\left[i(\omega_0 + n\omega_c)t + i\phi_n(t)\right] \tag{3.1}$$

where $\phi_n(t)$ is a random function of time uniformly distributed between 0 and 2π. The time-averaged intensity can be given as $\langle I \rangle = NI_0$ (where I_0 is the intensity of each line) since for square modulus of the field, cross-terms average to zero. Mode-locking then

refers to the phase-relation between all spectral lines being fixed. Thus, the $\phi_n(t)$ term can be taken out of the sum and total field can be written as

$$E_{\text{total}}(t) = E_0 e^{i\omega_0 t + i\phi(t)} \sum_{-(N-1)/2}^{+(N-1)/2} e^{in\omega_c t} = E_0 e^{i\omega_0 t + i\phi(t)} \frac{\sin\left(N\omega_c t/2\right)}{\sin\left(\omega_c t/2\right)}. \tag{3.2}$$

From this, we can derive a few key relations, such as the intensity

$$I(t) = I_0 \left[\frac{\sin\left(N\omega_c t/2\right)}{\sin\left(\omega_c t/2\right)}\right]^2 \tag{3.3}$$

the peak intensity of this function is then

$$I_{peak} = N^2 I_0 \tag{3.4}$$

and the temporal width of each pulse is can be approximated as:

$$\Delta t_p \approx \frac{1}{N\nu_c} \qquad \nu_c = \omega_c/2\pi. \tag{3.5}$$

More realistically, if the envelope of the spectral modes is Gaussian, the amplitude of the electric field at the n^{th} mode is

$$E_n = E_0 \exp\left[-2\ln 2\left(\frac{n\omega_c}{\Delta\omega}\right)^2\right] \tag{3.6}$$

where E_0 is the field at the peak of the Gaussian envelope and $\Delta\omega$ is the width in angular frequency units. In time domain, the field is

$$E(t) = E_0 e^{i\omega_0 t} \sum_{-(N-1)/2}^{+(N-1)/2} \left\{\exp\left[-2\ln 2\left(\frac{n\omega_c}{\Delta\omega}\right)\right]\right\} e^{in\omega_c t}. \tag{3.7}$$

Since N is very large, this series can be converted into an integral using $x = n\omega_c$ and $dx = \omega_c$, the field is then

$$E(t) = \frac{E_0 e^{i\omega_0 t}}{\omega_c} \int_{-\infty}^{+\infty} \left\{\exp\left[-\frac{2\ln 2 x^2}{\Delta\omega^2}\right]\right\} e^{in\omega_c t} \mathrm{d}x\,, \tag{3.8}$$

which can be solved analytically resulting in:

$$E(t) = E_o E^{i\omega_0 t} \left(\frac{\pi}{2\ln 2}\right)^{1/2} \left(\frac{\Delta\omega}{\omega_c}\right) \exp\left[-\left(\frac{\Delta\omega t}{2\sqrt{\ln 2}}\right)^2\right]. \tag{3.9}$$

The intensity is

$$I(t) = I_0 \exp\left[-2\left(\frac{\Delta\omega t}{2\sqrt{\ln 2}}\right)^2\right], \tag{3.10}$$

which forms a Gaussian-shaped pulse of width

$$\Delta t_p = \frac{2\ln 2}{\pi}\frac{1}{\Delta\nu} \approx \frac{0.44}{\Delta\nu} \qquad \Delta\nu = \Delta\omega/2\pi. \tag{3.11}$$

3.1.1 Active mode-locking

Active mode-locking uses an externally driven amplitude or phase modulator placed inside the laser oscillator. For amplitude-modulated mode-locking, the modulator ensures that the only internal field distribution supported by the laser is a series of short pulses, i.e. the modulator only allows transmission for a short pulse and hence for a high peak power. Acousto-optical modulators (AOMs) are commonly used for active mode-locking. AOMs rely on the acousto-optic effect to generate diffraction via a pressure and/or strain-induced periodic refractive index modulation [78]. For active mode-locking, employment of an AOM generating a standing acoustic wave is common. Here, the standing wave generates an inherent modulation at twice the acoustic frequency at constant driving power. In order to then modulate the losses and therefore amplitude at the roundtrip frequency, the acoustic frequency is $^1/_2 f_{\mathrm{roundtrip}} = {}^c/_{4L}$. Fig. 3.1 (a) depicts an AOM mode-locked cavity, where the modulator is driven at one half of the mode separation frequency, $c/4L$.

For frequency-modulation mode-locking a phase modulator, usually an electro-optical modulator (EOM) or Pockels cell, is inserted into the cavity. Phase modulation simply corresponds to a modulation of the optical path length in the cavity.

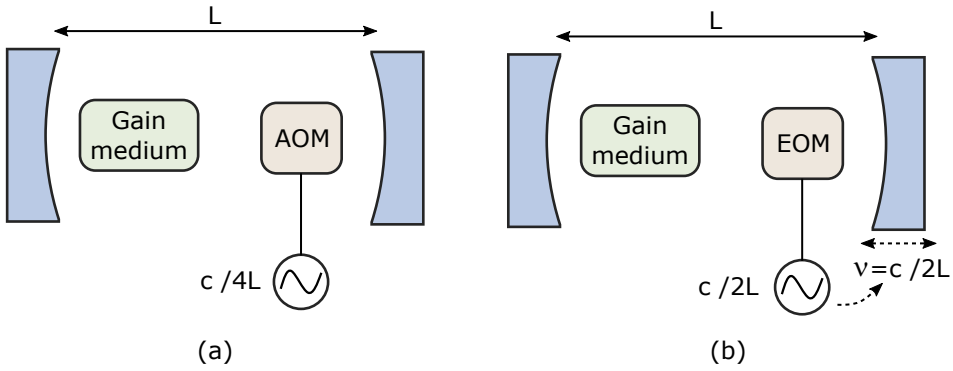

Figure 3.1: Active mode-locking using an AOM (a) and an EOM (b) placed inside the cavity.

A wave packet incident on the moving mirror will be Doppler shifted after the reflection. Depending on the speed of the modulation on the mirror, laser oscillation can be prevented. However, if the wave packet arrives at the mirror when it is reversing direction, there will be no Doppler shift, so the laser oscillation can occur. As shown in Fig. 3.1 (b), the phenomenon can be visualized as a moving mirror oscillating at a frequency of $c/2L$.

3.1.2 Passive mode-locking

Active mode-locking has drawbacks in terms of achievable pulse duration and stability, as it depends on an external control signal, which has to be generated. Contrary to

that, passive mode-locking techniques exploit physical effects which naturally occur in optical cavities. The most common mode-locking technique is passive mode-locking, it needs no external optical device, but uses nonlinear behavior of the intracavity medium. More specifically, this approach uses a saturable absorber (SA). The absorption or cavity loss introduced by a SA decreases with increasing intensity. Consequently, the loss the SAs favors short pulses rather than CW operation and therefore the scheme is viable for ultrafast pulse generation. SAs are often combined with one of the cavity mirrors to form a semiconductor saturable absorber mirror (SESAM) [59], [79].

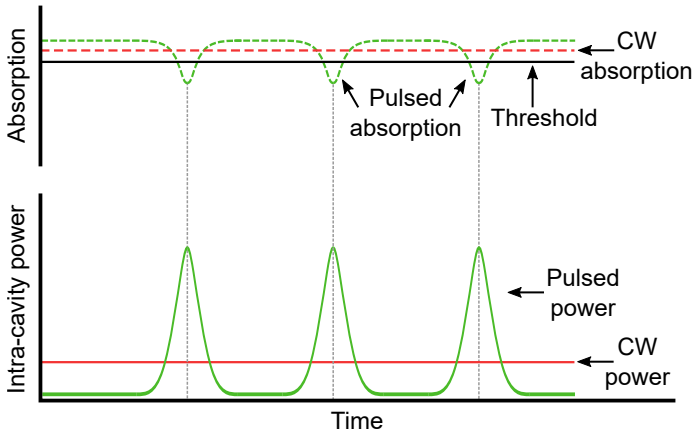

Figure 3.2: Illustration of saturable absorber in a laser cavity. The solid red and green lines depicts the CW and pulsed operation with identical average power, respectively. The dashed lines are the corresponding absorption of the saturating medium.

Figure 3.2 shows the absorption of the laser cavity as a function of time, where CW operation results in a peak power which is below the lasing threshold and therefore suppressed. However, the pulsed wave around its peak of the pulses is above threshold and thus, the laser will lase at those times. The time behavior of the SESAM shows a rapid saturation below 1 ps followed by a longer recovery time as long as hundreds of picoseconds. The disadvantage of SESAMs is their bandwidth, usually they don't support sufficient bandwidths for very short pulses and also the degradation of the material during long-time of operation poses a problem.

To achieve an even faster response Kerr-lens mode-locking (KLM) can be used. KLM exploits the optical Kerr effect, where the refractive index (n_0) is modulated by the nonlinear refractive index (n_2) as

$$n = n_0 + n_2 I. \tag{3.12}$$

The radial intensity distribution of the Gaussian beam is

$$I = I_0 e^{-2r^2/{\omega_0}^2} \tag{3.13}$$

and for a medium length L, the overall phase shift, ϕ, is

$$\phi = \frac{2\pi nL}{\lambda}. \tag{3.14}$$

Thus, the change in $\mathrm{d}\phi$ in the phase shift due to the intensity distribution is

$$\mathrm{d}\phi = \frac{2\pi L}{\lambda}\mathrm{d}n = \frac{2\pi Ln_2 I_0}{\lambda}e^{-2r^2/{\omega_0}^2} \approx \frac{2\pi Ln_2 I_0}{\lambda}(1 - 2r^2/{\omega_0}^2) \tag{3.15}$$

near the center of beam. This quadratic dependence of the phase shift with radial distance, describes a positive lens. Since the strength of the lens is proportional to the intensity, by placing a slit downstream from a Kerr medium, one can cause the loss for weak beams (non-focused) to be much greater than that for intense beams (focused). This effect is similar to the behavior of a saturable absorber: the oscillator favors pulses instead over CW operation.

3.2 Fiber lasers

An optical fiber is a cylindrical dielectric waveguide usually fabricated from a low-loss material such as silica glass. From a simple perspective and considering the most basic fiber type, the light is guided in its core, which is surrounded by a cladding of slightly less refractive index, n_1 and n_2, respectively, depicted in Fig. 3.3. Only light, whose

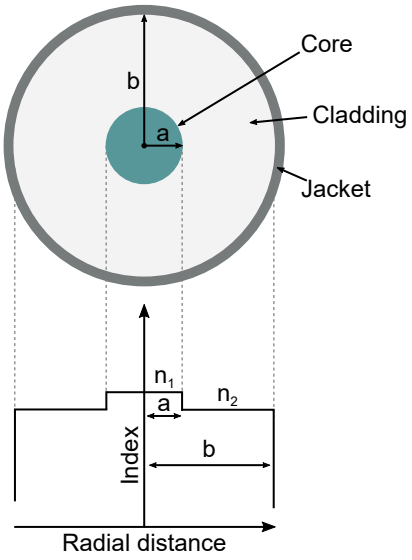

Figure 3.3: Cross-section and refractive index profile of a step-index fiber.

propagation vectors with an angle less than $\sqrt{n_1^2 - n_2^2}$ with the fiber axis will be accepted by it and propagate in it. Numerical aperture (NA) is a dimensionless number, which

identifies the range of angles on an optical system, that accepts or emits light. NA of this so-called step-index fiber is given by

$$\mathrm{NA} = \sqrt{n_1^2 - n_2^2}. \tag{3.16}$$

The modal capacity of the fiber is defined by the V parameter, which can be calculated as:

$$V = \frac{2\pi}{\lambda} a\mathrm{NA} = \frac{2\pi}{\lambda} a\sqrt{n_1^2 - n_2^2} \tag{3.17}$$

where λ is the vacuum wavelength and a is the radius of the fiber core. Fibers with $V \leqq 2.405$ are called single-mode fibers (SMF). SMFs only support one mode per polarization direction. V-number for multi-mode fibers (MMF) is much higher and the number of supported modes (M) is given by $M \approx V^2/2$. The light in the core at the core-cladding interface undergoes total internal reflection at angles smaller than the so-called critical angle defined by

$$\alpha_{\mathrm{crit}} = \arcsin\frac{n_2}{n_1} \tag{3.18}$$

and is thereby guided thorough the core without refraction into the cladding and thus, without loss.

A fiber laser is created when a fiber amplifier is placed in an optical resonator. Fibers can be doped. In order to modify the refractive index, most commonly, germanium, phosphorus and fluorine are used. Germanium and phosphorus both increase and fluorine decreases the index. Additionally, to create a gain medium (amplifying fiber), fibers can be doped with rare-earth ions for different wavelength ranges, such as ytterbium (Yb^{3+}), erbium (Er^{3+}), thulium (Tm^{3+}) and holmium (Ho^{3+}). The gain bandwidth of rare-earth-doped-fibers is fairly large, which enables the generation of ultrashort pulses.

Fiber lasers have many advantages. Because of their geometry, fibers are able to guide the light over large distances in a stable manner. Additionally, they provide a very high single-pass gain as a result of a long interaction path of the light with the active (gain) medium. Nowadays, combined with advanced fiber-optic components, very simple but compact, robust, all-fiber and thus, alignment-free fiber oscillators can be built [80]. Employing polarization-maintaining (PM) fibers, minimizes the disturbance on the system from environmental effects such as temperature and vibrations. Furthermore, owing to its very large surface-to-active-volume ratio and consequently easier heat dissipation, fiber lasers can be operated at very high average power levels.

3.2.1 Mode-locked fiber lasers

Mode-locking methods discussed in section 3.1 can also be applied to mode-locked fiber lasers. The most commonly used mode-locked fiber lasers are based on passive mode-locking [81]. In order to utilize the advantages of the fibers, there is a strong motivation to build all-fiber lasers. Nonlinear polarization rotation (or evolution) [82] and nonlinear

amplifying loop mirrors (NALMs) [83] are two commonly used fiber-based passive mode-locking methods based on Kerr nonlinearity. It is also worth mentioning mode-locked fiber lasers based on linear cavity terminated by a SESAM [84]. However, within the scope of this dissertation, we are going to focus on NALM since it is used in our system.

Initially, nonlinear optical loop mirrors (NOLMs) were first presented as an optical switch [85]. Later, by inserting an amplifying gain section into the NOLM, NALM mode-locked fiber lasers are realized [83], [86]–[89]. The main idea of NALM mode-locking is to

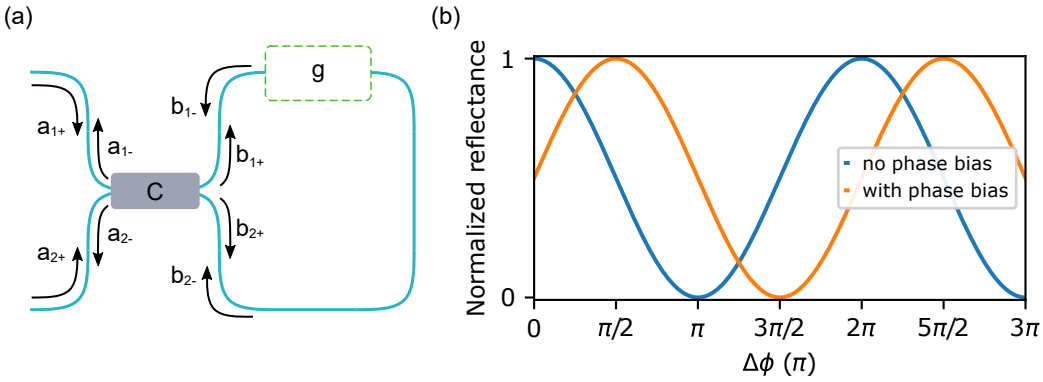

Figure 3.4: (a)Illustration of the NALM principle. (b) Normalized reflectance of a NALM as a function of nonlinear phase difference between two counter-propagating pulses for the cases of no phase bias and with phase bias in blue and orange, respectively. C: coupler and g: gain.

utilize the Kerr effect to realize intensity-dependent cavity losses. To understand this, it is worth considering how the field components evolve and interact within a NALM loop. As shown in Fig. 3.4 (a) the fields injected into the loop b_{1+} and b_{2+} for input fields a_{1+} and a_{2+} via a fiber-based coupler can be written as [44]

$$\begin{pmatrix} b_{1+} \\ b_{2+} \end{pmatrix} = \begin{pmatrix} \sqrt{\alpha} & \sqrt{1-\alpha} \\ \sqrt{1-\alpha} & -\sqrt{\alpha} \end{pmatrix} \begin{pmatrix} a_{1+} \\ a_{2+} \end{pmatrix} \tag{3.19}$$

where α is the splitting ratio of the fiber coupler. After entering the loop, the fields b_{1+} and b_{2+} are amplified. However, as the gain medium is inserted asymmetrically, the accumulated nonlinear phase for clockwise (cw) and counter-clockwise (ccw) directions differs. The fields within the loop after propagation can be given by

$$\begin{pmatrix} b_{1-} \\ b_{2-} \end{pmatrix} = \begin{pmatrix} 0 & E^g E^{-i\phi_1} \\ E^g E^{-i\phi_2} & 0 \end{pmatrix} \begin{pmatrix} b_{1+} \\ b_{2+} \end{pmatrix} \tag{3.20}$$

where g is the gain coefficient and ϕ_1 and ϕ_2 are the accumulated nonlinear phase for cw and ccw directions, respectively. Finally, the output fields (a_{1-} and a_{2-}) can be written as

$$\begin{pmatrix} a_{1-} \\ a_{2-} \end{pmatrix} = \begin{pmatrix} \sqrt{\alpha} & \sqrt{1-\alpha} \\ \sqrt{1-\alpha} & -\sqrt{\alpha} \end{pmatrix} \begin{pmatrix} b_{1-} \\ b_{2-} \end{pmatrix}. \tag{3.21}$$

If we make the assumption that there is only one input for the loop, $a_{2+} = 0$, the output power normalized to the input power and the gain is given by

$$\begin{aligned} \left|\frac{a_{1-}}{a_{1+}}\right|^2 E^{-2g} &= 4\alpha(1-\alpha)\cos^2\left(\frac{\Delta\phi}{2}\right) \\ \left|\frac{a_{2-}}{a_{1+}}\right|^2 E^{-2g} &= 1 - 4\alpha(1-\alpha)\cos^2\left(\frac{\Delta\phi}{2}\right). \end{aligned} \tag{3.22}$$

Assuming that the coupling ratio of the coupler is 50:50 hence $\alpha = 0.5$, Eq. 3.22 is reduced to

$$\begin{aligned} \left|\frac{a_{1-}}{a_{1+}}\right|^2 E^{-2g} &= \cos^2\left(\frac{\Delta\phi}{2}\right) \\ \left|\frac{a_{2-}}{a_{1+}}\right|^2 E^{-2g} &= 1 - \cos^2\left(\frac{\Delta\phi}{2}\right). \end{aligned} \tag{3.23}$$

As described by Eq. 3.22 the output of the NALM depends on the nonlinear phase difference $\Delta\phi$ in between cw and ccw pulses. For the special case where the coupling ratio of the coupler is 50:50 in Eq. 3.23, when $\Delta\phi = 0$, all the power is reflected back to the input port. Fig. 3.5 illustrates a special configuration of a NALM laser called figure-

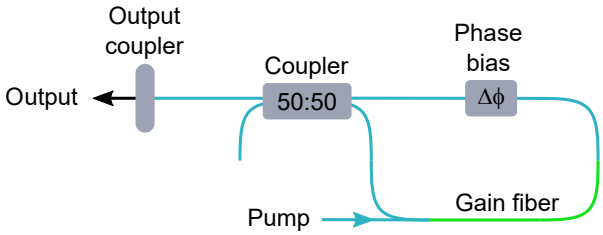

Figure 3.5: Schematic of the figure-of-9 NALM oscillator. Blue and green lines depicts passive and active fiber, respectively.

of-9 laser [90]. They are the successor of the figure-of-8 lasers [85], [91]. Figure-of-8 lasers require longer fiber length in order to fulfill the nonlinear phase requirement in between cw and ccw propagating pulses. Additionally, figure-of-8 lasers have problems with the self-starting mode-locking due to the higher mode-locking thresholds. In the figure-of-9 configuration, the long fiber is replaced with a nonreciprocal phase shifter [87], which supplies the required linear phase difference in between cw and ccw directions. Also, the phase shifter changes the operational aspect of the configuration, shown in Fig. 3.4 (b), which decreases the mode-locking threshold and helps with the self-starting feature of the laser. Furthermore, it is shown that this type of NALM oscillators [86], [92] has very low noise concerning timing jitter and f_0 supporting a narrow linewidth. These features of the NALM laser is figure-of-9 configuration, makes it an excellent candidate to be used in a frequency comb for precision spectroscopy.

3.3 Nonlinear pulse propagation in optical fibers

The nonlinear Schrödinger equation (NSE) in general, is derived from the Maxwell equations and describes the propagation of a pulse through a nonlinear medium. As such it can be applied to an optical fiber, taking into account certain boundary conditions. Due to the symmetry of fibers, using cylindrical coordinates is convenient and a possible representation is given by: [93]–[95]

$$i\frac{\partial A}{\partial z} - \frac{\beta_2}{2}\frac{\partial^2 A}{\partial t^2} - i\frac{\beta_3}{6}\frac{\partial^3 A}{\partial t^3} + \gamma(\omega_c)|A|^2 A + i\frac{\alpha A}{2} = 0. \tag{3.24}$$

Here, t is the time coordinate of a frame of reference which moves with the group velocity of the pulse ν_g. α is the linear gain coefficient and $A = A(z,t)$ is the slowly varying pulse envelope, which moves in the propagation direction z, similar to the envelope described in Eq. 2.2. The β parameters describe the dispersion as an expansion of $\beta(\omega)$ in a Taylor series around the carrier frequency ω_c as

$$\beta(\omega) = \beta_0 + (\omega - \omega_c)\beta_1 + \frac{1}{2}(\omega - \omega_c)^2\beta_2 + \frac{1}{6}(\omega - \omega_c)^3\beta_3 + \ldots, \tag{3.25}$$

where $\beta_0 \equiv \beta(\omega_0)$ and the rest of the parameters are defined as

$$\beta_m = \left(\frac{\mathrm{d}^m \beta}{\mathrm{d}\omega^m}\right)_{\omega=\omega_c} \qquad (m = 1, 2, 3\ldots). \tag{3.26}$$

The nonlinear parameter $\gamma(\omega_c)$ is defined as

$$\gamma(\omega_c) = \frac{\omega_c n_2}{c A_{\text{eff}}}, \qquad n_2 = \frac{2\overline{n}_2}{\epsilon_c n c}, \tag{3.27}$$

where n_2 is the nonlinear refractive index. The effective mode area A_{eff} is

$$A_{\text{eff}} = \frac{(\int\int_{-\infty}^{+\infty} |F(x,y)|^2 \,\mathrm{d}x\mathrm{d}y)^2}{\int\int_{-\infty}^{+\infty} |F(x,y)|^4 \,\mathrm{d}x\mathrm{d}y}. \tag{3.28}$$

To sum up, Eq. 3.24 describes the propagation of an ultrashort pulse in single-mode optical fibers. It accounts for the fiber losses via α and the chromatic dispersion through β_{i}, as well as nonlinearity of the optical fibers through γ. Concerning dispersion, the pulse envelope moves at the group velocity $\nu_g \equiv 1/\beta_1$, the effects of group-velocity dispersion (GVD) is contained by β_2 and the third order dispersion by β_3. The sign of β_2 may change with wavelength. When the wavelength is above the zero-dispersion wavelength λ_D, called anomalous-dispersion wavelength, the GVD parameter β_2 is negative and the fiber can support optical solitons. The term $\gamma(\omega_c)|A|^2 A$ describes the nonlinear effects of self-phase modulation (SPM). By neglecting third order dispersion (TOD) and losses, Eq. 3.24 reduces to a simple NSE:

$$i\frac{\partial A}{\partial z} - \frac{\beta_2}{2}\frac{\partial^2 A}{\partial t^2} + \gamma(\omega_c)|A|^2 A = 0. \tag{3.29}$$

3.4 Dispersion management

In optics, dispersion describes the phase velocity dependence of a wave (or the refractive index of a medium) on the frequency of the wave. The typical effect of dispersion, i.e. the spread of frequency components over time, typically causes the pulse to stretch temporally. Dispersion is an extremely important parameter especially for mode-locked lasers as well as chirped-pulse amplifiers since the dispersion needs to be compensated with high accuracy in order to reach the shortest output pulse durations. Dispersion management is done by introducing opposite sign of the dispersion into the system by balancing the total dispersion of a system e.g. by introducing a dispersive element with tailored dispersion properties.

Typical dispersion compensating elements are pairs of diffraction gratings [96], or a pair of Brewster-angled prisms [97]. However, such elements provide only limited degrees of freedom to compensate for higher order dispersion (such as third order dispersion), which is crucial for ultrashort pulses. In order to overcome this problem, combined prism and grating pairs can be used, and compression below 5 fs has already been achieved [98]. However, this combination for dispersion compensation suffers from higher losses as well as for high-power laser systems, prisms may introduce additional unwanted nonlinearities.

In fiber optics, specially tailored fibers, usually referred to as dispersion compensation fibers (DCF) can be used for dispersion management. DCFs were first used in telecommunications [99] in order to mitigate the dispersion-induced broadening of pulses as dispersion interferes with the detection process and limits the bandwidth of the signal. For ultrashort pulses, it is hard to compensate the GVD over the entire broad bandwidth of the pulse. To overcome this limitation, a special kind of DCF can be tailored in order to compensate for both β_2 and β_3 simultaneously. To compensate the dispersion for a fiber link containing two different fibers of lengths L_1 and L_2 the condition [93]

$$\beta_{21}L_1 + \beta_{22}L_2 = 0 \quad \text{and} \quad \beta_{31}L1 + \beta_{31}L_2 = 0 \tag{3.30}$$

should be met where β_{2j} and β_{3j} are the GVD and TOD parameters for the fiber of lengths L_1 and L_2. Additionally, fiber gratings [100] or liquid-crystal modulators [101] can also be used for dispersion compensation.

3.5 Amplification

The output pulse energies of mode-locked oscillators are typically limited to the nanojoule regime [80]. In order to reach higher pulse energies, amplification is needed.

The straightforward approach is to send the ultrashort pulse to a fiber amplifier to amplify the pulses directly as shown in Fig. 3.6 (a) or to a chain of amplifiers. However, since the fiber cores are typically in the order of several micrometers the output energy of the fiber amplifier is limited by nonlinearities such as self-focusing, stimulated Brillouin

scattering (SBS), SPM and stimulated Raman scattering (SRS) [14]. In order to mitigate

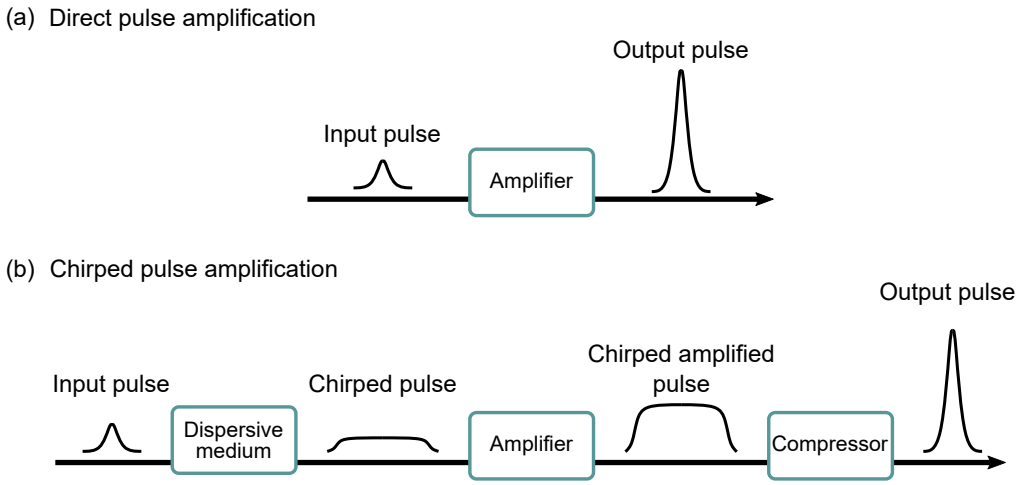

Figure 3.6: Illustration of direct pulse amplification (a) and chirped pulse amplification (b).

nonlinear effects in pulsed fiber systems, the CPA method [9] can be employed. In CPA, shown in Fig. 3.6, the pulses are first stretched in time, amplified in a fiber amplifier and finally recompressed to a pulse duration close to the input. In this way, the peak power of the pulse in the core is reduced in order to mitigate the nonlinearities.

High-power fiber lasers require larger core diameters, as in MMF, to reduce nonlinear effects. However, MMF fibers allow amplification for higher-order modes (HOM), which deteriorates the output beam quality and reduces amplification for the fundamental mode [102]. In order to keep single-mode-like behavior for the high-power output, large mode area (LMA) fibers can be used [103]. In LMA fibers, HOMs experience a larger loss compared to the fundamental mode. Alternatively, photonic-crystal fibers (PCFs) offer a brilliant solution to the same problem. In PCFs, the light is guided via the refractive index variation, which is created by microscopic and periodic array of air holes [104]. Specially after introduction of the rod-type PCFs [105], it is possible to amplify ultrashort pulses to over few kW range using coherent beam combining technique [106].

4 Development of a high-power Yb-based optical frequency comb

This chapter describes the development and performance of the high-power and long-term stable frequency comb laser system including its key sub-systems. An overview of the entire system is shown in Fig. 4.1. The system starts with an oscillator and its frequency comb stabilization (red boxes) and is followed by a chain of amplifiers, where CPA is utilized (gray box). The high-power output is sent to a multi-pass cell (MPC) (green box) for either post compression or a novel center wavelength tuning method, which utilizes the capabilities of the MPC and a phase and amplitude shaper placed in the CPA. Finally, the output of the MPC is sent to a femtosecond enhancement cavity (orange) in order to perform intra-cavity HHG. The entire system is protected by a technical interlock (blue), which enables fail-safe and long-term operation. The author developed the oscillator and its frequency comb stabilization, the entire CPA system, as

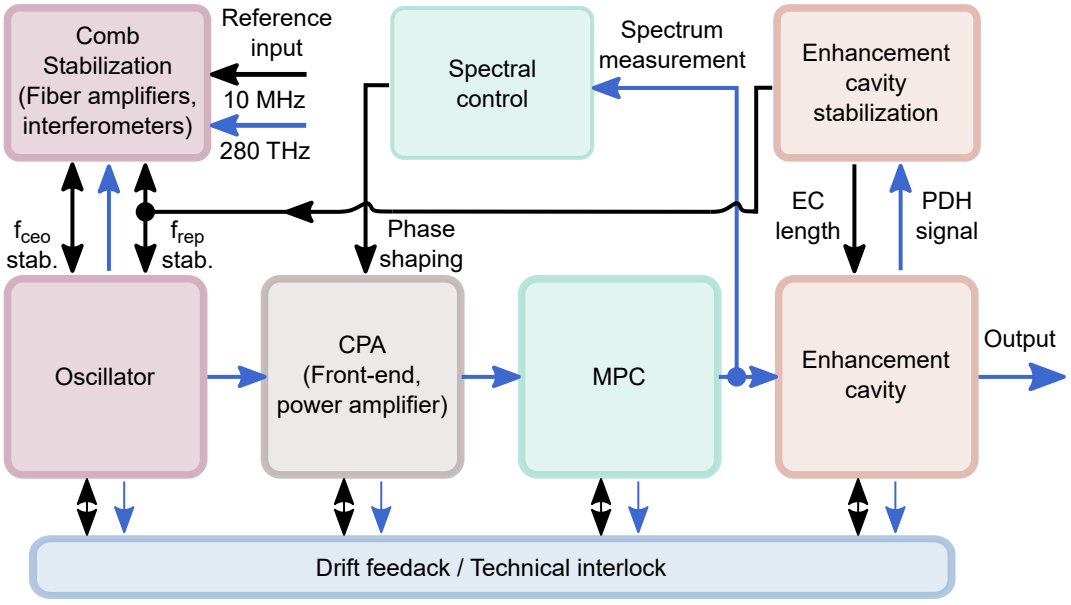

Figure 4.1: Laser system overview. CPA: chirped-pulse amplification, MPC: multi-pass cell, EC: enhancemenet cavity, PDH: Pound-Drever-Hall. Blue and black lines indicate optical and electrical signals, respectively.

well as the technical interlock and contributed to the rest of the building blocks indicated in Fig. 4.1.

4.1 Yb-based all-PM integrated NALM oscillator

As mentioned before in chapter 3, there are several ways for generating ultra-short pulses from a mode-locked optical cavity. In this dissertation an all-PM Yb:fiber based NALM oscillator is employed [107]. This oscillator type offers several advantages compared to other oscillators. In particular, NALM oscillators are very reliable, long-term stable and can be fully stabilized for frequency comb operation.

4.1.1 Optical setup

The all-PM Yb:fiber based NALM oscillator is designed in a way that all the components are fiber-based besides a mirror, which is used for cavity length locking. The schematic of the oscillator is depicted in Fig. 4.2.

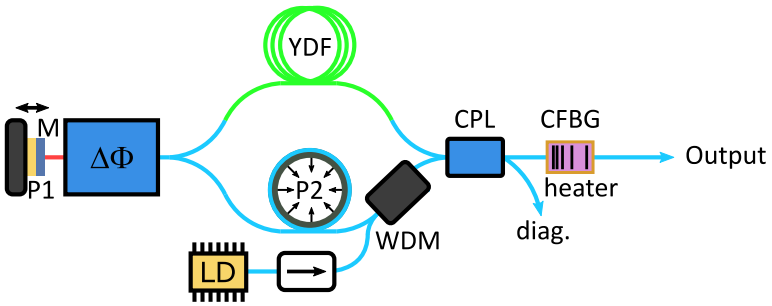

Figure 4.2: Schematic of the all-PM Yb:fiber based NALM oscillator. CPL: coupler, WDM: wavelength division multiplexer, LD: laser diode, CFBG: chirped fiber Bragg grating, YDF: ytterbium doped fiber, M: flat mirror, P1: linear piezo, P2: ring piezo, $\Delta\Phi$: non-reciprocal phase shifter.

The NALM oscillator contains two main parts: the loop and the linear arm. The loop of the oscillator consists of a 2 x 2 polarization maintaining (PM) fiber coupler with a 50:50 splitting ratio, a wavelength division multiplexer (WDM), a single-clad PM Yb-doped gain fiber (Yb401-PM, Coractive) and a non-reciprocal phase shifter in order to achieve mode-locking. To compensate for intra-cavity fiber dispersion, a chirped fiber Bragg grating (CFBG) is utilized, which also functions as an output coupler. The CFBG and its heater unit is placed in the linear arm. All fibers and fiber components used in the oscillator are PM and fast-axis blocked, where the blocking mechanism is based on micro-optics inside the respective fiber components. The phase shifter consists of a Faraday rotator and a $\lambda/8$ waveplate, which supplies the needed phase bias for stable

mode-locking, as discussed in section 3.2.1. The mirror (M) in the oscillator is glued to a linear piezoelectric element (P1), in order to tune/stabilize the cavity length of the oscillator. Additionally, PM980 fiber is glued onto the ring piezoelement (P2), again for tuning/stabilizing the cavity length. The pump diode (LD) has center wavelength of 976 nm and the maximum output power is 600 mW. The pump diode is protected by a pump protection filter (AFR PP-9806-N-B-1) against back-reflections. The optimal parameters for the fiber length in the loop, the pump power, the coupling ratio of the fiber coupler, the CFBG parameters as well as the active fiber's doping concentration were obtained via simulations using RP fiber power. In the linear arm, the fiber coupler delivers two fiber outputs, where one of them is used as a diagnostics port and the other one is spliced to the CFBG. The CFBG has a reflectivity of around 18% at 1030 nm center wavelength. The diagnostics port of the fiber coupler (Fig. 4.2 diag.) is sent to a photodiode to be used in the technical interlock, which will be discussed in chapter 5.

4.1.2 Characterization of output parameters

The pulse repetition rate of the Yb-NALM oscillator is 65 MHz. At the output, it delivers more than 10 mW of average power with roughly 18 nm spectral bandwidth at FWHM. The spectral comparison between the output (dark blue) and the diagnostics port (light blue) is given in Fig. 4.3.

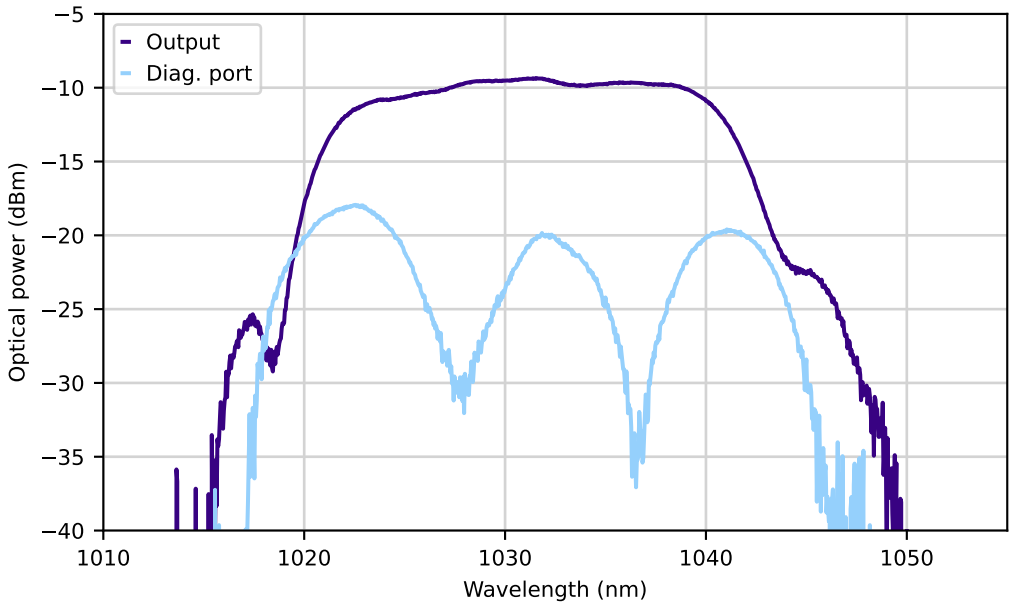

Figure 4.3: Characteristic spectra of the NALM oscillator. Spectra measured at output and diagnostic port are shown in dark blue and light blue, respectively.

The pulse repetition rate is measured via an RF spectrum analyzer (RIGOL DSA815)

and an InGaAs PIN photodiode (Discovery Semiconductors DSC50S) on a large span (Fig. 4.4 (a)), to ensure the single-pulse operation. Fig. 4.4 (b) shows a zoomed in RF spectrum with a signal to noise ratio (SNR) of roughly 60 dB for the carrier peak, at 30 Hz resolution bandwidth (RBW). The output pulse duration of the NALM oscillator is

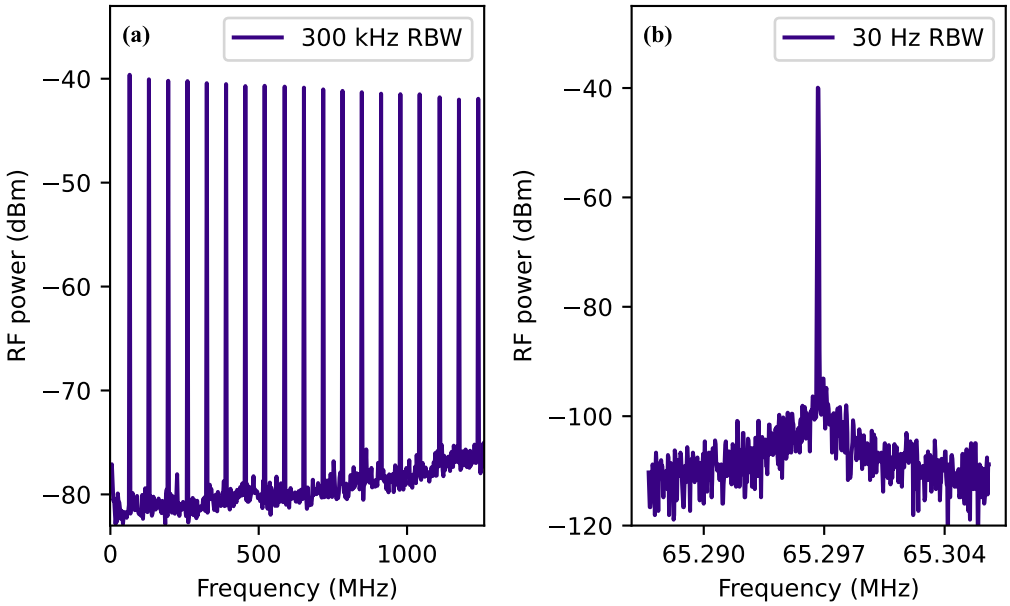

Figure 4.4: RF spectrum of the NALM oscillator recorded using two different resolution bandwidth settings.

measured to be roughly 1.2 ps which is positively chirped and can be compressed below 100 fs.

4.1.3 Optical frequency comb operation

The setup depicted in Fig. 4.5 is established for generating and measuring the oscillator's CEO beat note frequency (f_0), together with the optical beat note frequency (f_{CW}). The f_{CW} is obtained by beating a narrow line-width, CW non-planar ring oscillator (NPRO) (Coherent Mephisto) laser and the NALM oscillator's comb mode. Frequency comb stabilization is done via phase locked loops (PLLs). As an input signal for the PLL, the beat note signals are sent to the phase detector, which compares the phase of the generated beat note signal with an RF reference from a synthesizer (Rohde and Schwarz SML 03). The output of the phase detector is sent to a PID loop filter, whose output is then fed to the respective actuators for comb stabilization.

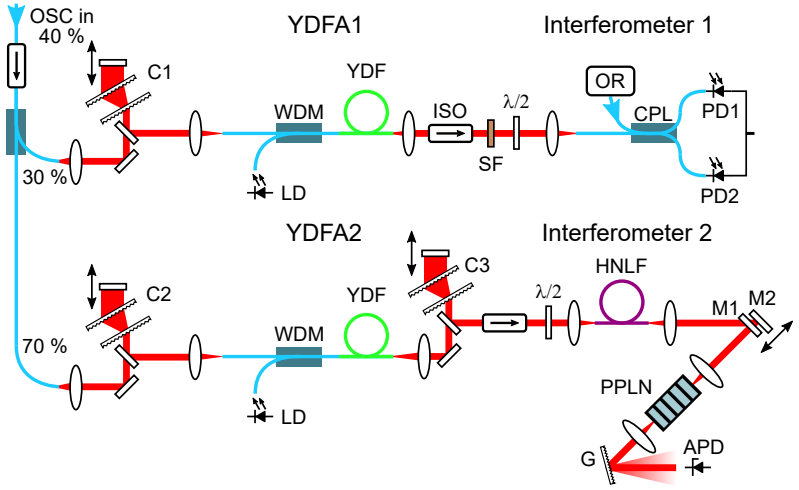

Figure 4.5: Schematic of the optical setup for frequency comb beat note generation and detection. C1-3: grating compressor, WDM: wavelength division multiplexer, LD: laser diode, YDF: ytterbium doped fiber, YDFA: ytterbium doped fiber amplifier, ISO: Faraday isolator, SF: spectral filter, OR: optical reference, CPL: coupler, HNLF: highly nonlinear fiber, PD1,2: balanced photo diode, M1: dichroic mirror, M2: silver mirror, PPLN: periodically poled lithium niobate, G: holographic grating.

The output of the oscillator is divided by a 60:40 fiber coupler. The 60% port is sent to the high-power amplifier chain, to be used as a seed. The remaining 40% is divided again for the beat note detection by a 70:30 fiber coupler. For f_{CW} beat note generation, the 30% output of the fiber coupler is first sent to a grating compressor (Fig. 4.5 C1) and then amplified by a fiber amplifier - YDFA1 (Fig. 4.5) - to 300 mW average power. The YDFA1 is a core-pumped amplifier, which consists of a 980/1030 nm WDM, a pump diode with 600 mW average power at 976 nm and a ytterbium doped fiber (Nufern PM-YSF-HI-HP). The reason for setting up a grating compressor before the amplifier is the wavelength difference between the NALM oscillator (1030 nm) and the reference laser (1064 nm). To

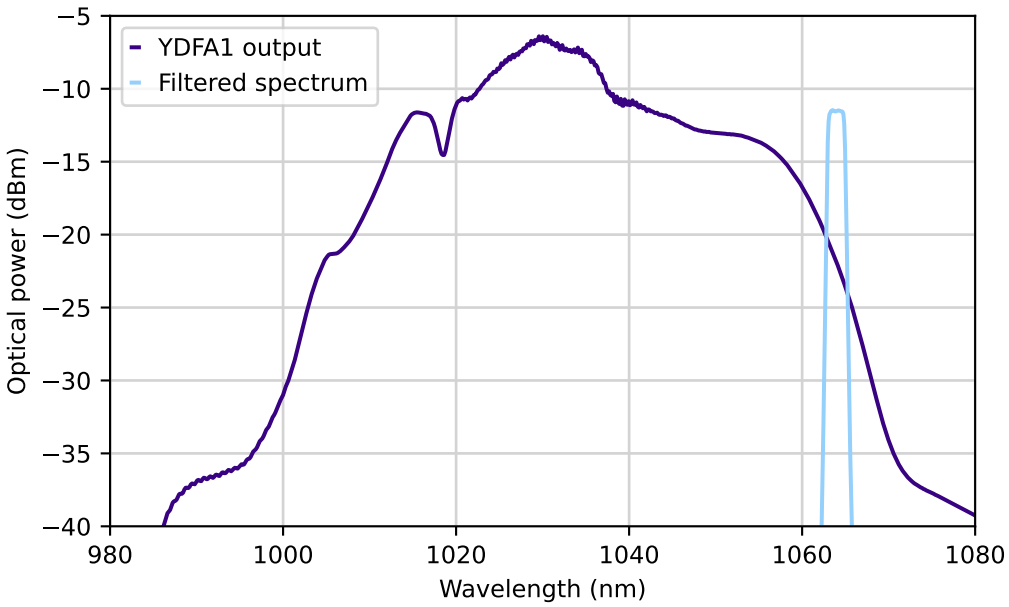

Figure 4.6: Output spectrum of YDFA1 (dark blue) and the portion, which is filtered out for beat note generation with a CW reference laser (light blue).

match the center wavelengths, a pre-chirp managed fiber amplifier is established in order to broaden the spectrum of the oscillator. The broadened spectrum is filtered using a spectral filter (Semrock LL01-1064-12.5) and then sent to interferometer 1, which consists of a 2x2, 50:50 fiber coupler and a balanced photodetector. Interferometer 1 is technically not an interferometer, since instead of recombining optically as is usually the case, here the signal is recombined electronically through the balanced photodetector. As it functions similiarly to one, it is called interferometer for the remainder of this thesis. The broadened and the filtered spectrum is shown in Fig. 4.6. The average power after filtering is about 1 mW. The polarization axis of the filtered light is tuned via a $\lambda/2$ waveplate before the interferometer, to match the polarization axes of two inputs. The optical beat notes, generated by beating the oscillator's output with the reference NPRO laser, is detected by a balanced photodetector (Thorlabs - PDB465C).

For CEO frequency f_0 detection, the 70% output of the fiber coupler is sent to a compressor (Fig. 4.5 C2) and then amplified via another pre-chirp managed amplifier, YDFA2 in Fig. 4.5. The broadened spectrum of YDFA2 in comparison with the oscillator's output is shown in Fig. 4.7. For f_0 detection, the amplified light is compressed via a second grating compressor (Fig. 4.5 C3). The reason for pre-compression prior to spectral broadening is to keep the pulse duration as short as possible in the HNLF in order to generate a coherent, octave-spanning spectrum [58]. The HNLF is a 14 cm piece of suspended-core fiber [108] and the output, which is broadened more than an octave, is shown in Fig.

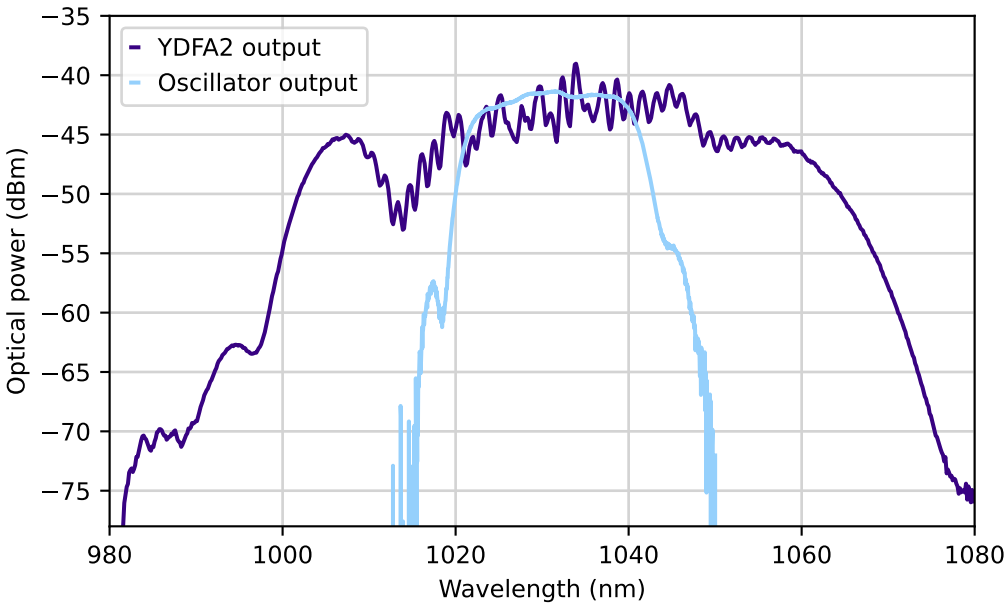

Figure 4.7: Output of YDFA2 (dark blue) in comparison with the output of the NALM oscillator (light blue).

4.8. The fiber ends of the HNLF are collapsed in order to seal the air holes to protect them against dirt. Microscope images are presented in Fig. 4.9. Before the compressed light is sent to the HNLF, it passes through an isolator and a $\lambda/2$ waveplate for isolation against back-reflections and matching the polarization axes of input light with HNLF, respectively. The output of the HNLF i.e. the octave-spanning supercontinuum, is then spectrally divided using mirrors M1 and M2. Mirror M1 is a dichroic mirror, which reflects the spectrum below 1000 nm and transmits above 1000 nm. Mirror M2 is a silver mirror, which reflects the transmitted spectrum above 1000 nm. M2 is placed on a linear stage to adjust the time difference in-between the blue and red part of the separated supercontinuum spectrum. Both beams are then sent to a periodically poled lithium niobate (PPLN) crystal, where second harmonic generation (SHG) is performed from the red side of the spectrum (reflection from M2). More specifically, $\approx$ 650 nm is generated via second harmonic from $\approx$ 1300 nm. The 650 nm light from the supercontinuum and the second harmonic are then sent onto an avalanche photo diode (APD) (Hamamatsu C5658) via a holographic grating (G, Thorlabs GH25-18V). This grating is used to filter/select the wavelength band, in which both f and $2f$ signals overlap.

To ensure long-term frequency comb stabilization without any phase slips, typically 30 dB SNR at 100 kHz RBW is required [109]. More than 30 dB SNR at 300 kHz RBW for f_0 and f_{CW} beat notes are shown in Fig. 4.14. The RF spectrum is measured via a radio frequency (RF) analyzer (RIGOL DSA815). The detected f_0 and f_{CW} beat note signals

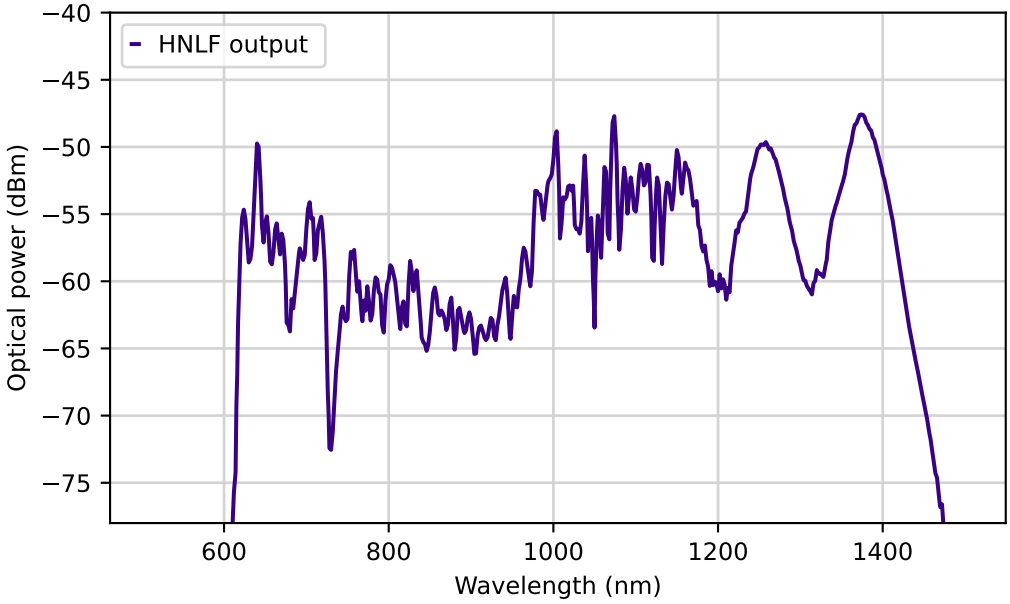

Figure 4.8: A more than octave spanning spectrum is generated in the HNLF.

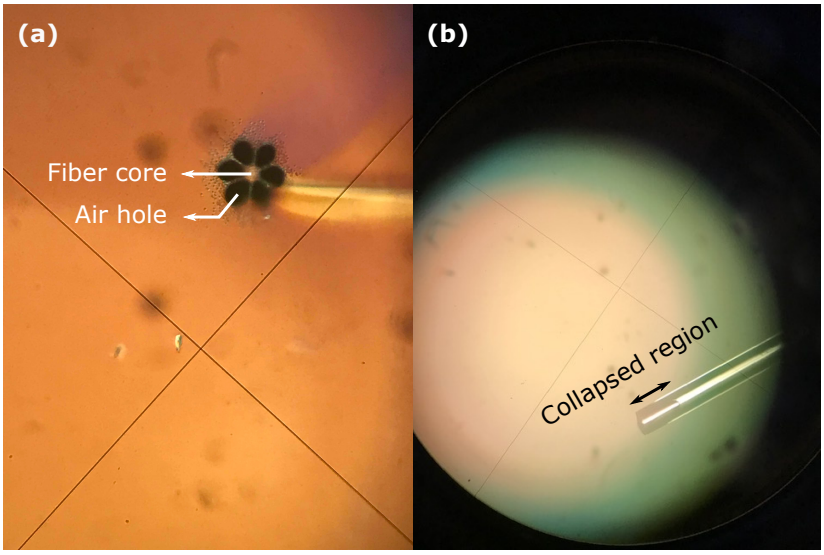

Figure 4.9: Microscope images of the used HNLF. The facet of the fiber is shown in (a) where the fiber core and the air holes are shown and the side image of the fiber is shown in (b) revealing the collapsed region of the fiber tip.

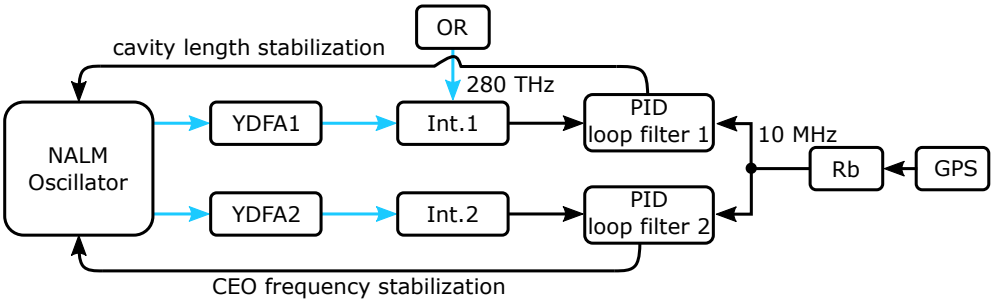

Figure 4.10: Comb stabilization concept. Int: interferometer, PID: proportional-integral-derivative, OR: optical reference, Rb: Rubidium clock. Blue and black lines are for optical and electrical cables, respectively.

are sent to the stabilization electronics for conditioning. They are filtered, amplified, divided using RF components and mixed on a phase detector with the RF references (RF synthesizers), in order to create an error signal, which is needed for stabilization. The stabilization setup is shown in Fig. 4.10. To minimize the long term drift of the RF equipment, a rubidium clock is utilized. The Rubidium clock provides a 10 MHz RF reference reaching an accuracy of 10^{-11} over a second, which decreases to 10^{-9} within a few hours. In order to keep its accuracy at 10^{-11} level, it is referenced to the Global Positioning System (GPS) with typical accuracy of 10^{-12} over several days on the one pulse per second (PPS) level. The error signal received from the phase detector is fed to the PID loop filter, which generates a feedback signal. Two different PID loop filters are used in the frequency comb stabilization setup. For compensating the fast jitter, an in-house developed analog PID loop filter with more than 1 MHz of electrical bandwidth is used. To compensate slow drifts, a field-programmable gate array (FPGA) based digital PID loop filter called RedPitaya [110] is used. The choice to use a digital PID loop filter helps to remotely control the beat note signals regarding their frequency tuning and remote stabilization. A 10% portion of the analog PID loop filter's output signal is used as an input to the digital PID loop filter after low-pass filtering. This configuration enables de-coupling of the fast feedback loop from slow drift compensation.

Besides the electronic feedback circuit, the response of the actuators, which are used for frequency comb stabilization, also play a key role, especially for fast signals. To analyze the response, transfer function measurements are performed for P1 (Fig. 4.2) and the pump diode driver of the oscillator.

The transfer function is defined as the ratio between frequency-dependent photodiode voltage and the modulation voltage. For determining the transfer function of the pump diode driver, the driver's current is modulated using a vector source analyzer (Hewlett-Packard 89440A) and the response is measured by the photodiode, which is aligned to the output of the oscillator. The transfer function measurement for P1 is done via an

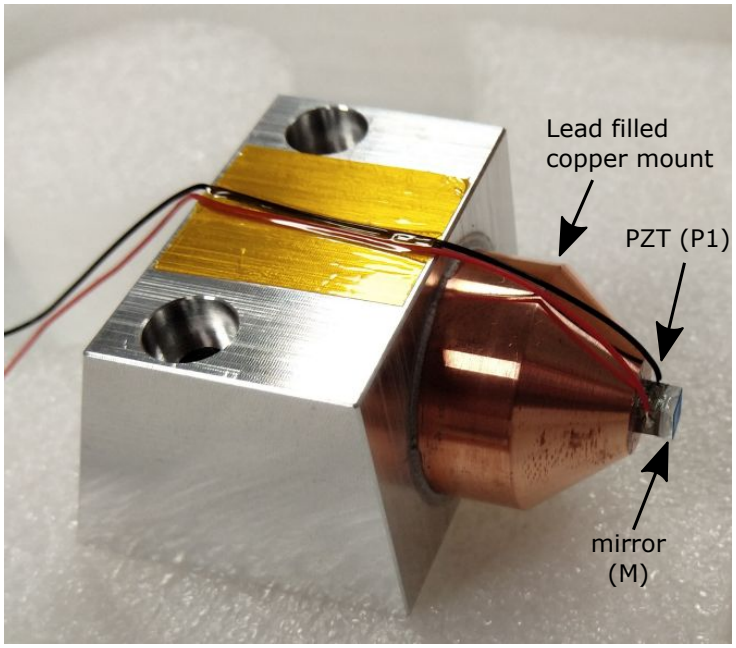

Figure 4.11: Mirror assembly of the Yb:NALM oscillator. A square mirror (M) is glued onto a PZT (P1). This is glued on a lead-filled copper mount, in order to damp the oscillations and increase the bandwidth of the actuator.

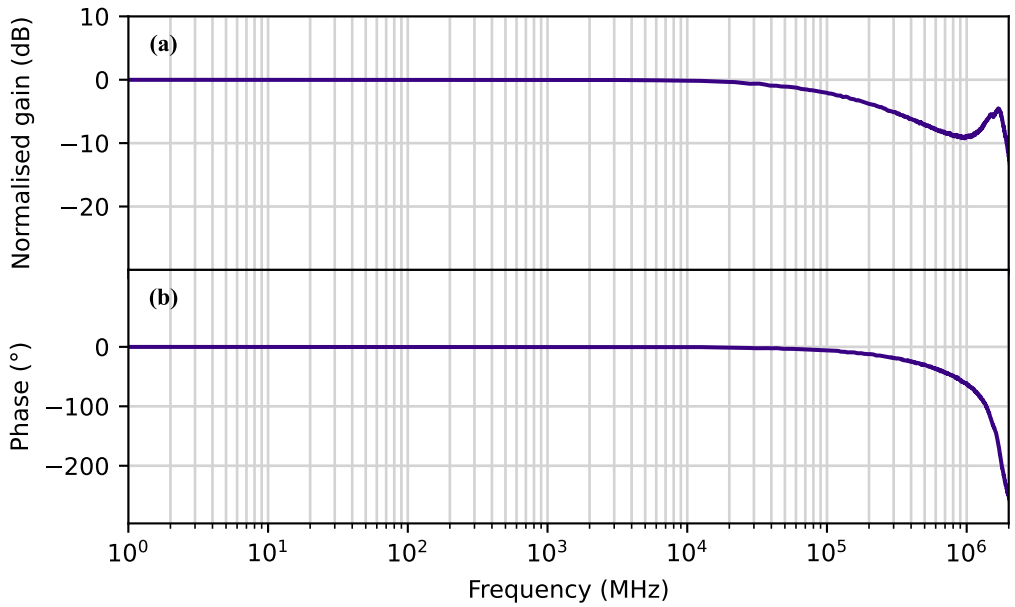

Figure 4.12: Transfer function of the diode driver to the Yb:NALM oscillator's output power for pump-current modulation.

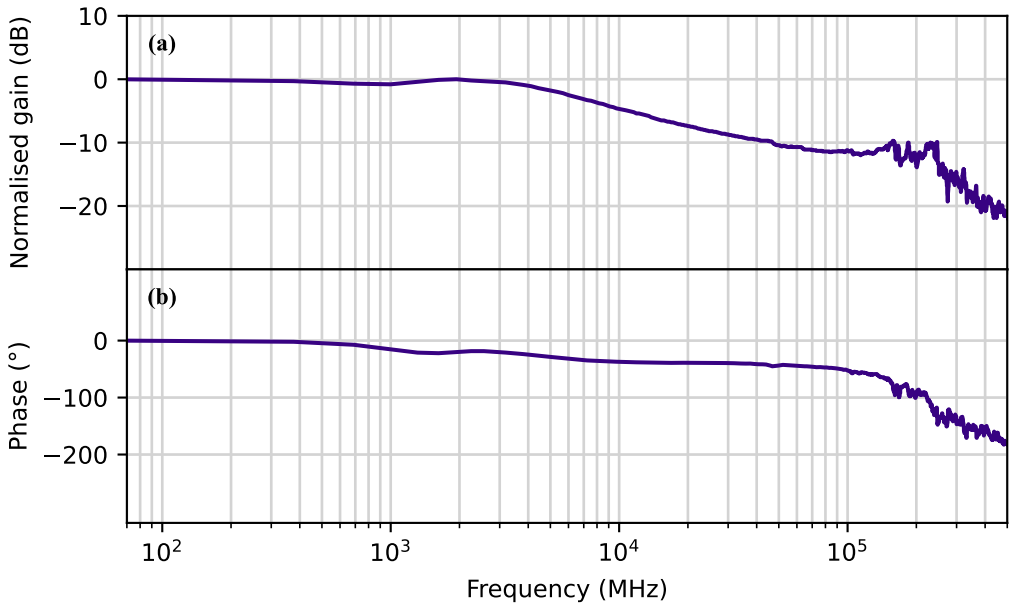

Figure 4.13: Transfer function of the mirror assembly from the Yb:NALM oscillator measured via in-house built Michelson type interferometer.

in-house built Michelson type interferometer, close to the reference [111]. To increase the bandwidth of the mirror assembly, the reference [112] is followed. The mirror assembly is shown in Fig. 4.11. Measurement results are shown in the Fig. 4.12 and Fig. 4.13. For P1 more than 100 kHz and for the pump diode's current driver roughly 1 MHz of bandwidth is detected.

The in-loop phase noise measurement shown in Fig. 4.15, reveals an integrated phase noise for both stabilized f_0 and f_{CW} beat notes of below 110 mrad. A signal source analyzer (SSA, Keysight E5052B) is used for measuring the single-sideband power spectral density phase noise. The servo bumps, which is a broad noise peak caused by the finite loop bandwidth, appear to be around 70 kHz for both measurements. In order to minimize the cross talk between two stabilizations, the PID parameters are carefully tuned to an optimum point, where a phase-slip free operation is ensured. The out-of-loop phase noise measurements, using identical interferometers depicted in Fig. 4.5, are shown in Fig. 4.16. For out-of-loop measurements, a fraction of the high-power compressed output is coupled into the respective interferometers. While the measurement for f_{CW} is in good agreement with its in-loop measurement, f_0 shows higher phase noise levels. Low-frequency noise can be attributed to the coupling difficulties into the HNLF with a 2.3 µm core diameter and the 4 m of beam path to the interferometer. High-frequency noise can be explained by the amplitude-to-phase noise conversion, caused by the amplification and nonlinear processes within amplifiers [113]. This high frequency noise, which is caused by the multi-branch

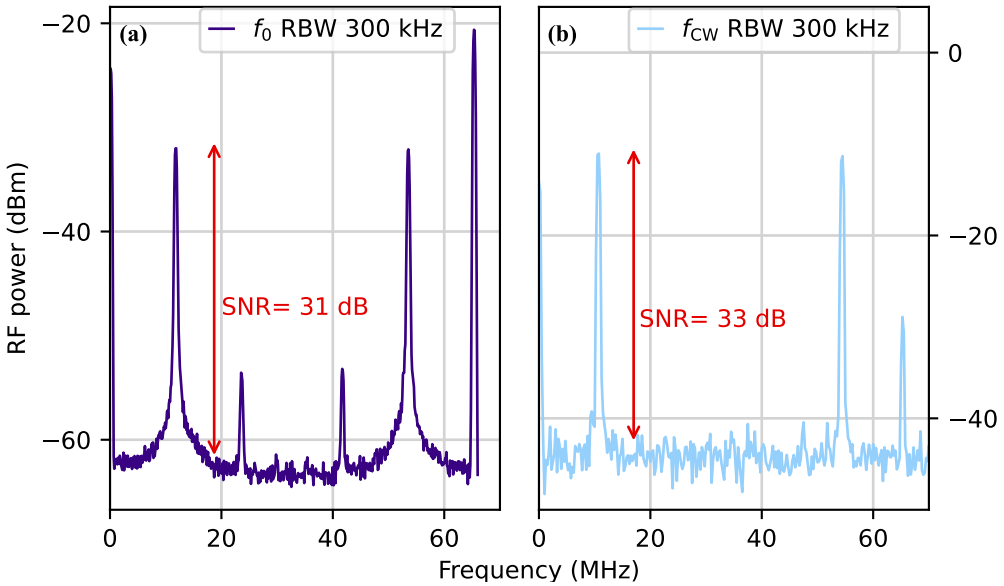

Figure 4.14: SNR of the detected beat note signals used for frequency comb stabilization. For both beat notes, more than 30 dB SNR is targeted at 300 kHz resolution bandwidth of the RF analyzer.

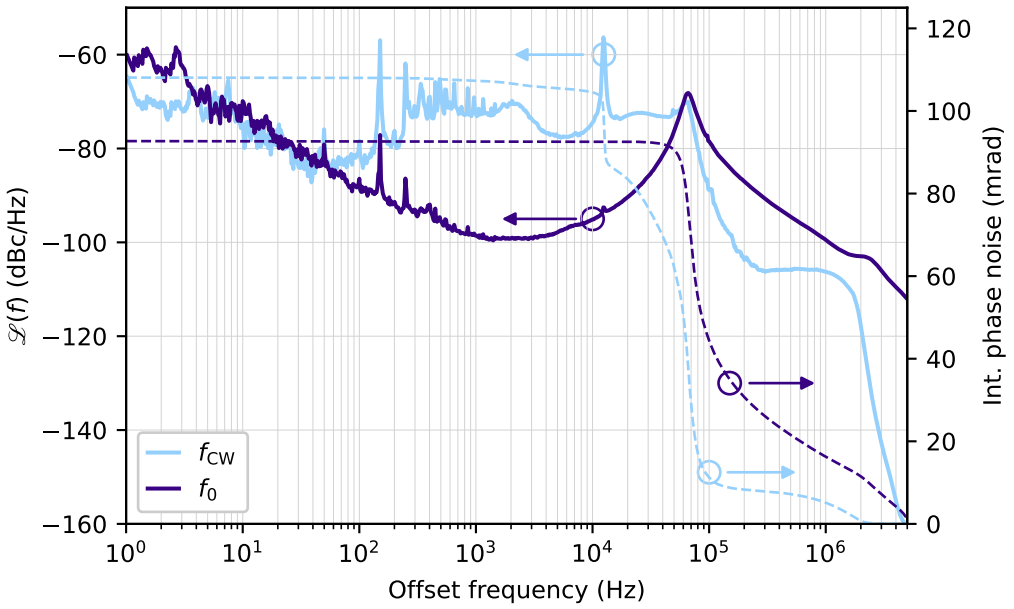

Figure 4.15: Single-sideband phase noise power spectral density of both stabilized f_0 and f_{CW} beat notes, along with integrated phase noise from 1 Hz to 5 MHz.

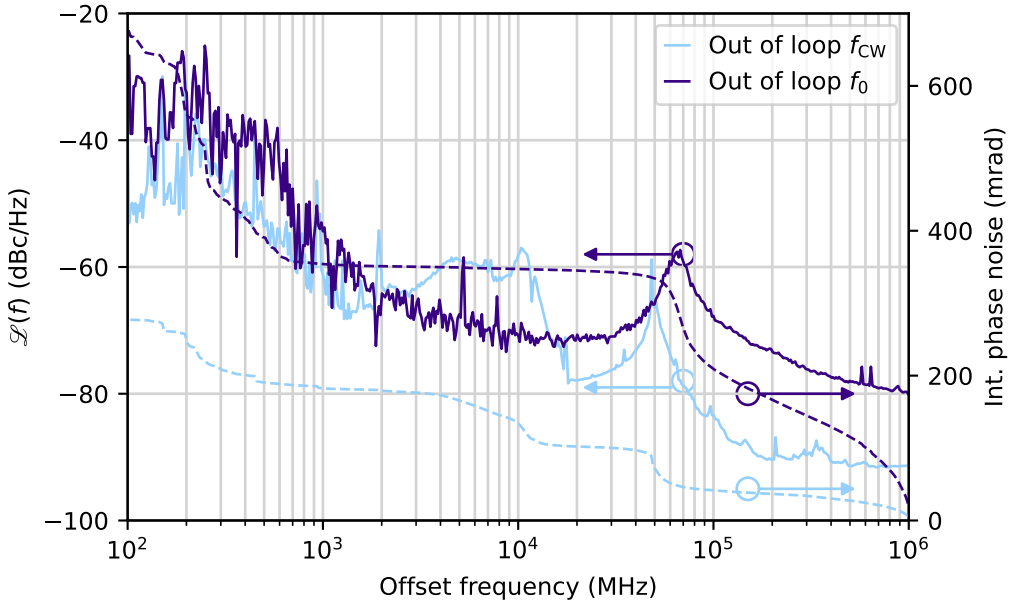

Figure 4.16: Out-of-loop single-sideband phase noise power spectral density of both stabilized f_0 and f_{CW} beat notes, along with integrated phase noise from 100 Hz to 1 MHz

.

architecture of the system, can be compensated [114].

The long-term frequency comb operation is performed, while the system is running at maximum output power at 72.6 W, which will be discussed in section 4.3. Long-term and phase-slip free frequency comb stabilization is shown in Fig. 4.17, measured via a frequency counter at 1 second gate time. The in-loop measurement shows excellent frequency stability without any phase-slip for both stabilized f_0 and f_{CW} beat notes over a 72 h period. Frequency fluctuations after stabilization are ± 16 mHz for f_0 and ± 4 mHz for f_{CW}.

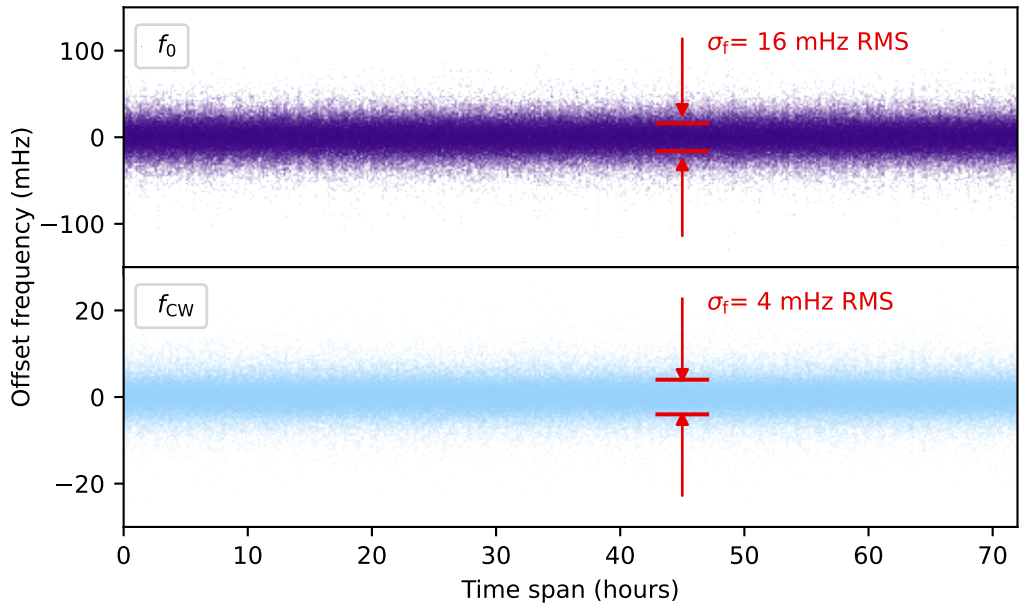

Figure 4.17: Long-term frequency comb stabilization for locked f_0 and f_{CW} beat notes measured via frequency counter. f_0 and f_{CW} beat notes are locked for 72 hours without any phase-slips with rms frequency fluctuations of 16 mHz and 4 mHz respectively.

4.1.4 Cross-gain modulation

The widely employed pump current modulation method is used for stabilizing the fast carrier-envelop phase frequency jitter. However, the feedback bandwidth of this method is limited by the gain lifetime of the active medium, as well as by the oscillator cavity dynamics [115]. To overcome this limitation, alternative methods are introduced [60], [116], [117]. These methods show the use of different actuators such as AOMs, EOMs or SESAMs to increase the feedback bandwidth, while sacrificing the simplicity of the traditional method. A more recent approach for CEO frequency stabilization relies on modulating the laser gain, using an auxiliary laser, which is called cross-gain modulation (XGM). Modulating the laser gain is found to be beneficial to overcome lifetime-induced

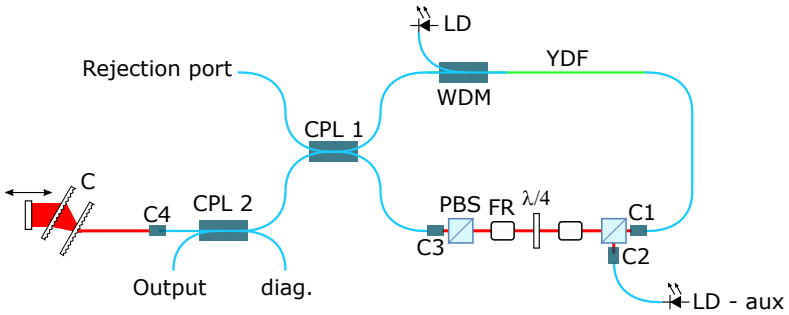

Figure 4.18: Experimental setup of the NALM oscillator used for XGM studies. LD: laser diode, LD - aux: laser diodes as auxiliary laser, C1-4: collimators, PBS: polarizing beam splitter, FR: Faraday rotator, C: compressor, WDM: wavelength division multiplexer, CPL1,2: fiber couplers, blue: passive fiber, green: active fiber and red: free space beam.

bandwidth limitations [118], [119]. The method is also implemented in the framework of this thesis in order to increase the locking bandwidth for f_0 stabilization. The XGM method is implemented using the first iteration of the NALM oscillator, which is shown in Fig. 4.18. This oscillator is the free-space version of the current oscillator. In order to utilize the phase bias required for mode-locking, a pair of polarizing beam splitters (PBS) and a pair of Faraday rotators (FM) are used, with a quarter wave plate (QWP) placed between them. Dispersion compensation is done via a pair of transmission gratings. The XGM method is introduced to the oscillator by injecting auxiliary laser light via an unused port of the PBS through collimator C2 (Fig. 4.18). The auxiliary laser light passes through the active fiber and then gets blocked by the fiber coupler, since the injection is done from the fast axis. In this way, it is possible to act on the gain dynamics of the oscillator, while ensuring that the auxiliary laser light is not appearing in the oscillator output. Two different wavelengths are used as auxiliary laser wavelengths: 1025 nm and 1080 nm. The maximum average power is limited to 4 mW. To characterize the achievable bandwidth, transfer function measurements from the laser current of the laser diode driver

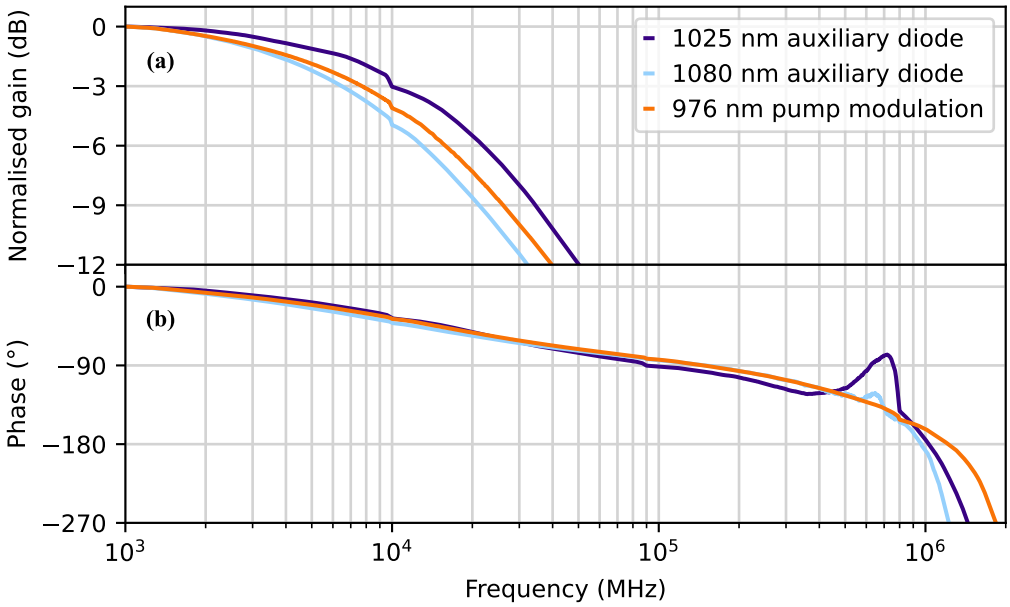

Figure 4.19: Transfer function of the diode driver to the NALM oscillator's output power for pump current modulation (orange) and for XGM (dark blue for 1025 nm and light blue for 1080 nm auxiliary diodes). (a) shows gain, (b) shows the phase. All curves are set to 0 at 1 kHz offset frequency.

to the oscillator's output power are performed, as shown in Fig. 4.19. After obtaining more than 25 dB SNR from the f_0 beat notes at 100 kHz of resolution bandwidth, f_0 stabilization was achieved for both techniques, including two different auxiliary laser wavelengths for the XGM method. The same stabilization concept introduced in Fig. 4.1.3 is used. For both methods, a locking bandwidth of roughly 350 kHz is obtained by careful tuning of the PID parameters. In-loop, integrated f_0 phase noise from 10 Hz to 1 MHz of 135 mrad, 157 mrad and 206 mrad is achieved for the pump modulation method, the XGM method - 1080 nm and the XGM method - 1025 nm, respectively. The single-side band power spectral density phase noise measurement is presented in Fig. 4.20.

In summary, introducing the XGM method for stabilizing the fast f_0 jitter did not reveal an improved locking performance, although a tight lock is achieved for two different auxiliary laser wavelengths. Eventually, the traditional method is used for f_0 stabilization for the remainder of this thesis including stabilization of the high-power comb system.

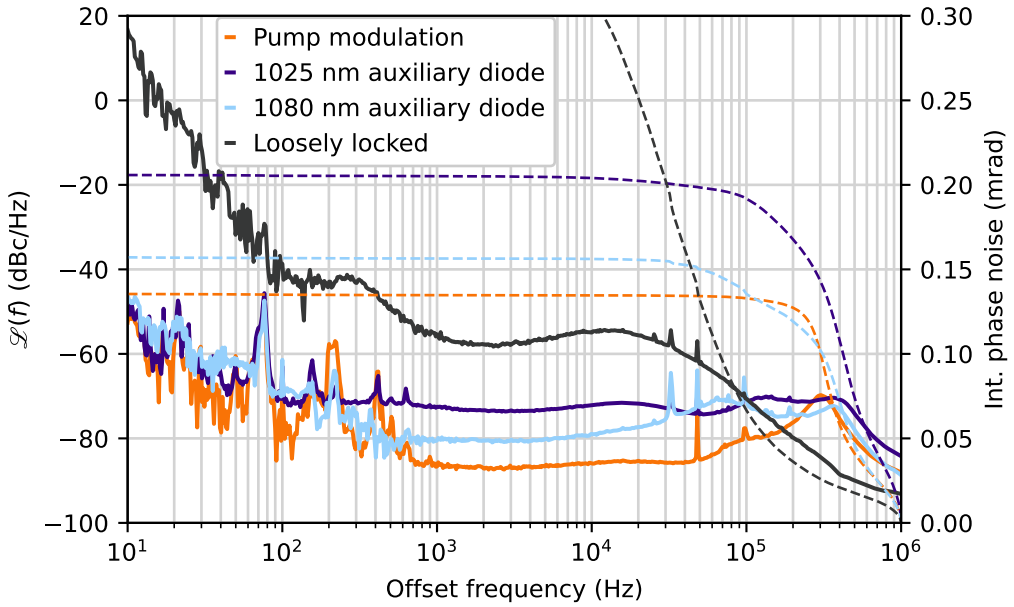

Figure 4.20: Single-sideband phase noise power spectral density (solid lines) and the integrated phase noise (dashed lines) of the stabilized CEO frequency beat signals, including two different stabilization methods (orange, dark blue and light blue) together with the loosely locked scenario (dark grey). Integration is done from 10 Hz to 1 MHz.

4.2 Front-end

The design of the ultrafast high-power amplifiers branches into two main paths regarding the nonlinearity. The nonlinearity caused by the short pulse durations is either used [120]–[122] for spectral broadening after amplification and finally shorter pulse durations, or it is avoided by introducing a large amount of group delay dispersion (GDD) [39], [123]–[126]. For frequency comb applications, the B-integral or the accumulated nonlinear phase shift, is preferred to be kept as low as possible, in order to reach good coherence properties. In contrast, in pre-chirp managed amplification, where the accumulated nonlinear phase shift is relatively high, the amplitude noise of the high power pump diodes can degrade the phase noise of the amplified frequency comb system via amplitude-to-phase noise coupling. Contrary to the amplifiers described in section 4.1.3, linear CPA is used for high power amplification. In the front-end, the pulses from the oscillator are chirped and amplified to be used as seed for the power amplifier, which will be discussed in section 4.3

4.2.1 Optical setup

The front-end of the system after the oscillator is shown in Fig. 4.21 and starts with a fiber-based pulse stretcher. The output of the oscillator is directly spliced into the fiber stretcher, which consists of a widely used PM980 fiber. The stretcher is followed by a core-pumped fiber amplifier (YDFA3 Fig. 4.21). YDFA3 contains a PM-WDM, a 976 nm

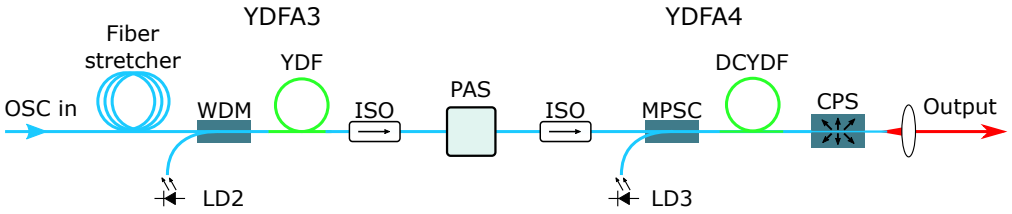

Figure 4.21: Simplified optical sketch of the front-end. LD: laser diode, WDM: wavelength division multiplexer, YDF: ytterbium doped fiber, ISO: Faraday isolator, PAS: phase and amplitude shaper, MPSC: multi-pump and signal combiner, DCYDF: double-clad ytterbium doped fiber, CPS: cladding power stripper, YDFA: ytterbium doped fiber amplifier.

laser diode with 600 mW average power and 0.9 m of ytterbium-doped active fiber (Nufern PM-YSF-HI-HP). The output of the YDFA3 reaches 300 mW average power. The design of the front-end has evolved throughout the work of this dissertation. In the initial design, YDFA3 is followed by an another fiber stretcher (Fig. 4.22) in order to compensate for third order dispersion accumulated in the system. Afterwards, the design has changed and instead of a second stretcher fiber, a phase and amplitude shaper (PAS) is added to the system. It is used in order to compensate for second and third order dispersion and more importantly, for enabling the center frequency shifting of the output, which will be discussed in Chapter 6. The dispersion engineering will be discussed in depth in the next section. The output of the PAS is directly sent to the second amplifier in the system, which is cladding pumped. This amplifier consists of a polarization-maintaining multi-pump and signal combiner (PM-MPSC), a 976 nm wavelength stabilized fiber-coupled laser diode for pumping and 1.5 m double-clad ytterbium-doped active fiber (Nufern PLMA-YDF-10/125). The optimum length of the active fiber was determined via numerical simulations using a commercial fiber-software (RP fiber power). The simulation resulted in 2.5 m of active fiber length for most efficient amplification as shown in Fig. 4.23. However, a shorter fiber length resulting in less efficient amplification was chosen to keep the B-integral lower and to minimize spectral re-shaping within the amplifier. Both aspects are important for the spectral tuning scheme implemented later-on (Chapter 6). Shorter fiber length increases the required pump power and also causes elevated unabsorbed pump power levels at the output of the active fiber. In order to remove the unabsorbed pump, a cladding power stripper (CPS) is spliced to the end of the active fiber. The fiber output

of the CPS is angle cut and glued in a glass ferrule to improve the mechanical stability of the fiber output. The output is then sent to the power amplifier to be used as a seed.

4.2.2 Dispersion engineering

In order to implement a CPA scheme, the pulses need to be stretched before amplification to avoid nonlinearities. Generally, two different designs for stretching are preferred, for building an all-fiber-based stretcher or a grating-based stretcher. Although grating-based stretchers have some advantages compared to fiber stretchers such as ease of tuning the dispersion parameters, no demand for splice etc., due to the fact that grating-based stretchers are free-space, they are much more sensitive to environmental changes compared to their fiber counterparts. Hence, an all-fiber stretcher design is chosen.

For the initial CPA design, dispersion management is done by a combination of a PM980 fiber, an OFS stretcher (OFS FemtoComp) fiber and a grating compressor. Initially, roughly 70 m of PM980 is used for introducing a large amount of positive GDD for stretching the pulses. However, PM980 and the grating compressor also adds positive TOD. For compensating the TOD, an OFS stretcher fiber is used, which adds negative TOD together with positive GDD. Finally, after amplification, the accumulated positive GDD is compensated via a grating compressor. The dispersion values are shown in table 4.1.

Table 4.1: Initial dispersion management design

Section	GDD(ps^2)	TOD(fs^3)
Fiber stretcher	1.90	2.9 x 10^6
OFS	2.6	-15 x 10^6
Grating compressor	-4.57	12 x 10^6

The setup for the OFS fiber is shown in Fig. 4.22. It consists of a polarization beam combiner (PBC), the OFS (TODCF) fiber and a Faraday mirror (FM). All fibers after the PBC, including OFS and FM, are non-PM. The input of the PBC is aligned for the slow axis, which transmits the light through the OFS fiber. After reflecting back from the FM, the polarization axis is rotated 90°and the PBC directs the light to the output port. The aim of building such a setup is to double pass through the OFS fiber using the FM, since the fiber's cost is relatively high. The output pulse duration using the initial dispersion management setup is about 217 fs, and shows remaining pre/post pulse structures, which will be discussed in section 4.3.3.

For the second iteration, a phase and amplitude shaper is added to setup for realizing a novel wavelength shifting method [127], which will be discussed in Chapter 6. It is also used for compensating second, third and fourth order dispersion by phase shaping. However, the device has limits and cannot compensate the GDD that TODCF introduces.

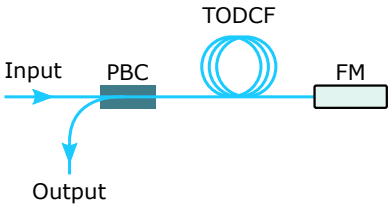

Figure 4.22: Initial dispersion management design for compensating the third order dispersion. PBC: polarization beam coupler/combiner, TODCF: third order dispersion compensation fiber (OFS), FM: Faraday mirror.

In order to match the GDD, about 90 m of extra PM980 fiber is added to the fiber stretcher. The residual mismatch of the GDD and TOD is then compensated via the PAS, while the grating distance from the grating compressor is kept constant. The dispersion values are provided in table 4.2. Since the PAS is computer-controllable, the parameters are easily tunable. In the initial design, the OFS fiber had a core diameter of about only 2.3 µm, which caused splicing difficulties. An intermediate fiber with roughly 4 µm core diameter is used in between PBC - OFS and OFS - FM splices. Also, a new splicing mode had to be tested and defined for the splices. By carefully tuning the parameters, 203 fs

Table 4.2: Current dispersion management design

Section	GDD(ps^2)	TOD(fs^3)
Fiber stretcher	4.37	6.6 x 10^6
Phase and amplitude shaper	0.23	-19 x 10^6
Grating compressor	-4.57	12 x 10^6

pulses are achieved after amplification and compression, revealing a clean temporal pulse structure.

4.2.3 Choice and characterization of output parameters

Following the rod fiber coupling guide for the high-power amplifier, the seed needs to reach at least 5 W average power in order to saturate the rod fiber. To have some headroom, a power level of 5.4 W was chosen. The length of the active fiber is simulated, targeting an output power of 5.4 W. Simulation results are shown in Fig. 4.23. The slope efficiencies, which are obtained by plotting the output power against the absorbed pump power for 1.5 m active fiber length is shown in Fig. 4.24. The simulations are performed using the before mentioned commercial RP fiber power software. Simulated and measured output spectra show excellent agreement for different fiber lengths. The displayed data also shows that the center wavelength of the output changes with fiber length, due to reabsorption. By keeping the fiber length short, it is possible to keep the center wavelength

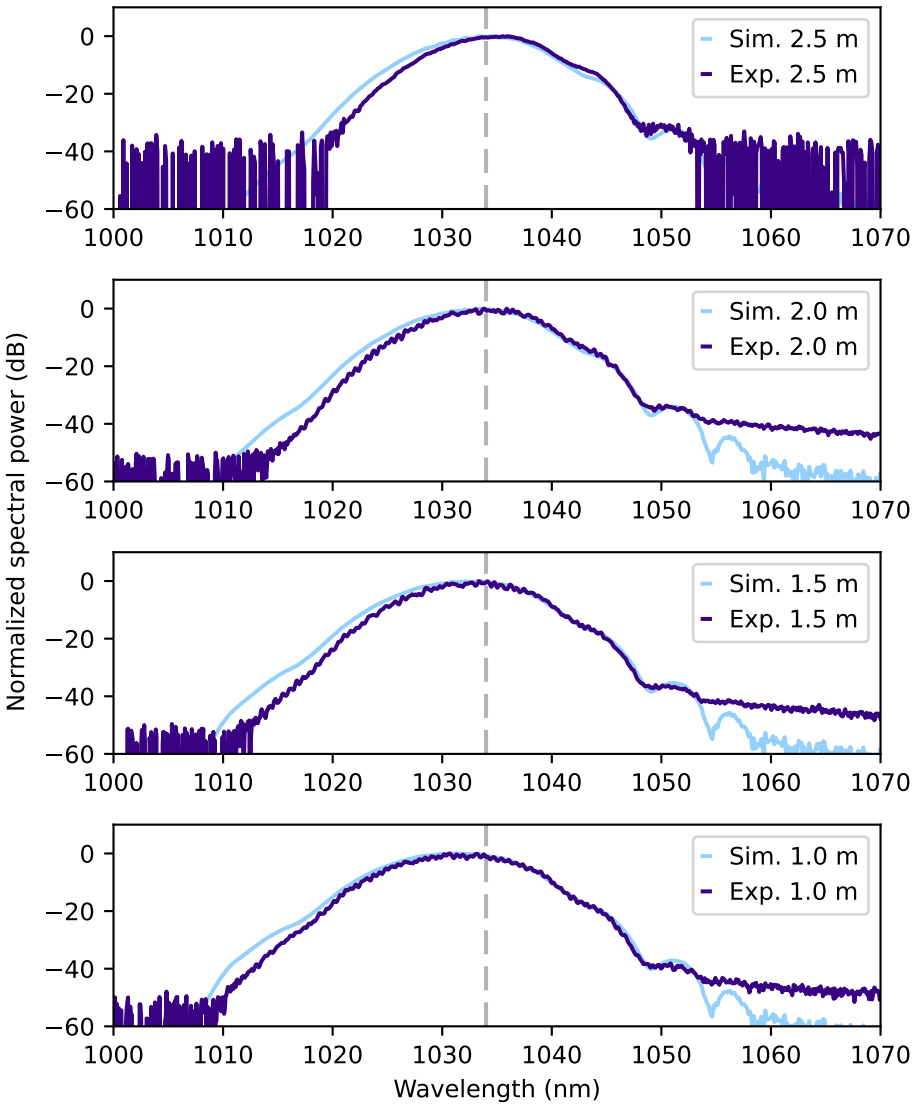

Figure 4.23: Output spectra comparison of YDFA4 after amplification using different fiber lengths for the active medium. Gray dashed line indicates the center wavelength for 2.5 m scenario of 1034 nm.

of the output close to the 1030 nm. As explained before, the slope efficiency drops with a shorter fiber length, which results in requirements for more pump power, in order to reach the same output power level. Using more pump power while keeping the active fiber length constant, results in unabsorbed pump power at the output. This leads to a temperature rise of the optical components and mounts in the beam path directed towards the power amplifier section, which then finally results in instabilities. In order to avoid this, a CPS is spliced at the fiber output of the front-end. The input and output fibers are

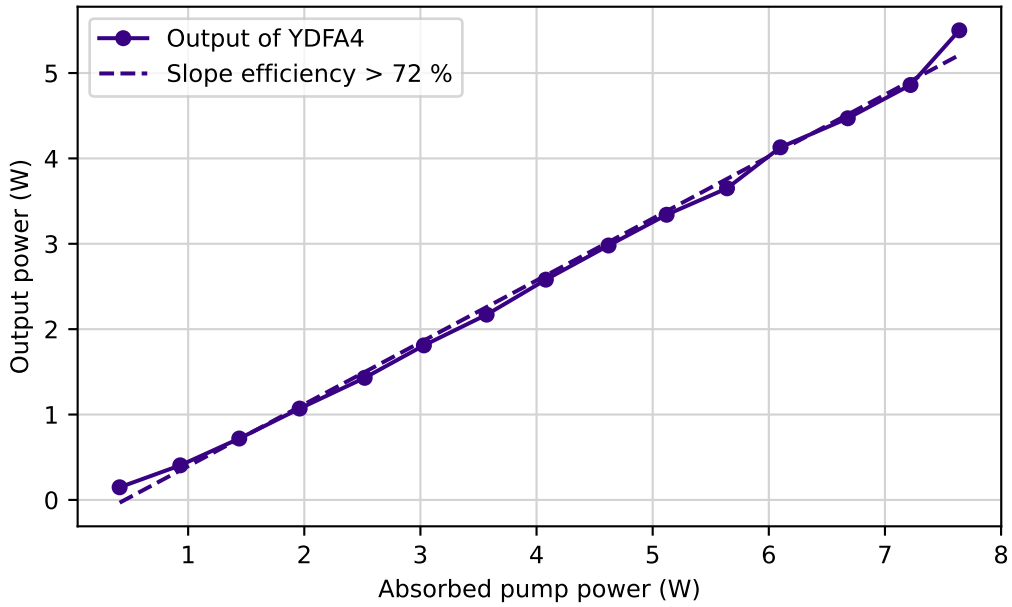

Figure 4.24: Measured slope efficiency of YDFA4 for reduced fiber length (1.5 m) to avoid nonlinearities displayed together with a linear fit (dashed line) indicating the effective slope efficiency.

kept as short as possible in order to reduce nonlinearities. The total fiber length of the CPS is about 30 cm and the unabsorbed pump at the output of the front-end is measured to be 14 mW.

The output of the front-end is compressed to check the compressibility of the pulses. Two dichroic mirrors (980 nm transmission / 1030 nm reflection) are used for pump-separation. The beam is then sent into a grating compressor, which consists of two transmission gratings (1000 lines/mm), a roof mirror and a d-shaped mirror. The grating distance is tuned to about 0.8 m and a fraction of the light is sent to a commercial frequency-resolved optical gating (FROG) for pulse characterization. The measured pulse duration and temporal phase is compared with the simulations depicted in Fig. 4.25. Simulations and experimental measurements fit extremely well. A pulse duration of 206 fs is measured with small pre- and post- pulses caused by the third order dispersion mismatch. The transform-limited pulse duration is around 190 fs. Measured and retrieved FROG traces are shown in Fig. 4.26, revealing good agreement and symmetry with less than 0.5 % FROG error. Additionally, the spectrum before and after compression, together with the retrieved spectrum from the FROG measurements are shown in Fig. 4.27, revealing again an excellent agreement.

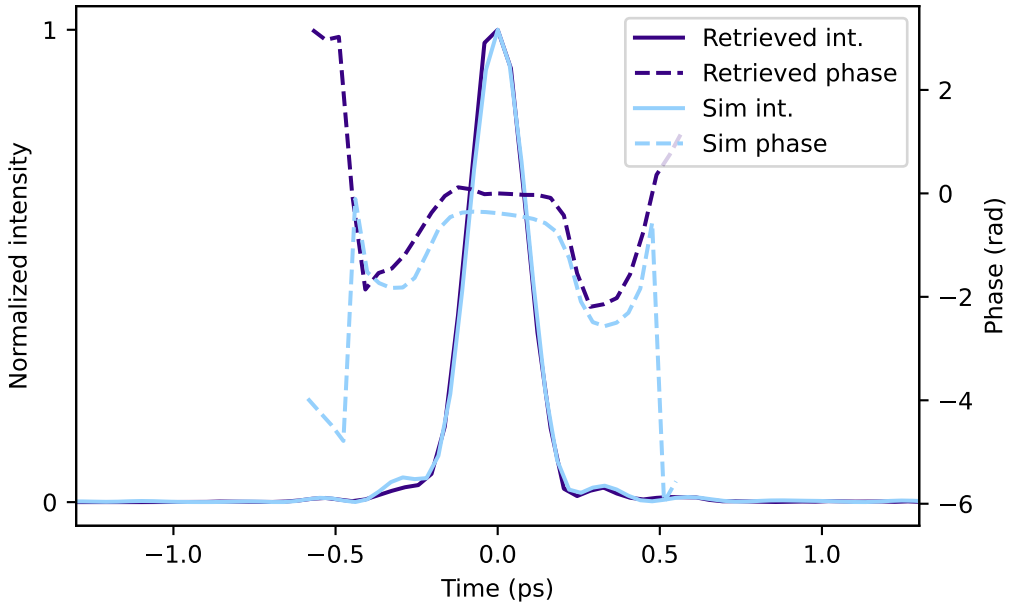

Figure 4.25: Measured (light blue-solid) and simulated (dark blue-solid) compressed temporal pulses displayed together with temporal phase (dashed light blue - measured, dashed dark blue - simulated).

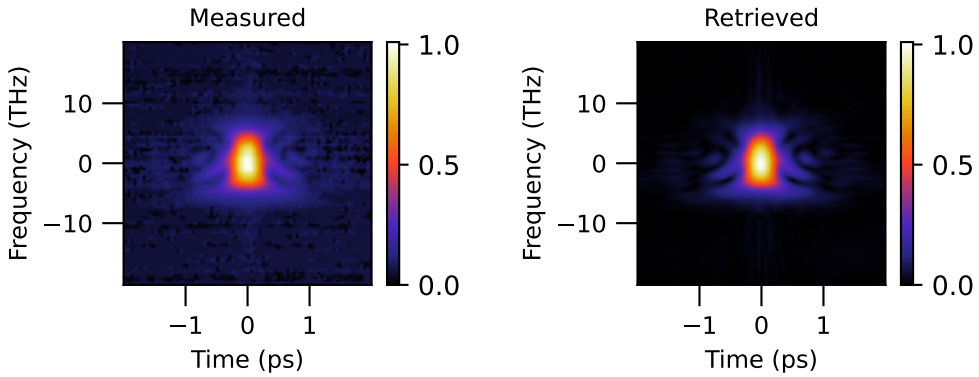

Figure 4.26: Measured and retrieved FROG traces for the compressed output of the laser front-end.

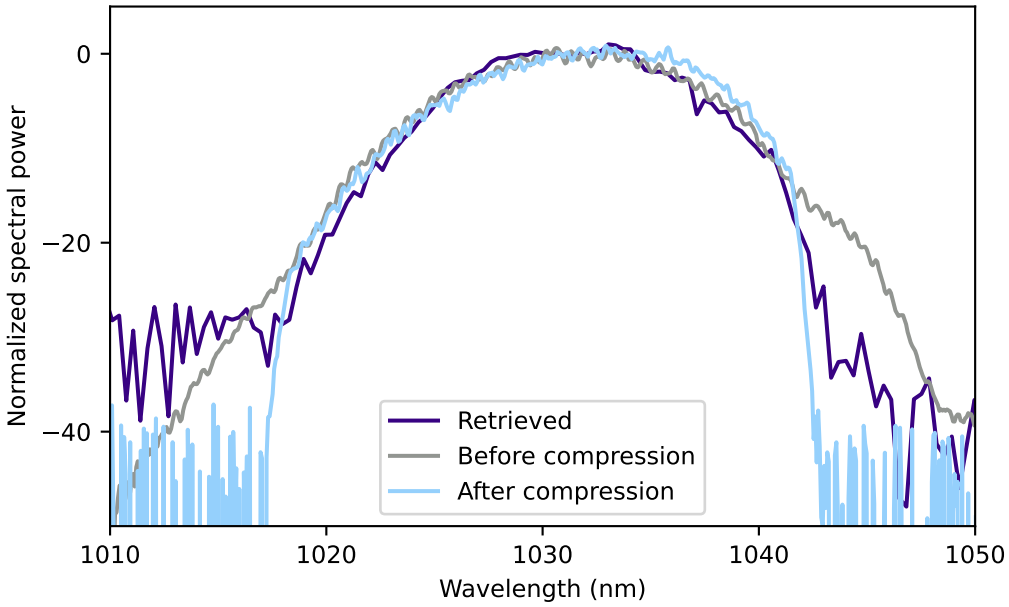

Figure 4.27: Spectra comparison of the front-end output. Spectrum retrieved from FROG, and spectra measured using an optical spectrum analyzer before and after the compression, shown in dark blue, gray and light blue, respectively.

4.3 Power amplifier and compressor

Ytterbium-based systems excel in average power scaling, due to the small quantum defect of ytterbium when pumped at 976 nm and the availability of highly doped gain media such as crystals and glasses [128], [129]. There are several Yb-doped gain media, which are suitable for high-power operation e.g., Yb^{3+} : YAG [130], Yb^{3+} : $CaGdAlO_4$ [131] and Yb-doped fibers [132].

One of the main obstacles in designing the power amplifier, is the thermal management of the active medium. Since the optical power levels of the pump and signal light can reach high average and peak power levels, design flaws usually end catastrophically. To mitigate this for the active medium, amplifier gain modules with built-in thermal management are often the preferred choice to avoid extra engineering. A PM ytterbium rod gain module (NKT Photonics areoGAIN-ROD) is chosen for the power amplifier. This module comes with a rugged aluminum casing and an integrated water cooling circuit, which assures efficient thermal management. Additionally, it has input and output anti-reflection coating and slightly angled end-caps, which already provides some protection against possible back-reflections. Moreover, the pump light in the rod type fiber is guided via air-clads with high damage thresholds and high NA, which makes it a reliable and easy-to-use choice for high-power amplification, which is aimed at reaching the 100 W regime.

Another important consideration is the beam diameter after amplification. The beam diameter at the output of the rod type fiber, which has a mode-field diameter of 45 µm, is around 1 mm after the collimation lens. Since the power levels are relatively high, a small beam diameter can easily cause thermal lensing especially inside the high power Faraday isolator. To avoid this problem, a beam expanding telescope is designed and implemented.

The CPA technique is very helpful for avoiding nonlinearities and boosting up the peak power of the amplifiers after compression. However, the distance between the gratings sets constraints if a compact setup is targeted. In addition, a large grating separation increases the risk for additional mechanical instabilities. To address these challenges, a compact compressor is developed.

4.3.1 Optical setup

The power amplifier and compressor of the system are shown schematically in Fig. 4.28. As mentioned before, the fiber output of the front-end is angle-cut at an angle of 8° to minimize back-reflections from the fiber facet and glued in a glass ferrule for enhancing the mechanical stability. The ferrule is placed on a 3-axis stage (NanoMax Stage - Thorlabs) for fine-tuning the beam. It is collimated using an aspheric lens (L1) (Thorlabs AL1512) with 12 mm focal length. Then the beam is guided onto a second aspheric lens (L2) (Asphericon AFL25-50-S-B) with 50 mm focal length, which is used for coupling the beam

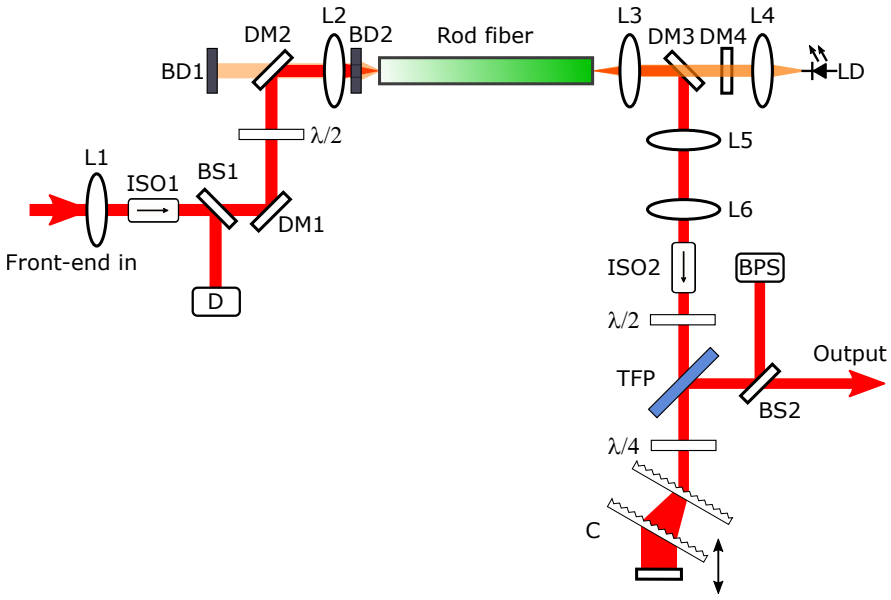

Figure 4.28: Optical sketch of power amplifier and compressor. ISO: Faraday isolator, L: lens, BS: beam sampler, D: diagnostics, DM: dichroic mirror, BD: beam dump, LD: laser diode, TFP: thin-film polarizer, C: compressor, BPS: beam pointing stabilization system.

into the rod type fiber. The beam is directed to the rod fiber through dichroic mirrors (DM1,2) to eliminate any residual pump light from the front-end and the power amplifier as it is counter-pumped. The reason for counter-pumping is an ease of adjustment and more importantly, to reduce the nonlinear phase shift accumulated in the rod fiber. In addition, a Faraday isolator (ISO1) (EO Tech Pavos 5 mm aperture) is placed along the path in order to protect the front-end from back-reflections, together with a $\lambda/2$ waveplate to tune the polarization axis. Additionally, there is a beam sampler (BS1) added for the technical interlock and other diagnostics, which will be discussed in the next chapter. In order to reduce thermal effects caused by unabsorbed pump light from the power amplifier, a water-cooled beam aperture is implemented after the second aspheric lens (L2), which lets the seed beam pass and partially blocks the more divergent pump light.

A wavelength stabilized, 240 W average power pump diode (Coherent DILAS D4F2S22-976.0,6-240C-IS58.1OW) with 976 nm center wavelength is used for continuous-wave pumping. The output of the pump diode has a delivery fiber which has a HP-SMA connector at the output with a sapphire end-cap. The core diameter of it is chosen to be 200 µm and the fiber NA is 0.22 to match the NA of the rod type fiber. It is fixed on a 3-axis stage and the pump light is sent to a cage assembly for coupling it into the rod type fiber, while guiding the amplified 1030 nm light out. The used assembly consists of two aspheric lenses with 30 mm (L4) (Asphericon AFL25-30-S-B) and 25 mm (L3) (Asphericon AFL25-25-S-B) focal length for collimating and coupling the pump light, respectively. L3 also

collimates the high-power output of the rod type fiber. In-between the lenses, dichroic mirrors with a 45° (DM3) and a 0° (DM4) angle of incidence (AOI) are placed for guiding the high-power output and for protecting the high-power pump diode, respectively. Specifications of the aeroGAIN rod fiber module are provided in table 4.3. The average

Table 4.3: Parameters of aeroGAIN-ROD-MODULE 1.1

Specification	Value
Signal wavelength	1030 nm to 1040 nm
Core diameter	57 µm
Pump cladding diameter	203 µm
Pump NA	0.58
Cladding absorption	$\approx$ 15 dB
PER[1]	17.4 dB
Optical efficiency	$\geq$ 60 %
M^2	$\leq$ 1.3
End-cap coating R@ 1030 nm	$\leq$ 0.2 %
End-cap coating R@ 976 nm	$\leq$ 0.3 %
End-cap angle, input	$\leq$ 0.5°
End-cap angle, output	2.0°$\pm$ 0.5°
Signal average power	$\leq$ 100 W
Dimensions (WxLxH)	35x817x35.2 mm
Recommended water temperature	25°C
Recommended water flow	$>$ 2 L/min
Operating temperature	20-30°C

[1] polarization extinction ratio

power at the output of the rod type fiber reaches above 120 W. The beam is guided into an expanding telescope via a highly-reflective dichroic mirror with a 22.5° AOI and two highly-reflective mirrors, all optimized for 1030 nm (not drawn in Fig. 4.28 for simplicity). The beam expanding telescope consists of a −50 mm (L5) and a 300 mm (L6) focal length aspheric lens, in order to expand the beam diameter by a factor of roughly six before the high-power isolator. The isolator (ISO2) (EO Tech Pavos Ultra) used for protecting the power amplifier against back-reflections has a 12 mm optical aperture. Afterwards, the beam is guided to the compressor section of the system.

4.3.2 Compact compressor design

The compressor design is shown in Fig. 4.29. The light passes through a TFP before entering the compressor. The compressor of the system consists of a $\lambda/4$ waveplate, a

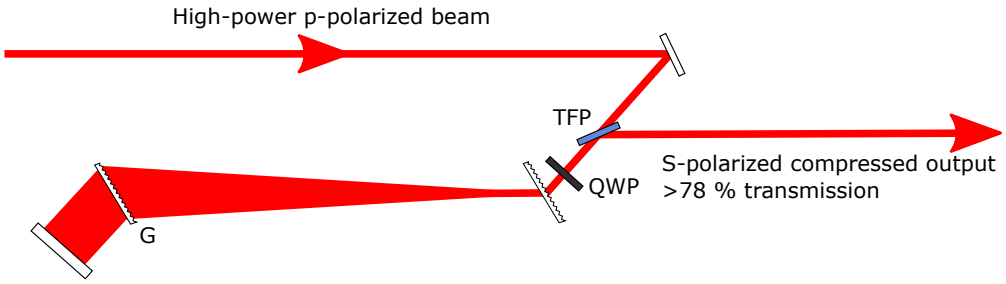

Figure 4.29: Layout of the compressor. TFP: thin film polarizer, QWP: quarter waveplate, G: grating.

grating pair with 1000 lines/mm density and a flat end-mirror, which is high-reflective at 1030 nm (Edmund Optics 38.1 x 25.4mm 1030nm 0-45°). Since the light passes through the $\lambda/4$ waveplate twice, the polarization axis of the high power p-polarized beam shifts from p-polarization to s-polarization at the output of the compressor. The transmission efficiency of the compressor has been measured to be over 78%. In order to reduce the thermal effects, the grating mounts are designed in a way that the 0th order diffracted light can pass through the mount. Both grating mounts are placed on a 5-axis stage in order to enable fine-tuning of the relevant angles for a optimum compression factor throughput and for minimizing beam distortions. The second grating of the compressor together with the flat end-mirror is placed on a linear stage for tuning the grating distance. This kind of compressor design only works with polarization insensitive gratings.

4.3.3 Characterization of output parameters

The compressed output power of the system reaches above 88 W. Output power characterization for the high-power pump diode as well as the output power before and after the compressor is shown in Fig. 4.30. The slope efficiency (launched pump power versus output power) of the power amplifier was measured to be roughly 50 %, however, after accounting for losses and unabsorbed pump light, the value rises to $>$ 65 %. Although the power at the output of the rod type fiber is above 120 W, there are some losses introduced by the beam expanding telescope, the high power Faraday isolator and the grating compressor setup. The output power of the rod type fiber used is roughly limited to 120 W [40], [133], mainly due to the transverse mode instabilities (TMI) [134], [135]. For characterization, a fraction of the high power output is sent for temporal pulse characterization using FROG, as well as to an M^2 meter (Spiricon M2-200s) for analyzing the spatial quality of the output beam. A water-cooled power meter head is used for average power measurements. Measured output spectrum and reconstructed temporal pulse are shown in Fig. 4.31.

FWHM spectral bandwidth is roughly 8.3 nm and the compressed pulse duration is

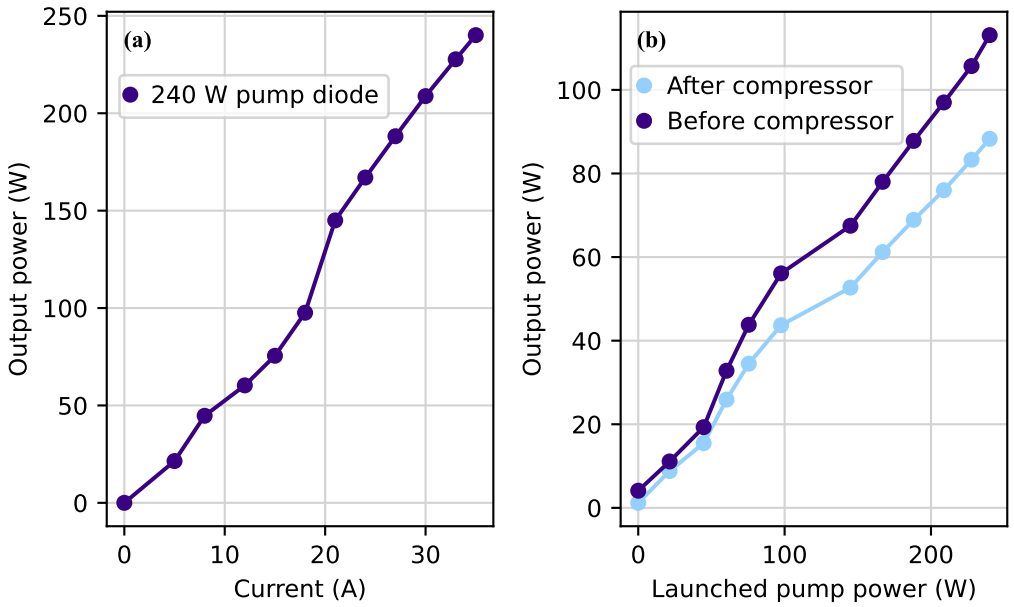

Figure 4.30: Output power characterization of 240 W high power pump diode and the power amplifier. Current versus output power of the high power pump diode is shown in (a) and output power of the power amplifier is shown in (b) before and after the compressor in dark and light blue, respectively.

around 203 fs, after carefully tuning the phase shaping parameters from the PAS. Comparison of the compressed pulse durations between the initial and the current dispersion management method is shown in Fig. 4.32. While switching between different dispersion management methods, the grating compressor at the high-power output is kept the same. Using the initial dispersion management, the system delivers longer pulses with pre- and post-pulses, indicating a poor TOD management. However, current dispersion management shows a cleaner pulse with no pre- or post-pulses and a shorter pulse duration. Measured and retrieved FROG traces are shown in Fig. 4.33. They show excellent agreement with below 0.5% FROG trace error. The corresponding transform-limited pulse duration is around 190 fs. The output beam profile for near and far field is shown in Fig. 4.34. The measured M^2 of the output beam is roughly 1.2, shown in Fig. 4.35.

A long-term power measurement is performed in order to analyze the long-term stability of the whole system. Relevant power levels are logged from various detectors, which are spread all over the laser system. Logged power levels show excellent long-term stability over 60 h as shown in Fig. 4.38. The high-power output after the compressor shows more than 88 W of average power with 0.29 % rms power fluctuations at 0.1 s integration time. Relevant temperature levels are also logged via temperature sensors, which are spread all over the system. Temperature levels are important, especially if the long-term stability

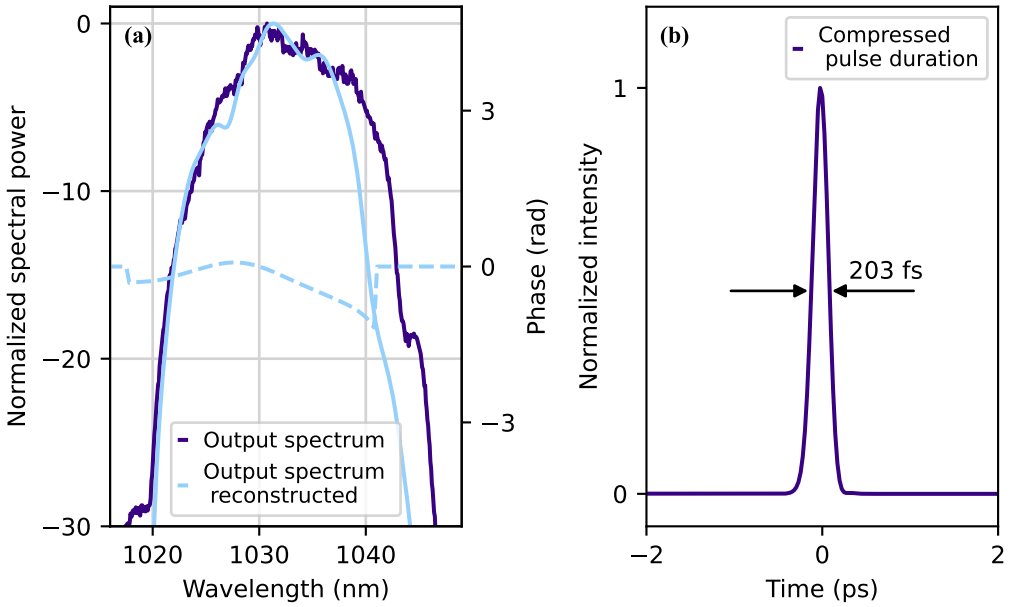

Figure 4.31: Output characterization of the compressor. Spectra comparison between measured and reconstructed high-power compressed output given in (a) with dark and light blue respectively. Dashed line depicts the spectral phase after compression. Compressed pulse duration is presented in (b).

of the system is considered. High temperature levels from the mounts of the optics can easily cause a misalignment of the beam path. Furthermore, keeping the high-power pump diode's temperature level constant is crucial in order to preserve the center wavelength. The temperature levels of the beam dumps are also important, since they can heat the whole amplifier box. Fig. 4.36 shows the temperature levels from different sensors placed on different components over 60 hours of operation. In Fig. 4.36 the temperature levels for both the high-power pump diodes from the front-end and the power amplifier, the seed coupling assembly, the rod-type fiber, the beam dumps and the power amplifier box are shown. All temperatures show an almost constant level without any significant change.

After 3-4 months of intermittent operation of the power amplifier, the output beam profile of the system started to degrade. The M^2 values deteriorated above certain average output levels. This effect is attributed to the TMI, caused by the thermal load on the rod type fiber module. TMI is an effect, which limits the average output power of the laser system. It was first seen in a high-power fiber laser system emitting a Gaussian beam, which abruptly changes its intensity distribution, when a certain average power level is exceeded [134]. These intensity changes are observed via a CCD camera, where the higher-order modes have appeared and changed the power distribution with the other transverse modes.

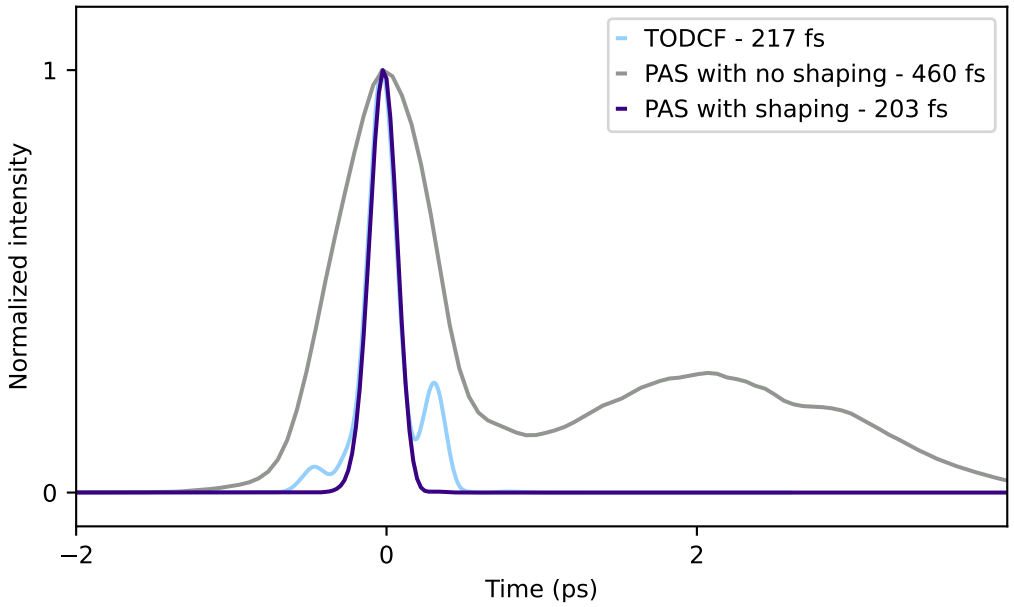

Figure 4.32: Pulse in temporal domain measured via FROG. Compressed pulse duration using first iteration of the dispersion engineering shown in light blue, the pulse duration using second iteration of the dispersion engineering without phase shaping shown in gray and with phase shaping shown in dark blue.

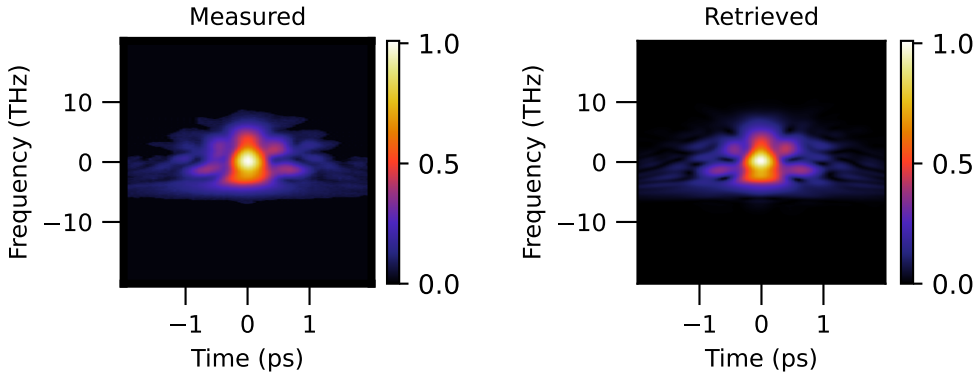

Figure 4.33: Measured and retrieved FROG traces after the compressor at full power operation.

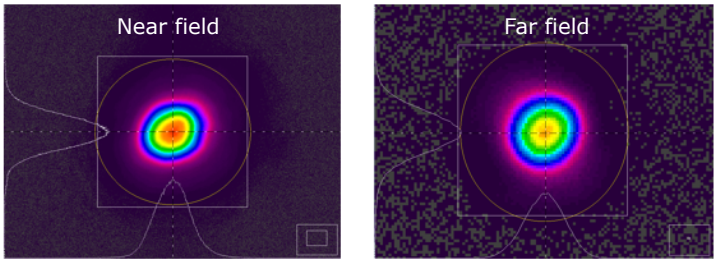

Figure 4.34: Image of the beam at near and far field at full power operation.

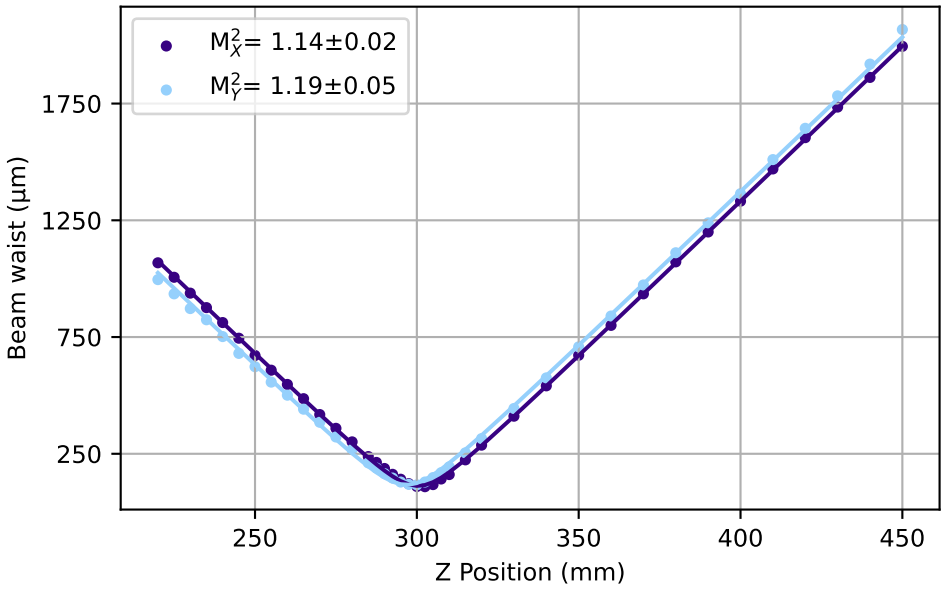

Figure 4.35: Fitted M^2 measurement of high-power compressed pulses showing M^2 values of 1.2.

The observed TMI issue is most probably triggered by imperfect seed coupling, which imprinted a thermally-induced index grating onto the rod fiber. The CPS at the output of the front-end was added to the system only after noticing the emerging temperature problem of the seed coupling stage, following a thermal scan of the system using a thermal camera. After adding the CPS, the temperature level of the seed coupling section follows the box temperature shown in Fig. 4.37. After this change, a temperature decrease of about 5°C is observed. The seed beam drift caused by the temperature increase at the seed coupling stage probably started the TMI and the effect has only gotten more prominent over time. However, it is still possible to reach an output power after the compressor of

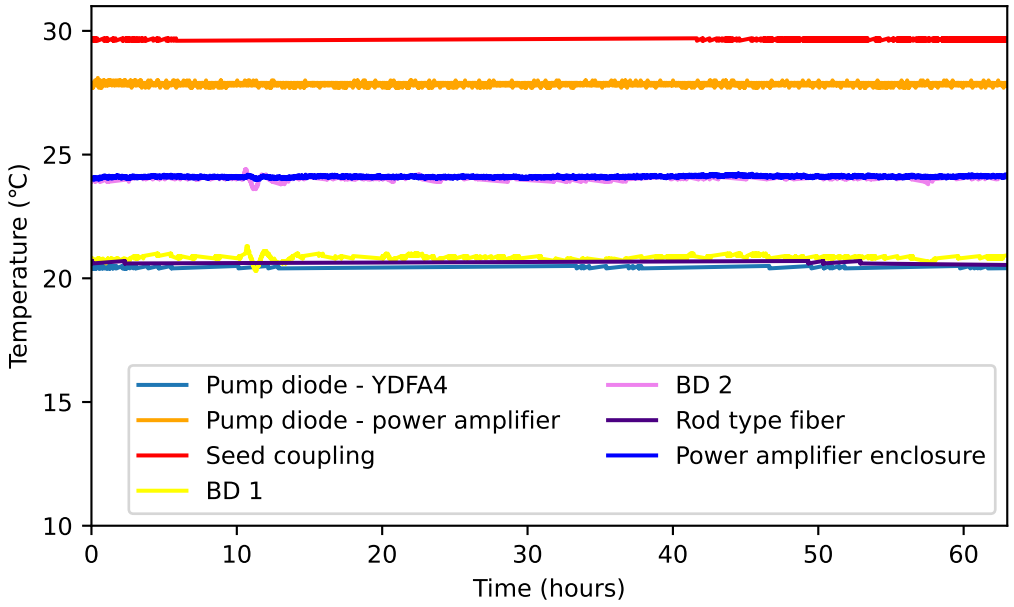

Figure 4.36: Temperature levels from various sections of the front-end and the power amplifier of the laser system for 60 hours.

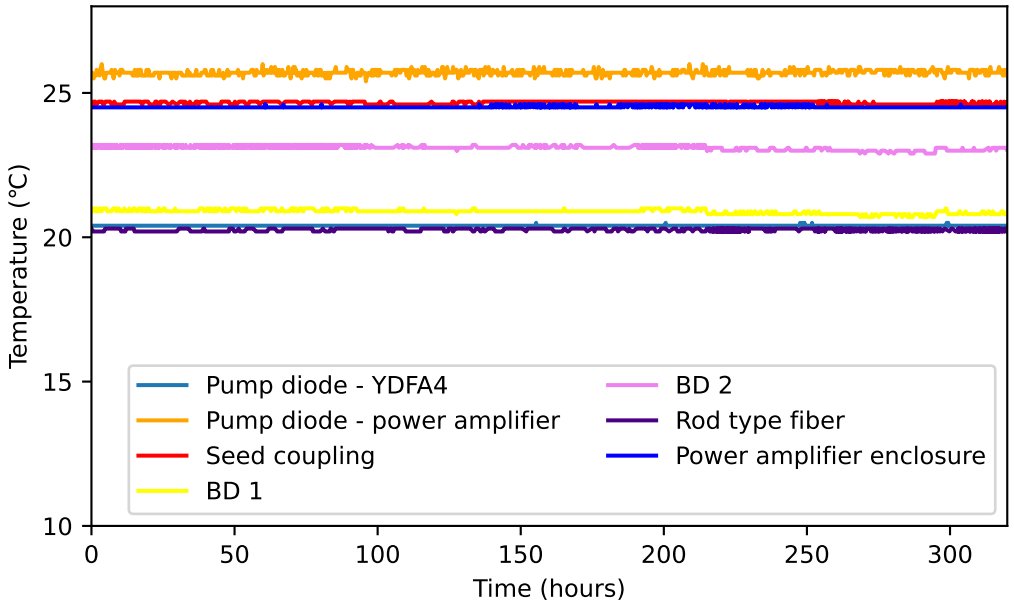

Figure 4.37: Temperature levels from various sections of the front-end and the power amplifier of the laser system for 320 hours.

72 W without a significant change of the beam quality. Long-term power measurements are performed for all most relevant sections of the laser system over 320 hours, which is shown in Fig. 4.39

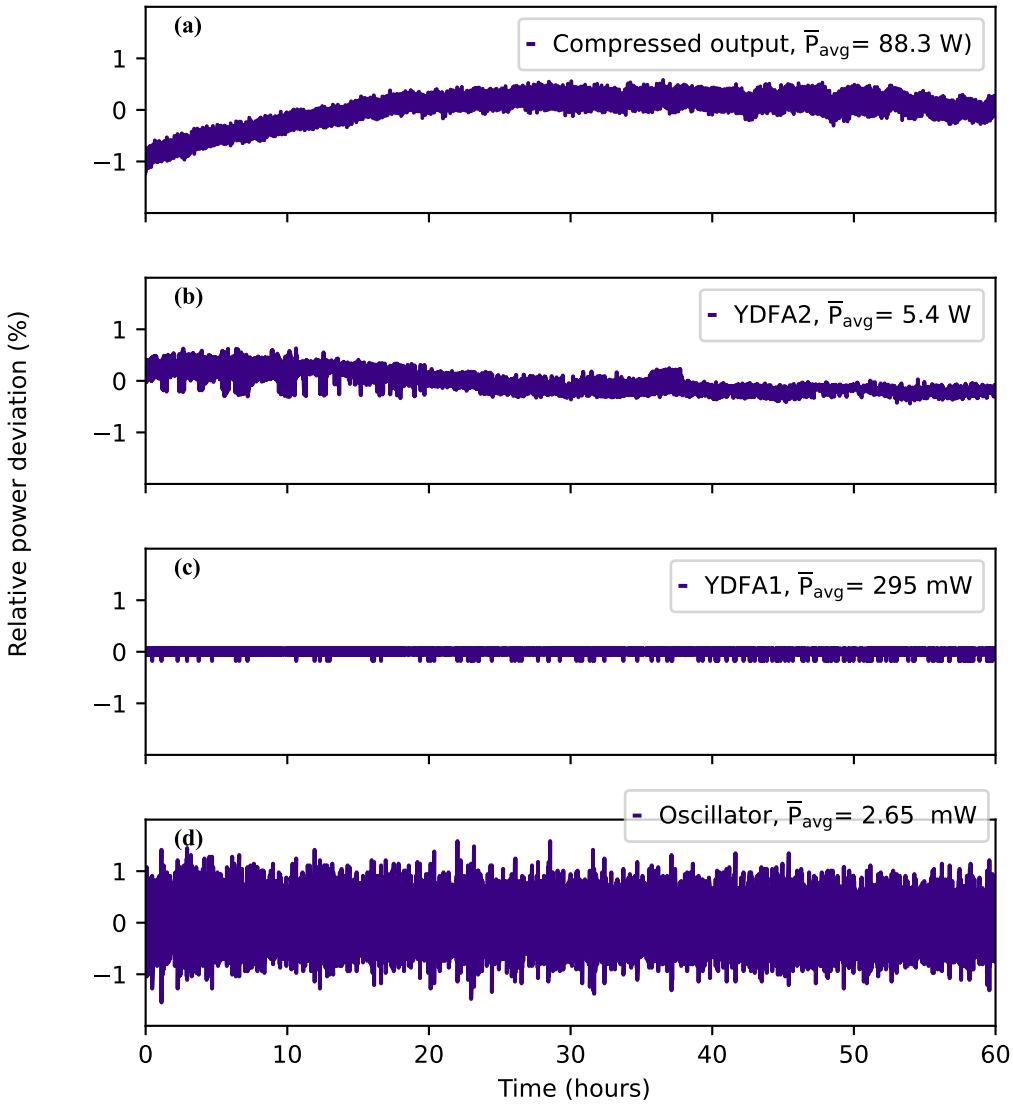

Figure 4.38: Long-term power measurement before the observation of TMI.

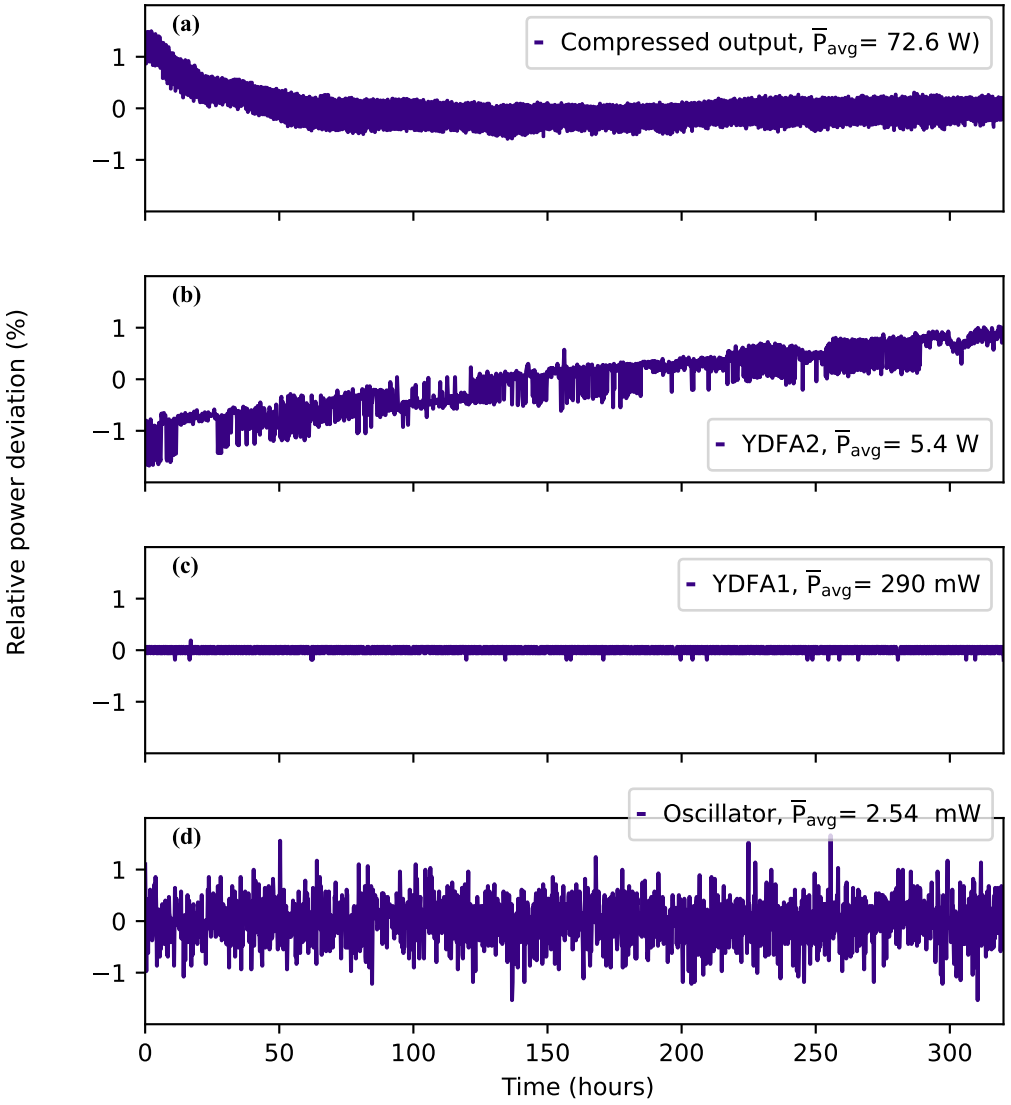

Figure 4.39: Long-term power measurements recorded after the observation of TMI issues.

4.4 Summary

A fully stabilized high-power and long-term stable frequency comb laser system has been developed. The pulse repetition rate of the laser system is fixed at about 65 MHz with an average power output after compression of 88 W and 72.5 W after the discussed TMI issue. The compressed pulse duration of the system is slightly above 200 fs with excellent temporal pulse shape and a peak power exceeding 5 MW. Moreover, as will be discussed in Chapter 6, the installation of a multi-pass cell at the laser output enables post-compression and wavelength-tuning. In addition, a long-term high power operation and a long-term frequency comb operation of the system are demonstrated. More than 320 hours of high power operation and 72 hours of frequency comb operation have been performed, which is one of the key requirements for spectroscopic applications with long acquisition times and also one of the key aspects of this thesis. The compactness of the system together with its fail-safe operation design makes it a suitable driver specifically for demanding spectroscopic applications. A picture of the laser system including the oscillator, front-end and the power amplifier is shown in Fig. 4.40

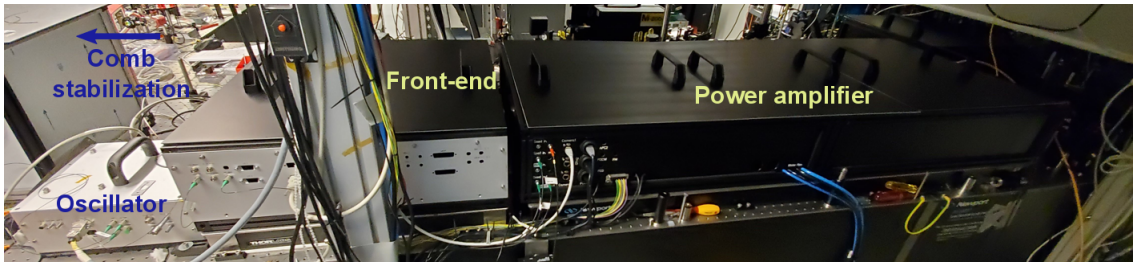

Figure 4.40: Picture of the laser system showing the front-end including the Yb:NALM oscillator, power amplifier and the compressor.

5 Long-Term Fail-Safe Operation of the Laser System

One of the key aspects of this dissertation work is the long-term and fail-safe operation of the whole laser system which is discussed in this chapter. For time-consuming experiments like the search for the Th-transistion, the system has to be able to provide a stable output for several hours, without deterioration of the output parameters. Furthermore, as the system provides high power output, technical measures have to be taken to detect possible failures and damage to the system. To ensure this stability and error-detection, a complex control system with several I/O devices and dedicated software and computers is implemented to the laser system. Controls of the laser system is divided into three main sections. First, remote controlling and monitoring relevant laser parameters and its integration is presented. It is followed by the description of the technical interlock of the laser system which ensures the fail-safe operation. Finally, implementation of the beam pointing stabilization is described and its long-term performance is analyzed.

5.1 Remote Control

The control system is designed in such a way that most of the relevant laser parameters are monitored and logged. There are several photodiodes, temperature sensors, humidity sensors, water leakage sensors, spectrometers and cameras integrated into the laser system. Most of the sensor outputs are fed into I/O units of a programmable logic controller unit (PLC) (Beckhoff CX9020). The different inputs are checked by a program running on the PLC CPU. It checks the output of the I/O modules and through the set limits, controls the laser system which will be discussed in section 5.2. Additional data like spectra and camera images are processed on a different computer. The second computer is running on Linux operating system and integrated to the accelerator control system which is developed in DESY and will be discussed in section 5.1.1.

Additionally, as mentioned before in section 4.1.3, an FPGA based digital PID loop filter (RedPitaya) is used to compensate slow drifts for the frequency comb stabilization. Implementing a digital PID loop filter enables remote and computer control for slow frequency comb stabilization and brings flexibility to the comb controls concerning stabilization and tuning. It runs on an open-source software package called PyRPL [136] which provides modules such as PID, oscilloscope, spectrum analyzer and IQ together

with a graphical user interface.

5.1.1 Integration to the accelerator control system

The whole laser system is integrated into the accelerator control system called DOOCS [137]. DOOCS stands for distributed object-oriented control system, which is widely used at DESY for accelerator control and diagnostics. It is first deployed at the FLASH facility in DESY in order to be used as the basic software framework for the accelerator controls, while the three-fold integrated network environment (TINE) is used for vacuum and magnet controls [138]. In this work, DOOCS is used for diagnostics and laser controls and TINE is for data logging. An in-house developed DOOCS panel used for the power

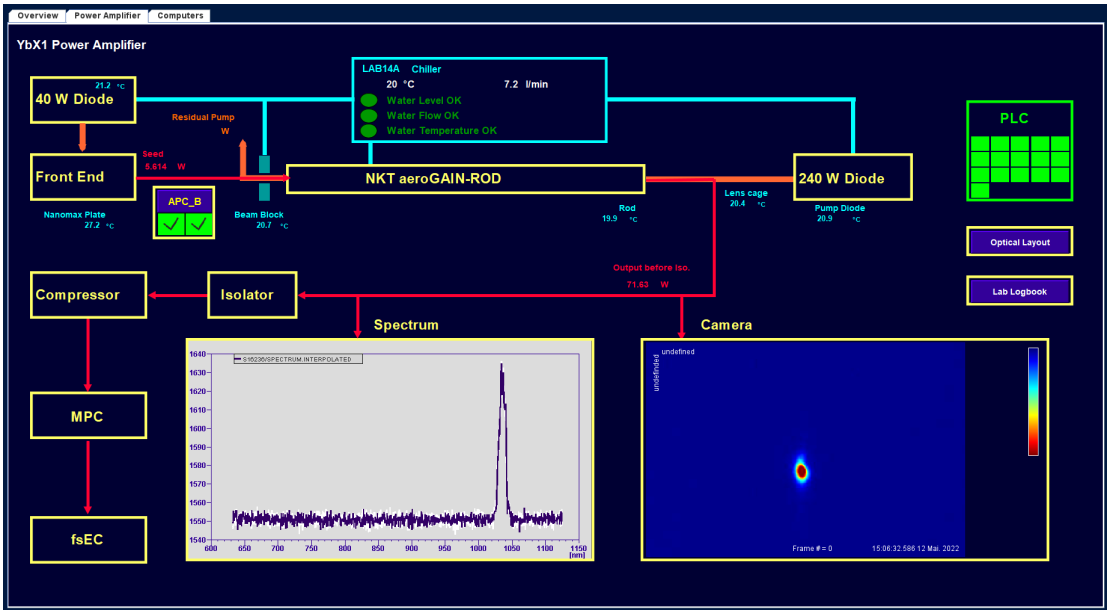

Figure 5.1: DOOCS panel of the laser system controls and diagnostics for the power amplifier.

amplifier section of the laser system is shown in Fig. 5.1. The panel shows the status of the PLC and its submodules, chiller status for the water cooling, several temperature values from various sections of the power amplifier, relevant power levels, status from the technical interlock specified for power amplifier (APC-B), an output spectrum and the beam profile. All the values shown in the panel such as temperatures and power levels are simultaneously logged via TINE. The DOOCS panel allows a high level of control over the whole laser system however, remote control of the laser diode drivers are not implemented yet. It is already implemented to several other laser systems within the Author's group at DESY, so it would be only a small effort to carry it out.

5.2 Technical interlock

Laser safety in a research and development laboratory is immensely important especially for high power, class 4 lasers. These type of lasers exceed the maximum permissible exposure irradiance restrictions for the eye and also for the skin. Concerning an interlock for such a laser system, one has to take into account different aspects, the prime aspect is safety. A safety interlock has to make sure that in case of an incident (e.g. emergency button is pushed, the lab door is opened forcefully) the laser system is shut down to prevent any harm to humans and to the facility. A second aspect is to prevent damage to the laser system itself (e.g. optical damage caused by the seedless operation of a laser amplifier) via a technical interlock. The technical interlock needs a delicate design, which needs to fulfill a time requirement concerning the response and a certain shut down order for the amplifiers. To eliminate all the concerns mentioned above and ensure the long-term and fail-safe operation of the laser system, a sophisticated technical interlock system is designed.

5.2.1 Interlock Design

The technical interlock has two main branches, a slow and fast interlock. These two branches are needed in order to address the various requirements and conciderations of the system.

The slow interlock acts on the slow signals supplied from the sensors of temperature, chiller, water leakage or the door interlock. As an example, in case of a water leakage or the door interlock failure, the slow interlock acts on the current drivers of all the pump diodes from all the amplifiers within the system and shuts them down in a specific order. This order moves from last amplifier towards the first one thus, the pump diode of the power amplifier shuts-down first, followed by the double-clad amplifier, followed by the single-clad amplifier and so on. Shutting down the system due to a temperature increase is more complicated. For different laser components, different temperature limits had to be defined. For all the pump diodes and the rod fiber, the temperature limits on the data sheets are inherited however, for beam dumps and the free-space sections of the power amplifier, the temperature levels are recorded while the laser system is working at full power. After thermalization of the system, the limits are set. All the sensors are controlled by the PLC through the I/O modules, together with an in-house developed python script, which checks all the sensors every second. In case of a failure, the PLC script triggers the safety relay (Phoenix contact PSR-PIP-24DC/MXF1/4X1/2X2/B) via the CPU module, which then cuts the power on the laser diode drivers. The door interlock for the lab is directly attached to the mentioned safety relay, which is independent of PLC signals. During design and implementation, it was measured that the time frame starting from the failure until the power cut is measured to be in the order of 20 ms. It is mostly limited by the response time of the safety relay. Additionally, the response time of the

high power laser diode driver (TDK LAMBDA GEN 30-50) is measured to be 400 µs. However, experimental and numerical studies show that, already a shorter time span is sufficient for an unseeded Yb:fiber amplifier to store a huge and potentially dangerous amount of energy. In only about 80 µs, already 30 dB of gain can be provided for ASE [139]. Thus, the slow interlock alone is too slow to put the amplifiers into a safe state That's why an additional interlock branch is introduced to ensure the long-term and fail-safe operation of the laser system.

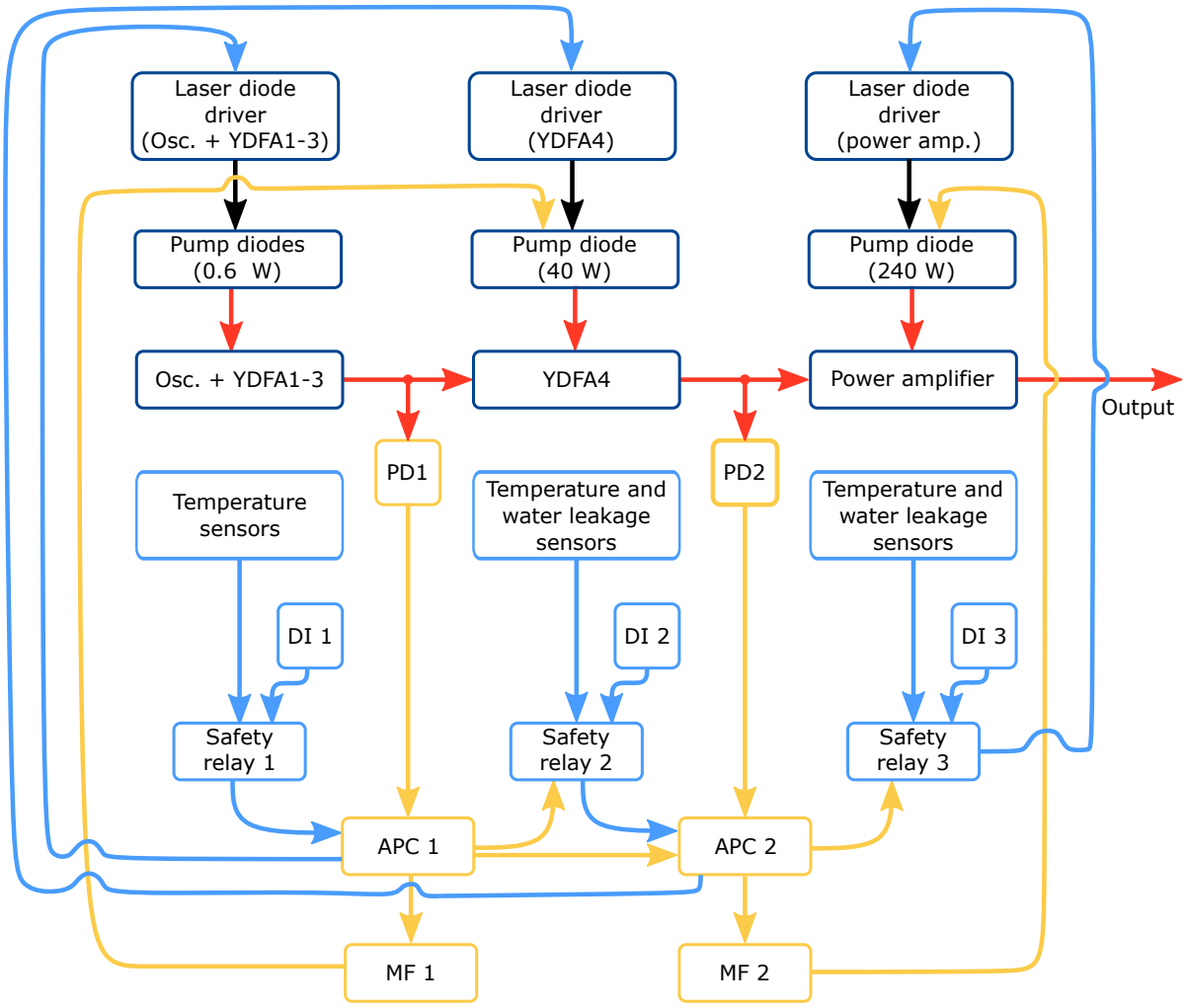

Figure 5.2: Logic diagram of the technical interlock. DI: door interlock, PD: fast photodetectors, APC: amplifier protection circuit, MF: MOSFET based crowbar circuit, black: electrical power cable to laser diodes, red: laser beam, blue lines: slow electronic signals, orange lines: fast electronic signals.

5.2.2 Fast shut-down circuit

In case of a possible seed malfunction in the amplifiers, a so-called crowbar circuit is designed and implemented by the author to the technical interlock as a second branch. The fundamental idea is, that in case of a sudden shutdown, this crowbar circuit drains the current which otherwise would flow over the laser diode (LD), until the power supply is shutdown by the slow interlock. Thus, the LD can be shutdown much faster than by just using the shutdown time of the current supply.

A printed circuit board (PCB) is made, consisting of a high current metal-oxide-semiconductor field-effect transistor (MOSFET), its microchip driver together with input as well as supply voltages and related resistors and capacitors. A specific power MOSFET (IXYS IXTN600N04T2) is chosen, which can bare high current levels due to the high power pump diodes used in the power amplifier and front-end. The assembled PCB is placed on a heat sink to reduce the potentially destructive effects of high temperature caused by high current levels. Two of these circuits are inserted in between the high power laser diode drivers and the high power laser diodes operating in power amplifier and front-end (YDFA4). The input signal for these circuits is supplied from FPGA based amplifier protection circuit (APC). There are two APCs (APC1 and APC2) in the technical interlock and they are interconnected (daisy-chained). The APCs receive the fast PD signals as input. The fast PDs are InGaAs based, fixed gain, high-sensitivity photodetectors with 600 MHz bandwidth. They are placed before (FPD610-FC-NIR) and after (FPD610-FS-NIR) YDFA4 (Fig. 5.2). The APC is designed to detect several possible faults: missing seed pulses (input from PDs) or too low or high seed pulses (exceeding a set limit) and too long pump pulses in case of pulsed pump operation. As soon as the APC detects a failure, it triggers the crowbar circuit which shortens the current on the high-power LDs. The time response of the amplifier protection circuit is on the order of 10 ns. The InGaAs based fixed gain high-sensitivity photodetectors (FPD610-FC-NIR and FPD610-FS-NIR) which are used for monitoring the seed behaviour has 600 MHz bandwidth. The time response of the crowbar circuit after getting the shut-down signal from the APC is shown in Fig. 5.3.

The time response of the crowbar circuit operates under 40 A is roughly 15 µs which is well-below the mentioned 80 µs time frame. The logic diagram of the technical interlock is shown in Fig. 5.2. The amplifiers need to be shut-off with a well-defined order in order to prevent seedless operation. The order is defined by introducing a delay to the signals. As an example, in case of a failure before YDFA4, the power amplifier will shut down first due to the 10 µs delay which is introduced to the APC1's output port. Moreover, the safety relays are also connected to the respective APCs. In case of a temperature out of limits, water leakage or door interlock failure, crowbar circuits (MFs in Fig. 5.2) are still triggered through APCs and shut down the amplifiers in the defined sequence. The technical interlock was tested thoroughly and a test protocol for regular check of the whole technical interlock was created.

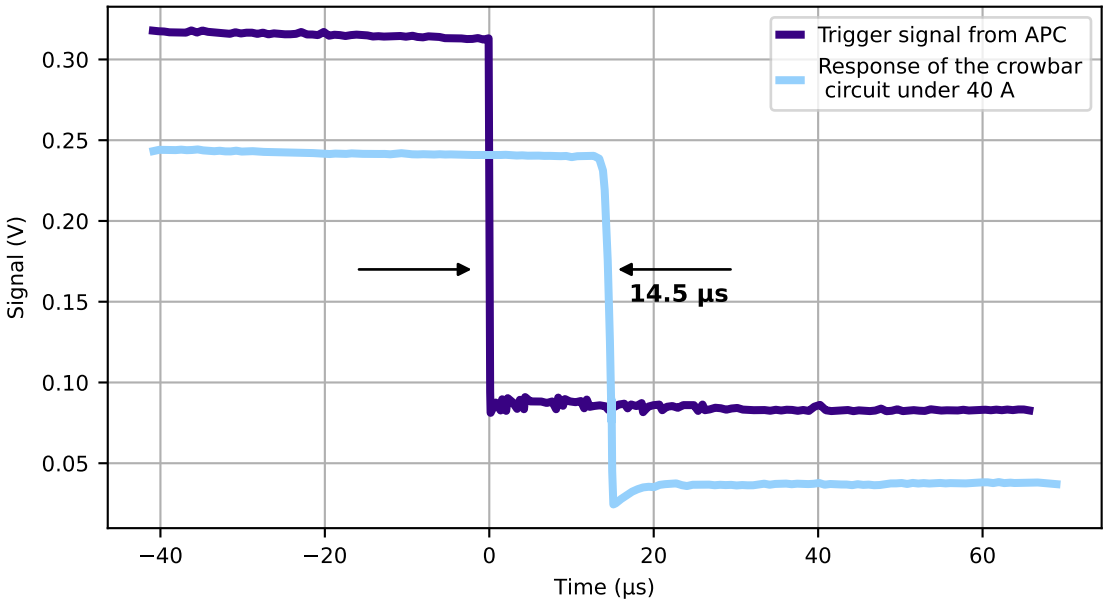

Figure 5.3: Time response of the crowbar circuit while intentionally emulating the seed failure on the power amplifier under 40 A

5.3 Beam pointing stabilization

The high-power output of the system is first sent to the MPC for either post-compression or center wavelength tuning and then is guided towards the enhancement cavity, where the HHG will be performed. The total optical path length is in the order of 20 m. Due to this long travel distance and beam stability requirements needed to operate the MPC and fsEC, a beam pointing stabilization system is introduced. It is placed immediately outside the power amplifier enclosure. The beam pointing stabilization setup is shown in Fig. 5.4. The system consists of two motorized mirror mounts (Newport 8816-6), a 50:50 beam splitter, a 200 mm focal length lens, two cameras where C1 (Basler acA2040-25gm) is used for near-field and C2 (Basler acA1300-30gm) is used for far-field positioning. The beam pointing stabilization system is also integrated into the DOOCS system and it is controlled by a python script. Long-term measurement from beam pointing fluctuations with active beam stabilization is shown in Fig. 5.5. After stabilization, fluctuations are suppressed significantly. For 320 h of measurement time, far-field beam pointing fluctuations are around ± 2% and near-field ± 0.6% for both x and y direction.

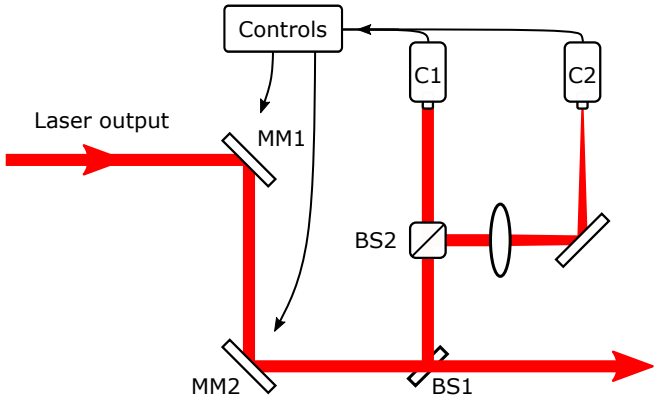

Figure 5.4: Schematic of the beam pointing stabilization setup. MM1,2: motorized mirrors, BS1: beam sampler, BS2: 50:50 beam splitter, C1,2: cameras, black: electrical cable, red: laser beam.

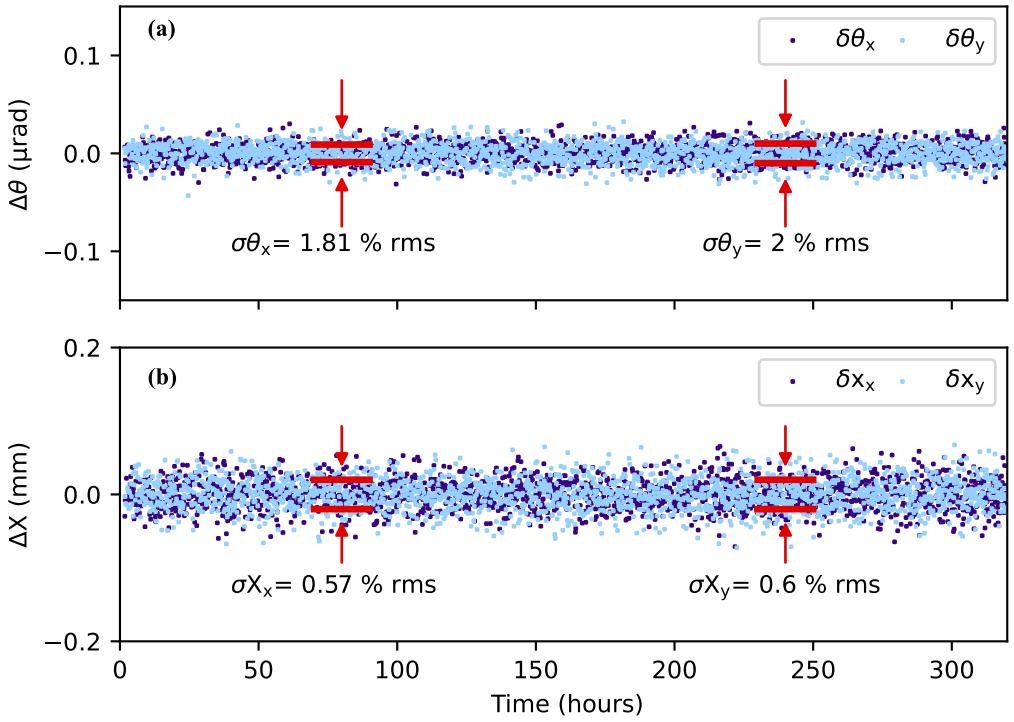

Figure 5.5: Long-term beam pointing fluctuations after beam pointing stabilization system is activated, (a) for far-field and (b) for near field.

5.4 Summary

As described above, the developed high-power frequency comb laser system was also equipped with a sophisticated control system. It is integrated into the accelerator control system DOOCS, and allows to monitor, control and log relevant laser parameters.

Additionally, a technical interlock is implemented, which grants a (certain) protection against damages to the laser system itself and also to its surrounding.

The technical interlock has two branches as slow which monitors the slow signals such as temperature, water leakage or door interlock while the fast branch monitors the seed power from different positions. In case of a failure, the technical interlock shuts down the whole laser system in a specific order, which is fast enough to protect the laser system and reduces the possible laser hazards to minimum. Finally, a beam pointing stabilization system is introduced at the output of the laser system, which suppresses the expected beam pointing fluctuations, caused by the nature of high-power lasers and also vibrations caused by the mechanical and thermal effects. Owing to this whole control and technical interlock system in place, long-term measurements like frequency comb stabilization or long-term high-power operation can be realized, without the need of permanent human observation.

6 Towards ultrahigh precision spectroscopy of ^{229}Th

6.1 Optically driven Thorium-229 nuclear transition

Ultrahigh precision spectroscopy of atomic transitions is one of the main topics of frequency comb spectroscopy for the study of fundamental interactions, precise determination of physical constants and the search for new physics [140], [141]. Similar measurements can also be performed in atomic nuclei [142]–[144]. The idea of nuclear optical clock has sparked many experimental and theoretical research. Such nuclear clocks have the potential to redefine the second, as the systematic frequency uncertainty is expected to better than the optical atomic clocks. In addition, being able to make high-precision

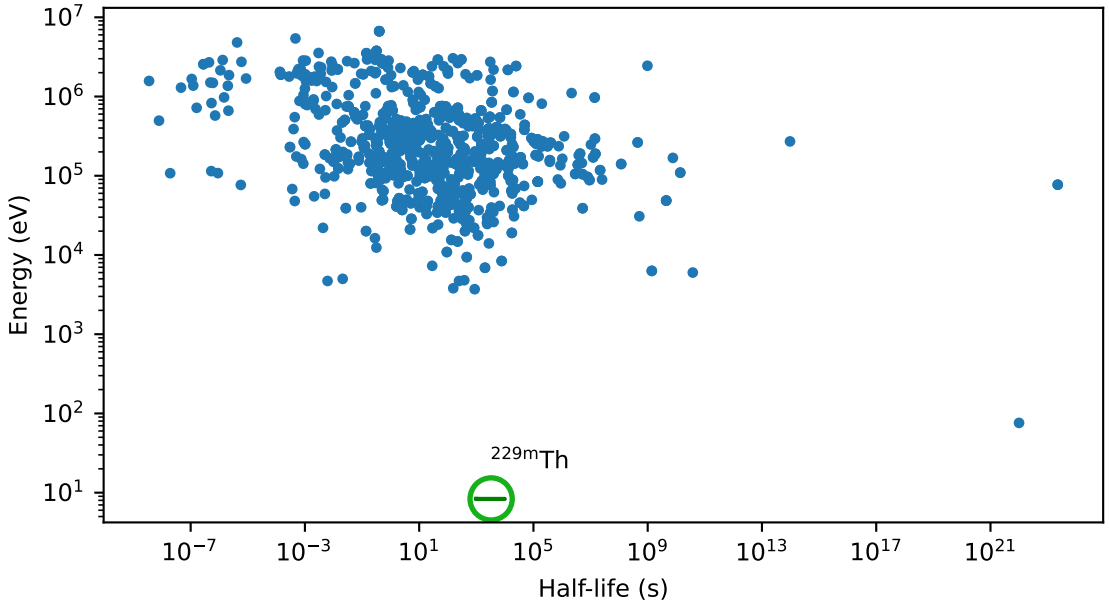

Figure 6.1: Excitation energy versus half-life distribution of most of the known nuclear isomeric states using references [30], [145]. ^{229}Th (indicated via a green circle) is the only known possible candidate for direct laser excitation.

measurements in nuclei will open up new possibilities for nuclear physics. So far there is

only one known nuclear excited state with an excitation energy comparable to the excitation energies measured in atoms, which is the low-energy isomeric state in ^{229}Th. Figure 6.1 shows the excitation energy distribution of isomeric nuclear isomeric states versus half-life. It is also the only known nuclear state that can prospectively be excited via direct laser excitation with current laser technology. Very recently, the radiative decay of this low-energy isomer in ^{229}Th is measured to be 8.338 ± 0.024 eV [30], which corresponds to 148.7 ± 0.43 nm. This new study decreases the uncertainty by approximately 7 times compared to earlier studies [146]–[148] while being in good agreement with them.

One of the most attractive routes towards direct laser excitation of 229Th is to employ a high-power Yb OFC and femtosecond cavity-enchanced 7^{th} harmonic combination hence, a VUV comb [149]. However, typical VUV comb spectral bandwidth doesn't cover the spectral range set by the current uncertainty of the ^{229}Th transition. In order to circumvent this problem, the comb's center wavelength needs to be tunable.

6.2 Multi-pass cell setup

In order to realize the spectral tuning of the high-power OFC's output, a new method based on the *serrodyne principle* is introduced [150]. This phenomenon has already been exploited in the radiofrequency, microwave and optical regions of the electromagnetic spectrum in order to shift the center frequencies. This principle combined with an MPC, can be used to tune the central frequency of ultrashort pulses over a THz frequency range [127].

As a basic principle, MPCs utilize a quasi-guiding structure that includes a Kerr medium in which a large nonlinear phase can be accumulated via multiple passes through the MPC [151], [152]. MPCs can be used for spectral broadening and other nonlinear processes [153]. Employed MPC for this laser is a very compact MPC (about 20 cm setup length), where glass windows are used as Kerr plates. It contains two concave mirrors with radii of curvature 100 mm with a separation of 187 mm and a dispersive coating of -200 fs^2. The dispersive medium used in MPC consists of five anti-reflection-coated solid fused silica windows. The window, which is placed at the focus has a thickness of 6.35 mm and the rest of the windows are 1 mm thick and placed 20 mm and 40 mm away from the focus symmetrically. The MPC accommodates 32 round trips.

6.2.1 Center frequency shifting of optical frequency comb output

According to the serrodyne principle, when a linear phase is applied on a signal in the time domain, the signal's frequency shifts [150]. This linear phase can be applied utilizing the Kerr-effect as it creates a temporal phase profile proportional to the temporal intensity profile of a pulse during propagation. Simply, a temporal saw-tooth pulse with center frequency ω_c, which experiences SPM, gets frequency shifted to $\omega = \omega_c + \Delta\omega$ where

$\Delta\omega = -\Phi_{nl} \frac{\mathrm{d}I(t)}{\mathrm{d}t}$ and Φ_{nl} is the accumulated nonlinear phase. However, for this method to work, the temporal saw-tooth pulse shape has to be maintained during propagation within the nonlinear medium, and this is typically not the case when linear dispersion and SPM are present. MPCs offers a solution to this obstacle since they can be built in a dispersion-balanced configuration, which supports large Φ_{nl} values. Fig. 6.2 shows the experimental data generated using the OFC, which is presented in Ch. 4. The triangular pulse is created using the integrated spatial light modulator (Fig. 4.21 PAS). The plot shows shifted center frequency to shorter wavelength, 999 nm (light blue) and to longer wavelength, 1062 nm (dark blue) in comparison with the input centered at a wavelength of about 1035 nm. At the MPC output, the frequency-shifted pulses are

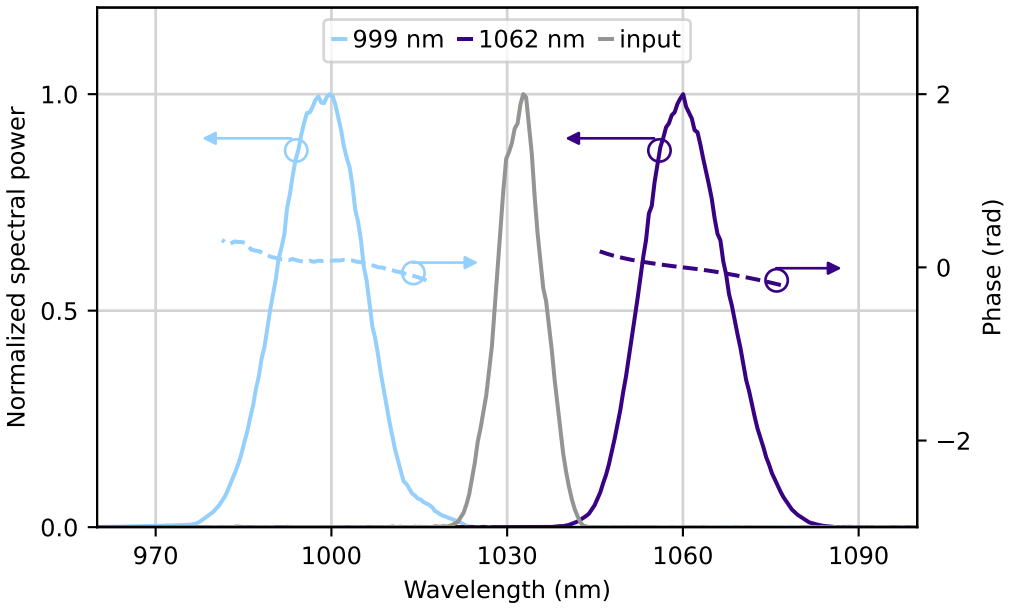

Figure 6.2: Measured spectra and corresponding retrieved phase after spectral shifting, filtering and compression. Solid lines depict the normalized intensity and dashed lines are retrieved phase

slightly negatively chirped. After spectral filtering, they are compressed to 92 fs and 106 fs after passing through 119 mm and 100 mm fused silica for 999 nm and 1062 nm, respectively. For the wavelength shifting experiments, pulses from the OFC with 76 W average power are coupled into the MPC. The throughput of the MPC is measured to be 62.2 W yielding an overall efficiency of 81%. After center wavelength shifting, spectral filtering and compression, efficiencies of 63% (39.2 W) and 66.7% (41.5 W) are reached for center wavelengths of at 999 nm and 1062 nm, respectively [127].

It is already known that, in the radiofrequency domain, serrodyne frequency translation is used for sideband suppression [154]. Additionally, it is possible to enhance the temporal

contrast of the laser pulses via filtering the SPM broadened spectra [155]. Consequently, temporal contrast improvements can also be expected for the demonstrated ultrafast Serrodyne method. Third-order autocorrelation measurements of the wavelength-shifted pulses are carried out, as explained in Ref. [127]. It is found that, the pulses at the output of the MPC have an improved temporal contrast, reaching at least an improvement factor of 200. Additionally, to verify that good coherence properties are maintained after the frequency shifting, a second interferometer (similar to the interferometer 1 in Fig. 4.5) is built where the shifted 1062 nm light characterized relative to the CW NPRO laser via heterodyne beat note generation. The phase noise properties of the generated beat note indicate excellent coherence, indicating a relative linewidth in the few-Hz range.

6.2.2 Post compression of the output pulses

While it is shown that MPC can be used for center frequency shifting of the high-power OFC output, MPCs are commonly mainly used for post-compression of ultrashort pulses [151]. It has been shown that even picosecond long pulses can be post-compressed into the few-cycle regime using two cascaded gas-filled MPCs [156]. Especially, for peak power hungry applications such as HHG [157] or XUV combs [158], MPCs are very attractive for nonlinear pulse compression. The earlier introduced MPC has also been used to demonstrate post-compression of the high-power OFC. Fig. 6.3 depicts the SPM broadened

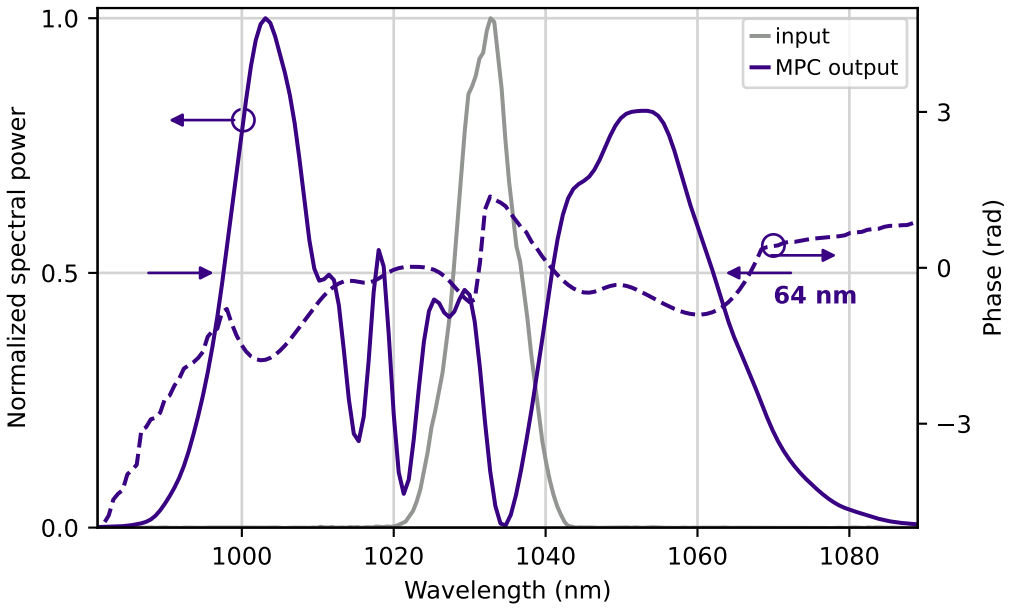

Figure 6.3: Measured SPM-broadened pulse spectrum from the MPC (dark blue) and retrieved phase (dashed) in comparison with the input spectrum (gray).

spectrum using the MPC in comparison to the input spectrum. The SPM-broadened

spectrum has roughly 64 nm bandwidth and the pulses are compressed to below 40 fs pulse duration, as demonstrated using FROG measurements.

6.3 Enhancement cavity for intra-cavity VUV and XUV generation

A fsEC is employed in order to enhance the power of the input femtosecond pulses and subsequently perform intra-cavity VUV or XUV generation. The fsEC is placed into a vacuum chamber, and consists of an input/output coupler and 7 highly reflective mirrors in order to fold the beam to match the pulse repetition rate of the OFC to the cavity. Two of the high-reflector mirrors have a radius of curvature of 150 and 200 mm with a separation of 180 mm, which produces a beam waist of approximately 24 µm at focus for both horizontal and vertical directions. The measured enhancement factor is around

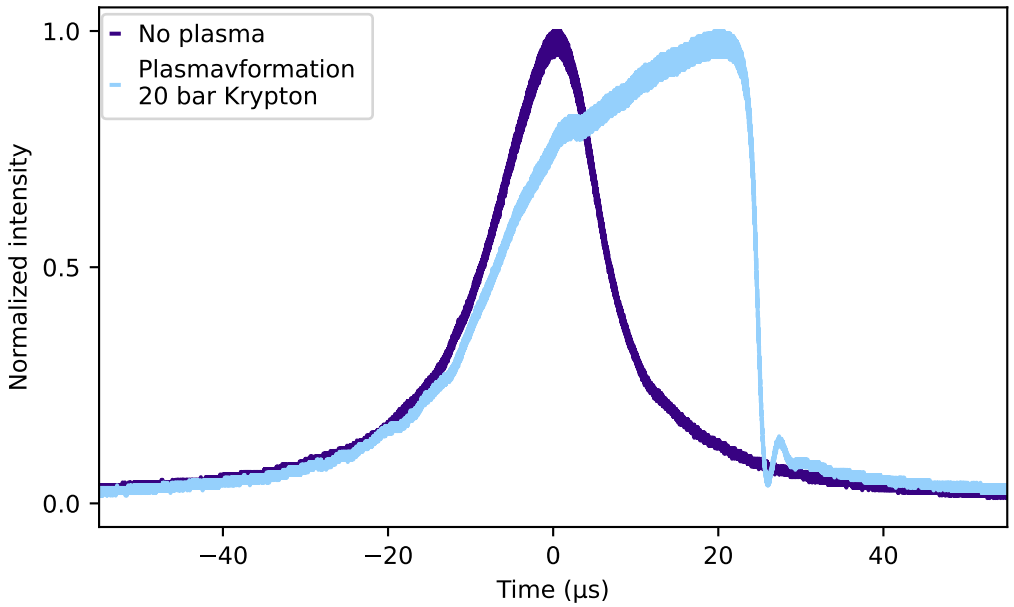

Figure 6.4: Intracavity laser power while sweeping over the cavity resonance without gas (dark blue) and with gas (light blue).

120, which corresponds to a intra-cavity peak power of 0.7 GW. To lock the fsEC to the OFC using the Pound-Drever-Hall (PDH) technique [159], one of the high-reflector cavity mirrors is glued onto a PZT for fast feedback and the one is placed on a PZT-actuated translation stage for slow feedback. Fig. 6.4 shows the first indication of plasma formation under 20 bar of Krypton, released via a high-pressure gas nozzle into the intra-cavity focus. An asymmetrically distorted cavity resonance is visible, indicating resonance

detuning via plasma generation [160].

6.4 ^{229}Th nuclear spectroscopy in an ion storage ring

At GSI (GSI Helmholtzzentrum für Schwerionenforschung GmbH) in the heavy ion storage ring ESR, an alternative approach to direct laser excitation and probing of ^{229}Th is pursued. Storage rings are typically used for storing ions up to high currents. By applying techniques like electron cooling, a high brilliance of the circulating ions beams is reached. The ESR [161] is the only storage ring world-wide that can provide high-brilliance ions from helium (Z = 2) to uranium (Z = 92) at ion velocities from below 10% to 90% of the speed of light. This thesis work includes contributions to a joint experimental effort at GSI aiming at ^{229}Th ion spectroscopy in the ESR storage ring as an alternative approach to direct laboratory-based laser spectroscopy.

The ^{229}Th spectroscopy approach targeted at the ESR is unique in several regards. In particular, it employs highly charged ^{229}Th such as one-electron ^{229}Th^{89+}. Under very strong magnetic fields, occurring within these highly charged ions, the unpaired s-electron mediates a mixing of the F = 2 levels of ground and isomeric states [162]. This nuclear hyperfine mixing (NHM) process leads to a small energy shift but more importantly it leads to a drastic decrease on the life-time of the isomeric state by 5 to 6 orders of magnitude, from few hours to few milliseconds. Consequently, the excitation probability with a laser and the detection of the fluorescence light are also enhanced accordingly. ^{229}Th is the nucleus with the lowest excitation energy of E = 8.28 eV (This value refers to the best measurements available mid-2022, before the more recent experiment discussed in Ref. [30]). However, due to the NHM in ^{229}Th^{89+}, for the ground-state laser excitation of two different nuclear hyperfine states, laser energies of 8.4 eV and 9.2 eV are required [163]. At the GSI, for this experiment, a dye laser with pulse energy up to 100 mJ at λ = 628 nm, which can be frequency doubled to λ = 314 nm, corresponding to an energy of 3.95 eV is used. The ions are stored in ESR moves at up to 72.5% of the speed-of-light. Probing those ions with a counter-propagating laser beam results in a Doppler shift. This Doppler shift corresponds to photon energies in the moving frame of reference of up to 10 eV. The photon energy is then scanned by tuning the center wavelength of the laser and by varying the ion energy in order to find the laser resonance of the hyperfine transition. Electron and ion energies are measured using a high-voltage divider in combination with Schottky spectroscopy. Schottky beam probes are used for precision diagnostics in order to registration of stored ions non-destructively with a big dynamic range [164]. Additionally, in order to detect the low-energy hyperfine photons ($\approx$ 0.7–0.8 eV), a fluorescence detection system with 3 independent detectors, which are optimized for the energy-range is utilized. Finally, a newly designed aluminum mirror system coated with MgF_2 and photo-multiplier-tube optimized between 110 nm-180 nm are employed allowing registration of short-wavelength photons down to 110 nm.

While a first experimental campaign at the ESR storage ring could be used to establish all experimental routines required for this challenging experiment, technical challenges with the seeding accelerator for the ESR storage ring limited the energy scan range. Therefore, only 15% of the planned energy search range is covered and the ^{229}Th laser resonance is not found yet. The established routines and achievements include testing of a new MgF_2 coated mirror setup, Doppler-boosted photon energies up to 9.3 eV are reached, new background-free low-beam intensity bunch-length measurements are performed, and via improvements of the data acquisition system, 10-fold increased sensitivity is obtained.

These achievements set the stage for follow-up campaigns which are envisioned in the near future.

7 Conclusion and outlook

In this dissertation, the development of a high-power fully-stabilized optical frequency comb with long-term stability and wavelength tunability is presented. The system and all sub-systems of the frequency comb described in detail in chapter 4 of this dissertation were designed, developed and assembled in-house by the author.

A NALM oscillator provides a low-noise, stable seed used for amplification and frequency comb stabilization. Amplification is done by two amplifier blocks, a front-end and a power amplifier. In the front-end, the seed pulses are initially chirped via a fiber stretcher in order to utilize CPA. It is followed by core-pumped and cladding-pumped fiber amplifiers. In-between the two fiber amplifiers, a phase and amplitude shaper is placed, which is used for dispersion compensation, as well as for a novel wavelength tuning technique. The output of the front-end is imaged into a rod type fiber for further amplification in a power amplifier. After final amplification, the pulses are compressed in a grating compressor. At the output the system delivers more than 72 W average power with 65 MHz pulse repetition rate and 203 fs compressed pulse duration at 1033 nm center wavelength.

In order to convert the system into a frequency comb, two degrees of freedom of the oscillator need to be stabilized: the carrier-envelope offset frequency (f_0) and the pulse repetition frequency. For f_0 detection, a self referenced f-to-$2f$ interferometer is employed, in order to detect f_0 beat notes. For pulse repetition frequency stabilization, a heterodyne beating method (f_{CW}), where a narrow linewidth laser is used as an optical reference, is used. In order to achieve a robust stabilization, more than 30 dB beat note SNR at 300 kHz RBW is targeted. In order to obtain the required signal strengths, two pre-chirp managed amplifiers are utilized for each stabilization channel. The generated beat note signals for f_0 and f_{CW} are then sent to a fast analog and a slow digital PID loop filter. Finally, the outputs of the PID loop filters are used to lock both signals via actuators.

The entire high-power frequency comb system is protected by a technical interlock, which enables fail-safe operation while providing an important basis for long-term stable operation. When triggered, it first cuts the current of the high-power amplifiers in a pre-defined order via a fast crowbar circuit, which protects the system from optical hazards. Then it turns off the entire system in a controlled manner. The interlock can react to numerous internal and external triggers, such as seed loss, water leakage or temperature fluctuations. Additionally, the system is integrated into the DESY control systems

DOOCS and TINE, which enable remote controlling, data monitoring, as well as data logging.

The system is tested for long-term operation and shows an excellent power stability over 320 h, where all the power fluctuations are within a ±1% range. Additionally, frequency comb stabilization for over 72 h is demonstrated and a phase-slip free frequency stabilization below ±16 mHz frequency fluctuations is shown. To the best of the author's knowledge, this is the first time that a fully-stabilized high-power frequency comb laser system reaches the mentioned stability levels.

The compressed output of the high-power long-term stable frequency comb is sent to an MPC for either center wavelength tuning, which is utilized in combination with phase shaping, or for post compression, depending on the experimental needs. The MPC is followed by a femtosecond enhancement cavity, which boosts the input power up to 120 times for intra-cavity HHG. First indication of plasma formation is shown by focusing the enhanced light into 20 bar of Krypton gas.

Although there is an indication of it, intra-cavity HHG has not been achieved yet with this system. Generating intra-cavity high-harmonics is one of the most promising future uses of the high-power frequency comb system developed within this dissertation. The system can be converted into a VUV or XUV frequency comb, depending on the application, which will open new possibilities for ultrahigh precision spectroscopy. In particular, the parameters of the developed system and subsequently its 7^{th} harmonic, fit for direct laser excitation of the ^{229}Th nuclear isomer very well [31], which is a major challenge yet to be addressed. Probing this nuclear transition is not only essential for nuclear clock development, but will prospectively open entirely new areas for nuclear physics and for frequency metrology in general [165], [166].

Bibliography

[1] M. Plank, "Zur theorie des gesetzes der energieverteilung im normalspektrum", *Verhandlungen der Deutschen Physikalischen Gesellschaft*, vol. 2, pp. 237–245, 1900.

[2] A. Einstein, "Concerning an heuristic point of view toward the emission and transformation of light", *American Journal of Physics*, vol. 33, no. 5, p. 367, 1965.

[3] A. Einstein, "Zur quantentheorie der strahlung", *First published in*, pp. 121–128, 1916.

[4] T. H. Maiman *et al.*, "Stimulated optical radiation in ruby", 1960.

[5] F. J. McClung and R. W. Hellwarth, "Giant optical pulsations from ruby", *Applied Optics*, vol. 1, no. 101, pp. 103–105, 1962.

[6] M DiDomenico Jr, "Small-signal analysis of internal (coupling-type) modulation of lasers", *Journal of Applied Physics*, vol. 35, no. 10, pp. 2870–2876, 1964.

[7] P. F. Moulton, "Spectroscopic and laser characteristics of ti: Al 2 o 3", *JOSA B*, vol. 3, no. 1, pp. 125–133, 1986.

[8] D. E. Spence, P. N. Kean, and W. Sibbett, "60-fsec pulse generation from a self-mode-locked ti: Sapphire laser", *Optics letters*, vol. 16, no. 1, pp. 42–44, 1991.

[9] D. Strickland and G. Mourou, "Compression of amplified chirped optical pulses", *Optics communications*, vol. 55, no. 6, pp. 447–449, 1985.

[10] E Snitzer, "Proposed fiber cavities for optical masers", *Journal of Applied Physics*, vol. 32, no. 1, pp. 36–39, 1961.

[11] C. J. Koester and E. Snitzer, "Amplification in a fiber laser", *Applied optics*, vol. 3, no. 10, pp. 1182–1186, 1964.

[12] K. C. Kao and G. A. Hockham, "Dielectric-fibre surface waveguides for optical frequencies", in *Proceedings of the Institution of Electrical Engineers*, IET, vol. 113, 1966, pp. 1151–1158.

[13] E Snitzer, H Po, F Hakimi, R Tumminelli, and B. McCollum, "Double clad, offset core nd fiber laser", in *Optical fiber sensors*, Optica Publishing Group, 1988, PD5.

[14] C. Jauregui, J. Limpert, and A. Tünnermann, "High-power fibre lasers", *Nature Photonics*, vol. 7, no. 11, pp. 861–867, Nov. 2013, ISSN: 1749-4885, 1749-4893. DOI: 10.1038/nphoton.2013.273.

[15] J. L. Hall, "Nobel lecture: Defining and measuring optical frequencies", *Reviews of modern physics*, vol. 78, no. 4, p. 1279, 2006.

[16] T. W. Hänsch, "Nobel lecture: Passion for precision", *Reviews of Modern Physics*, vol. 78, no. 4, p. 1297, 2006.

[17] J. Xia, F. Zhu, J. Bounds, *et al.*, "Spectroscopic trace gas detection in air-based gas mixtures: Some methods and applications for breath analysis and environmental monitoring", *Journal of Applied Physics*, vol. 131, no. 22, p. 220 901, 2022.

[18] J. Nürnberg, B. Willenberg, C. R. Phillips, and U. Keller, "Dual-comb ranging with frequency combs from single cavity free-running laser oscillators", *Optics Express*, vol. 29, no. 16, pp. 24 910–24 918, 2021.

[19] H. Timmers, A. Kowligy, A. Lind, *et al.*, "Molecular fingerprinting with bright, broadband infrared frequency combs", *Optica*, vol. 5, no. 6, pp. 727–732, 2018.

[20] L. Lundberg, M. Mazur, A. Mirani, *et al.*, "Phase-coherent lightwave communications with frequency combs", *Nature communications*, vol. 11, no. 1, p. 201, 2020.

[21] D. F. Phillips, A. G. Glenday, C.-H. Li, *et al.*, "Calibration of an astrophysical spectrograph below 1 m/s using a laser frequency comb", *Optics express*, vol. 20, no. 13, pp. 13 711–13 726, 2012.

[22] L. Essen and J. V. Parry, "An atomic standard of frequency and time interval: A caesium resonator", *Nature*, vol. 176, pp. 280–282, 1955.

[23] T. E. Parker, "Long-term comparison of caesium fountain primary frequency standards", *Metrologia*, vol. 47, no. 1, p. 1, 2009.

[24] N. Poli, C. Oates, P. Gill, and G. Tino, "Optical atomic clocks", *La rivista del Nuovo Cimento*, vol. 36, pp. 555–624, 2013.

[25] T. L. Nicholson, S. Campbell, R. Hutson, *et al.*, "Systematic evaluation of an atomic clock at 2× 10- 18 total uncertainty", *Nature communications*, vol. 6, no. 1, pp. 1–8, 2015.

[26] B. Bloom, T. Nicholson, J. Williams, *et al.*, "An optical lattice clock with accuracy and stability at the 10- 18 level", *Nature*, vol. 506, no. 7486, pp. 71–75, 2014.

[27] L. von der Wense, B. Seiferle, and P. G. Thirolf, "Towards a 229 th-based nuclear clock", *Measurement Techniques*, vol. 60, pp. 1178–1192, 2018.

[28] E Peik and C. Tamm, "Nuclear laser spectroscopy of the 3.5 ev transition in th-229", *Europhysics Letters*, vol. 61, no. 2, p. 181, 2003.

[29] E Peik, K Zimmermann, M Okhapkin, and C. Tamm, "Prospects for a nuclear optical frequency standard based on thorium-229", in *Frequency Standards and Metrology*, World Scientific, 2009, pp. 532–538.

[30] S. Kraemer, J. Moens, M. Athanasakis-Kaklamanakis, *et al.*, "Observation of the radiative decay of the 229th nuclear clock isomer", *Nature*, vol. 617, no. 7962, pp. 706–710, 2023.

[31] A. Schönberg, H. S. Salman, A. Tajalli, S. Kumar, I. Hartl, and C. M. Heyl, "Below-threshold harmonic generation in gas-jets for th-229 nuclear spectroscopy", *Optics Express*, vol. 31, no. 8, pp. 12 880–12 893, 2023.

[32] C. Gohle, T. Udem, M. Herrmann, *et al.*, "A frequency comb in the extreme ultraviolet", *Nature*, vol. 436, no. 7048, pp. 234–237, 2005.

[33] R. J. Jones, K. D. Moll, M. J. Thorpe, and J. Ye, "Phase-coherent frequency combs in the vacuum ultraviolet via high-harmonic generation inside a femtosecond enhancement cavity", *Physical Review Letters*, vol. 94, no. 19, p. 193 201, 2005.

[34] X. Li, M. A. R. Reber, C. Corder, Y. Chen, P. Zhao, and T. K. Allison, "High-power ultrafast yb:fiber laser frequency combs using commercially available components and basic fiber tools", *Review of Scientific Instruments*, vol. 87, no. 9, p. 093 114, Sep. 2016, Publisher: AIP Publishing. DOI: 10.1063/1.4962867.

[35] A. Cingöz, D. C. Yost, T. K. Allison, *et al.*, "Direct frequency comb spectroscopy in the extreme ultraviolet", *Nature*, vol. 482, no. 7383, pp. 68–71, Feb. 2012, Publisher: Springer Nature, ISSN: 1476-4687. DOI: 10.1038/nature10711.

[36] A. Ozawa and Y. Kobayashi, "Vuv frequency-comb spectroscopy of atomic xenon", *Physical Review A*, vol. 87, no. 2, p. 022 507, 2013.

[37] D. Luo, Y. Liu, C. Gu, *et al.*, "130 w, 180 fs ultrafast yb-doped fiber frequency comb based on chirped-pulse fiber amplification", *Optics Express*, vol. 28, no. 4, pp. 4817–4824, 2020.

[38] C. Zhang, P. Li, J. Jiang, *et al.*, "Tunable vuv frequency comb for 229m th nuclear spectroscopy", *Optics Letters*, vol. 47, no. 21, pp. 5591–5594, 2022.

[39] A. Ruehl, A. Marcinkevicius, M. E. Fermann, and I. Hartl, "80 w, 120 fs yb-fiber frequency comb", *Optics letters*, vol. 35, no. 18, pp. 3015–3017, 2010.

[40] X. Li, M. A. Reber, C. Corder, Y. Chen, P. Zhao, and T. K. Allison, "High-power ultrafast yb: Fiber laser frequency combs using commercially available components and basic fiber tools", *Review of Scientific Instruments*, vol. 87, no. 9, p. 093 114, 2016.

[41] T. Udem, R. Holzwarth, and T. W. Hänsch, "Optical frequency metrology", *Nature*, vol. 416, no. 6877, pp. 233–237, 2002.

[42] G. Paulus, F Grasbon, H Walther, *et al.*, "Absolute-phase phenomena in photoionization with few-cycle laser pulses", *Nature*, vol. 414, no. 6860, pp. 182–184, 2001.

[43] M. Drescher, M. Hentschel, R. Kienberger, *et al.*, "X-ray pulses approaching the attosecond frontier", *Science*, vol. 291, no. 5510, pp. 1923–1927, 2001.

[44] A. M. Weiner, *Ultrafast optics, a john wiley & sons inc*, 2009.

[45] T. Ando, A. Liu, N. Negishi, A. Iwasaki, and K. Yamanouchi, "Spin-orbit splitting of ar+, kr+, and kr 2+ determined by strong-field ultrahigh-resolution fourier-transform spectroscopy", *Physical Review A*, vol. 104, no. 3, p. 033 516, 2021.

[46] N. Nishizawa and K. Takahashi, "Time-domain near-infrared spectroscopy using a wavelength-tunable narrow-linewidth source by spectral compression of ultrashort soliton pulses", *Optics letters*, vol. 36, no. 19, pp. 3780–3782, 2011.

[47] G. Mourou, "Nobel lecture: Extreme light physics and application", *Reviews of Modern Physics*, vol. 91, no. 3, p. 030 501, 2019.

[48] T. Fortier and E. Baumann, "20 years of developments in optical frequency comb technology and applications", *Communications Physics*, vol. 2, no. 1, pp. 1–16, 2019, Publisher: Nature Publishing Group.

[49] S. A. Diddams, T. Udem, J. C. Bergquist, *et al.*, "An optical clock based on a single trapped ^{199} hg $^{+}$ ion", *Science*, vol. 293, no. 5531, pp. 825–828, Aug. 3, 2001, ISSN: 0036-8075, 1095-9203. DOI: 10.1126/science.1061171.

[50] J. Xia, F. Zhu, J. Bounds, *et al.*, "Spectroscopic trace gas detection in air-based gas mixtures: Some methods and applications for breath analysis and environmental monitoring", *Journal of Applied Physics*, vol. 131, no. 22, p. 220 901, Jun. 14, 2022, ISSN: 0021-8979, 1089-7550. DOI: 10.1063/5.0091263.

[51] D. F. Phillips, A. G. Glenday, C.-H. Li, *et al.*, "Calibration of an astrophysical spectrograph below 1 m/s using a laser frequency comb", *Optics Express*, vol. 20, no. 13, p. 13 711, Jun. 18, 2012, ISSN: 1094-4087. DOI: 10.1364/OE.20.013711.

[52] J. Nürnberg, B. Willenberg, C. R. Phillips, and U. Keller, "Dual-comb ranging with frequency combs from single cavity free-running laser oscillators", *Optics Express*, vol. 29, no. 16, p. 24 910, Aug. 2, 2021, ISSN: 1094-4087. DOI: 10.1364/OE.428051.

[53] L. Lundberg, M. Mazur, A. Mirani, *et al.*, "Phase-coherent lightwave communications with frequency combs", *Nature Communications*, vol. 11, no. 1, p. 201, Dec. 2020, ISSN: 2041-1723. DOI: 10.1038/s41467-019-14010-7.

[54] H. Timmers, A. Kowligy, A. Lind, *et al.*, "Molecular fingerprinting with bright, broadband infrared frequency combs", *Optica*, vol. 5, no. 6, p. 727, Jun. 20, 2018, ISSN: 2334-2536. DOI: 10.1364/OPTICA.5.000727.

[55] T. Udem, J Reichert, R Holzwarth, and T. Hänsch, "Absolute optical frequency measurement of the cesium d 1 line with a mode-locked laser", *Physical review letters*, vol. 82, no. 18, p. 3568, 1999, Publisher: APS.

[56] L. Xu, C. Spielmann, A Poppe, T Brabec, F. Krausz, and T. Hänsch, "Route to phase control of ultrashort light pulses", *Optics letters*, vol. 21, no. 24, pp. 2008–2010, 1996.

[57] H. R. Telle, G. Steinmeyer, A. E. Dunlop, J. Stenger, D. H. Sutter, and U. Keller, "Carrier-envelope offset phase control: A novel concept for absolute optical frequency measurement and ultrashort pulse generation", *Applied Physics B*, vol. 69, p. 327, 1999.

[58] J. M. Dudley, G. Genty, and S. Coen, "Supercontinuum generation in photonic crystal fiber", *Reviews of modern physics*, vol. 78, no. 4, p. 1135, 2006.

[59] U Keller, "Ultrafast solid-state laser oscillators: A success story for the last 20 years with no end in sight", *Applied Physics B*, vol. 100, pp. 15–28, 2010.

[60] M. Hoffmann, S. Schilt, and T. Südmeyer, "Ceo stabilization of a femtosecond laser using a sesam as fast opto-optical modulator", *Optics Express*, vol. 21, no. 24, pp. 30 054–30 064, 2013.

[61] R. Paschotta, "Noise of mode-locked lasers (part i): Numerical model", *Applied Physics B*, vol. 79, pp. 153–162, 2004.

[62] C. H. Henry and R. F. Kazarinov, "Quantum noise in photonics", *Reviews of Modern Physics*, vol. 68, no. 3, p. 801, 1996.

[63] R. Paschotta, "Noise of mode-locked lasers (part ii): Timing jitter and other fluctuations", *Applied Physics B*, vol. 79, pp. 163–173, 2004.

[64] R Paschotta, A Schlatter, S. Zeller, H. Telle, and U Keller, "Optical phase noise and carrier-envelope offset noise of mode-locked lasers", *Applied Physics B*, vol. 82, pp. 265–273, 2006.

[65] A. Sennaroglu, *Solid-state lasers and applications*. CRC press, 2017.

[66] I. Pupeza, C. Zhang, M. Högner, and J. Ye, "Extreme-ultraviolet frequency combs for precision metrology and attosecond science", *Nature Photonics*, vol. 15, no. 3, pp. 175–186, 2021.

[67] T. Allison, T. Wright, A. Stooke, *et al.*, "Femtosecond spectroscopy with vacuum ultraviolet pulse pairs", *Optics letters*, vol. 35, no. 21, pp. 3664–3666, 2010.

[68] A Ravasio, D Gauthier, F. Maia, *et al.*, "Single-shot diffractive imaging with a table-top femtosecond soft x-ray laser-harmonics source", *Physical review letters*, vol. 103, no. 2, p. 028 104, 2009.

[69] Z.-H. Loh and S. R. Leone, "Ultrafast strong-field dissociative ionization dynamics of ch 2 br 2 probed by femtosecond soft x-ray transient absorption spectroscopy", *The Journal of chemical physics*, vol. 128, no. 20, p. 204 302, 2008.

[70] F. Krausz and M. Ivanov, "Attosecond physics", *Reviews of modern physics*, vol. 81, no. 1, p. 163, 2009.

[71] C. Chen, G. Wang, X. Wang, and Z. Xu, "Deep-uv nonlinear optical crystal kbe 2 bo 3 f 2—discovery, growth, optical properties and applications", *Applied Physics B*, vol. 97, pp. 9–25, 2009.

[72] J. C. Travers, T. F. Grigorova, C. Brahms, and F. Belli, "High-energy pulse self-compression and ultraviolet generation through soliton dynamics in hollow capillary fibres", *Nature Photonics*, vol. 13, no. 8, pp. 547–554, 2019.

[73] D. C. Yost, T. R. Schibli, J. Ye, *et al.*, "Vacuum-ultraviolet frequency combs from below-threshold harmonics", *Nature Physics*, vol. 5, no. 11, pp. 815–820, 2009.

[74] C. Benko, T. K. Allison, A. Cingöz, *et al.*, "Extreme ultraviolet radiation with coherence time greater than 1 s", *Nature Photonics*, vol. 8, no. 7, pp. 530–536, 2014.

[75] J. Nauta, A. Borodin, H. B. Ledwa, *et al.*, "Towards precision measurements on highly charged ions using a high harmonic generation frequency comb", *Nuclear Instruments and Methods in Physics Research Section B: Beam Interactions with Materials and Atoms*, vol. 408, pp. 285–288, 2017.

[76] J Mark, L. Liu, K. Hall, H. A. Haus, and E. P. Ippen, "Femtosecond pulse generation in a laser with a nonlinear external resonator", *Optics letters*, vol. 14, no. 1, pp. 48–50, 1989.

[77] W. Nagourney, *Quantum electronics for atomic physics and telecommunication*. OUP Oxford, 2014.

[78] A. P. Goutzoulis, D. R. Pape, and S. V. Kulakov, Eds., *Design and fabrication of acousto-optic devices* (Optical engineering v. 41). New York: M. Dekker, 1994, ISBN: 978-0-8247-8930-5.

[79] U. Keller, K. J. Weingarten, F. X. Kartner, *et al.*, "Semiconductor saturable absorber mirrors (sesam's) for femtosecond to nanosecond pulse generation in solid-state lasers", *IEEE Journal of selected topics in QUANTUM ELECTRONICS*, vol. 2, no. 3, pp. 435–453, 1996.

[80] W. Stepien and J. R. Marciante, "Review of ultrafast fiber oscillators based on mamyshev and dissipative soliton resonance mechanisms", *JOSA B*, vol. 39, no. 3, pp. 626–633, 2022.

[81] M. E. Fermann and I. Hartl, "Ultrafast fibre lasers", *Nature photonics*, vol. 7, no. 11, p. 868, 2013, Publisher: Nature Publishing Group, ISSN: 1749-4893. DOI: 10.1038/nphoton.2013.280.

[82] V. Matsas, D. Richardson, T. Newson, and D. Payne, "Characterization of a self-starting, passively mode-locked fiber ring laser that exploits nonlinear polarization evolution", *Optics letters*, vol. 18, no. 5, pp. 358–360, 1993.

[83] W. Hänsel, H. Hoogland, M. Giunta, *et al.*, "All polarization-maintaining fiber laser architecture for robust femtosecond pulse generation", *Exploring the World with the Laser: Dedicated to Theodor Hänsch on his 75th birthday*, pp. 331–340, 2018.

[84] M Guina, N Xiang, and O. Okhotnikov, "Stretched-pulse fiber lasers based on semiconductor saturable absorbers", *Applied Physics B*, vol. 74, s193–s200, 2002.

[85] M. E. Fermann, F Haberl, M. Hofer, and H Hochreiter, "Nonlinear amplifying loop mirror", *Optics Letters*, vol. 15, no. 13, pp. 752–754, 1990.

[86] N Kuse, J Jiang, C.-C. Lee, T. Schibli, and M. Fermann, "All polarization-maintaining er fiber-based optical frequency combs with nonlinear amplifying loop mirror", *Optics express*, vol. 24, no. 3, pp. 3095–3102, 2016.

[87] T. Jiang, Y. Cui, P. Lu, C. Li, A. Wang, and Z. Zhang, "All pm fiber laser mode locked with a compact phase biased amplifier loop mirror", *IEEE Photonics Technology Letters*, vol. 28, no. 16, pp. 1786–1789, 2016.

[88] A. S. Mayer, W. Grosinger, J. Fellinger, *et al.*, "Flexible all-pm nalm yb: Fiber laser design for frequency comb applications: Operation regimes and their noise properties", *Optics express*, vol. 28, no. 13, pp. 18 946–18 968, 2020.

[89] Y. Ma, S. H. Salman, C. Li, *et al.*, "Compact, all-pm fiber integrated and alignment-free ultrafast yb: Fiber nalm laser with sub-femtosecond timing jitter", *Journal of Lightwave Technology*, vol. 39, no. 13, pp. 4431–4438, 2021.

[90] W Haensel, R Holzwarth, R Doubek, and M Mei, "Laser with non-linear optical loop mirror", *EP2637265 A1*, 2013.

[91] F. Ilday, F. Wise, and T Sosnowski, "High-energy femtosecond stretched-pulse fiber laser with a nonlinear optical loop mirror", *Optics letters*, vol. 27, no. 17, pp. 1531–1533, 2002.

[92] L. Nugent-Glandorf, T. A. Johnson, Y. Kobayashi, and S. A. Diddams, "Impact of dispersion on amplitude and frequency noise in a yb-fiber laser comb", *Optics letters*, vol. 36, no. 9, pp. 1578–1580, 2011.

[93] G. Agrawal, "Nonlinear fiber optics, academic, san diego", 2001.

[94] R. W. Boyd, *Nonlinear optics*. Academic press, 2020.

[95] F. Mitschke and F. Mitschke, *Fiber optics*. Springer, 2016.

[96] E. Treacy, "Compression of picosecond light pulses", *Physics Letters A*, vol. 28, no. 1, pp. 34–35, 1968.

[97] R. Fork, O. Martinez, and J. Gordon, "Negative dispersion using pairs of prisms", *Optics letters*, vol. 9, no. 5, pp. 150–152, 1984.

[98] A. Baltuška, Z. Wei, M. S. Pshenichnikov, and D. A. Wiersma, "Optical pulse compression to 5 fs at a 1-mhz repetition rate", *Optics letters*, vol. 22, no. 2, pp. 102–104, 1997.

[99] J. Dugan, A. Price, M Ramadan, *et al.*, "All-optical, fiber-based 1550 nm dispersion compensation in a 10 gbit/s, 150 km transmission experiment over 1310 nm optimized fiber", in *Optical Fiber Communication Conference*, Optical Society of America, 1992, PD14.

[100] D. Pastor, J. Capmany, D. Ortega, V. Tatay, and J. Martí, "Design of apodized linearly chirped fiber gratings for dispersion compensation", *Journal of Lightwave Technology*, vol. 14, no. 11, pp. 2581–2588, 1996.

[101] A. M. Weiner, D. E. Leaird, J. Patel, and J. R. Wullert, "Programmable shaping of femtosecond optical pulses by use of 128-element liquid crystal phase modulator", *IEEE journal of quantum electronics*, vol. 28, no. 4, pp. 908–920, 1992.

[102] M. N. Zervas and C. A. Codemard, "High power fiber lasers: A review", *IEEE Journal of selected topics in Quantum Electronics*, vol. 20, no. 5, pp. 219–241, 2014.

[103] S. Wielandy, "Implications of higher-order mode content in large mode area fibers with good beam quality", *Optics Express*, vol. 15, no. 23, pp. 15 402–15 409, 2007.

[104] S. A. Cerqueira, "Recent progress and novel applications of photonic crystal fibers", *Reports on progress in physics*, vol. 73, no. 2, p. 024 401, 2010.

[105] J Limpert, N Deguil-Robin, I Manek-Hönninger, *et al.*, "High-power rod-type photonic crystal fiber laser", *Optics Express*, vol. 13, no. 4, pp. 1055–1058, 2005.

[106] M. Müller, C. Aleshire, A. Klenke, *et al.*, "10.4 kw coherently combined ultrafast fiber laser", *Optics letters*, vol. 45, no. 11, pp. 3083–3086, 2020.

[107] Y. Ma, S. H. Salman, C. Li, *et al.*, "Compact, all-PM fiber integrated and alignment-free ultrafast yb:fiber NALM laser with sub-femtosecond timing jitter", Jan. 8, 2021. arXiv: `2101.02920v1`.

[108] L. Dong, B. K. Thomas, and L. Fu, "Highly nonlinear silica suspended core fibers", *Optics Express*, vol. 16, no. 21, pp. 16 423–16 430, 2008.

[109] I Hartl, G Imeshev, M. Fermann, C Langrock, and M. Fejer, "Integrated self-referenced frequency-comb laser based on a combination of fiber and waveguide technology", *Optics express*, vol. 13, no. 17, pp. 6490–6496, 2005.

[110] A. Tourigny-Plante, V. Michaud-Belleau, N. Bourbeau Hébert, H. Bergeron, J. Genest, and J.-D. Deschênes, "An open and flexible digital phase-locked loop for optical metrology", *Review of Scientific Instruments*, vol. 89, no. 9, p. 093 103, 2018.

[111] M. J. Connelly, J. H. Galeti, and C. Kitano, "Piezoelectric mirror shifter transfer function measurement, modelling, and analysis using feedback based synthetic-heterodyne michelson interferometry", *OSA Continuum*, vol. 3, no. 12, pp. 3424–3432, 2020.

[112] T. C. Briles, D. C. Yost, A. Cingöz, J. Ye, and T. R. Schibli, "Simple piezoelectric-actuated mirror with 180 khz servo bandwidth", *Optics express*, vol. 18, no. 10, pp. 9739–9746, 2010.

[113] Y. Nakajima, H. Inaba, K. Hosaka, *et al.*, "A multi-branch, fiber-based frequency comb with millihertz-level relative linewidths using an intra-cavity electro-optic modulator", *Optics Express*, vol. 18, no. 2, pp. 1667–1676, 2010.

[114] K. Kashiwagi, Y. Nakajima, M. Wada, S. Okubo, and H. Inaba, "Multi-branch fiber comb with relative frequency uncertainty at 10- 20 using fiber noise difference cancellation", *Optics Express*, vol. 26, no. 7, pp. 8831–8840, 2018.

[115] B. Washburn, W. C. Swann, and N. R. Newbury, "Response dynamics of the frequency comb output from a femtosecond fiber laser", *Optics express*, vol. 13, no. 26, pp. 10 622–10 633, 2005.

[116] C.-C. Lee, C Mohr, J Bethge, *et al.*, "Frequency comb stabilization with bandwidth beyond the limit of gain lifetime by an intracavity graphene electro-optic modulator", *Optics Letters*, vol. 37, no. 15, pp. 3084–3086, 2012.

[117] W Hänsel, M Giunta, M Lezius, M Fischer, and R. Holzwarth, "Electro-optic modulator for rapid control of the carrier-envelope offset frequency", in *2017 Conference on Lasers and Electro-Optics (CLEO)*, IEEE, 2017, pp. 1–2.

[118] S. Hakobyan, V. J. Wittwer, K. Gürel, A. S. Mayer, S. Schilt, and T. Südmeyer, "Carrier-envelope offset stabilization of a ghz repetition rate femtosecond laser using opto-optical modulation of a sesam", *Optics Letters*, vol. 42, no. 22, pp. 4651–4654, 2017.

[119] K. Gürel, S. Schilt, and T. Südmeyer, "Carrier-envelope offset frequency stabilization of a fiber laser by cross gain modulation", *IEEE Photonics Journal*, vol. 10, no. 2, pp. 1–6, 2018.

[120] W. Liu, D. N. Schimpf, T. Eidam, *et al.*, "Pre-chirp managed nonlinear amplification in fibers delivering 100 w, 60 fs pulses", *Optics letters*, vol. 40, no. 2, pp. 151–154, 2015.

[121] D. Luo, Y. Liu, C. Gu, *et al.*, "High-power yb-fiber comb based on pre-chirped-management self-similar amplification", *Applied Physics Letters*, vol. 112, no. 6, p. 061 106, Feb. 2018, Publisher: AIP Publishing. DOI: 10.1063/1.5012100.

[122] J. Zhao, W. Li, C. Wang, Y. Liu, and H. Zeng, "Pre-chirping management of a self-similar yb-fiber amplifier towards 80 w average power with sub-40 fs pulse generation", *Optics Express*, vol. 22, no. 26, pp. 32 214–32 219, 2014.

[123] I. Hartl, M. E. Fermann, T. R. Schibli, *et al.*, "Passive cavity enhancement of a femtosecond fiber chirped pulse amplification system to 204w average power", in *Advanced Solid-State Photonics*, Journal Abbreviation: Advanced Solid-State Photonics, Optical Society of America, 2007, WA4. DOI: 10.1364/assp.2007.wa4.

[124] M. E. Fermann and I. Hartl, "Ultrafast fiber laser technology", *IEEE Journal of Selected Topics in Quantum Electronics*, vol. 15, no. 1, pp. 191–206, 2009, Publisher: IEEE, ISSN: 1077-260X. DOI: 10.1109/jstqe.2008.2010246.

[125] A. Klenke, S. Breitkopf, M. Kienel, *et al.*, "530 w, 13 mJ, four-channel coherently combined femtosecond fiber chirped-pulse amplification system", *Optics Letters*, vol. 38, no. 13, p. 2283, Jun. 2013, Publisher: The Optical Society. DOI: 10.1364/ol.38.002283.

[126] E. Shestaev, S. Hädrich, N. Walther, *et al.*, "Carrier-envelope offset stable, coherently combined ytterbium-doped fiber cpa delivering 1 kw of average power", *Optics Letters*, vol. 45, no. 23, pp. 6350–6353, 2020.

[127] P. Balla, H. Tünnermann, S. H. Salman, *et al.*, "Ultrafast serrodyne optical frequency translator", *Nature Photonics*, pp. 1–6, 2022.

[128] R. Paschotta, J. Nilsson, A. C. Tropper, and D. C. Hanna, "Ytterbium-doped fiber amplifiers", *IEEE Journal of quantum electronics*, vol. 33, no. 7, pp. 1049–1056, 1997.

[129] M. E. Fermann and I. Hartl, "Ultrafast fiber laser technology", *IEEE Journal of Selected Topics in Quantum Electronics*, vol. 15, no. 1, pp. 191–206, 2009.

[130] S. Radmard, A. Moshaii, and K. Pasandideh, "400 w average power q-switched yb: Yag thin-disk-laser", *Scientific Reports*, vol. 12, no. 1, p. 16 918, 2022.

[131] E Caracciolo, A Guandalini, F Pirzio, *et al.*, "High power yb: Calgo ultrafast regenerative amplifier for industrial application", in *Solid State Lasers XXVI: Technology and Devices*, SPIE, vol. 10082, 2017, pp. 284–289.

[132] J. Dai, C. Shen, N. Liu, *et al.*, "10 kw-level output power from a tandem-pumped yb-doped aluminophosphosilicate fiber amplifier", *Optical Fiber Technology*, vol. 67, p. 102 738, 2021.

[133] V. Shumakova, V. F. Pecile, J. Fellinger, *et al.*, "Spectrally tunable high-power yb: Fiber chirped-pulse amplifier", *Photonics Research*, vol. 10, no. 10, pp. 2309–2316, 2022.

[134] C. Jauregui, C. Stihler, and J. Limpert, "Transverse mode instability", *Advances in Optics and Photonics*, vol. 12, no. 2, pp. 429–484, 2020.

[135] M. M. Johansen, M. Laurila, M. D. Maack, *et al.*, "Frequency resolved transverse mode instability in rod fiber amplifiers", *Optics Express*, vol. 21, no. 19, pp. 21 847–21 856, 2013.

[136] L Neuhaus, R Metzdorff, S Chua, *et al.*, "Pyrpl (python red pitaya lockbox)-an open-source software package for fpga-controlled quantum optics experiments", in *European Quantum Electronics Conference*, Optica Publishing Group, 2017, EA_P_8.

[137] S Goloboroko, G Grygiel, O Hensler, V Kocharyan, K Rehlich, and P Shevtsov, "Doocs: An object-oriented control system as the integrating part for the ttf linac", in *Proceedings of ICALEPCS*, vol. 97, 1997, p. 141.

[138] P. Duval, "Tine: An integrated control system for hera", 1999.

[139] P Booker, O De Varona, M Steinke, P Wessels, J Neumann, and D Kracht, "Experimental and numerical study of interlock requirements for high-power eydfas", *Optics Express*, vol. 28, no. 21, pp. 31 480–31 486, 2020.

[140] P Micke, T Leopold, S. King, *et al.*, "Coherent laser spectroscopy of highly charged ions using quantum logic", *Nature*, vol. 578, no. 7793, pp. 60–65, 2020.

[141] N. Picqué and T. W. Hänsch, "Frequency comb spectroscopy", *Nature Photonics*, vol. 13, no. 3, pp. 146–157, 2019.

[142] D. T. Yordanov, L. V. Rodríguez, D. L. Balabanski, *et al.*, "Structural trends in atomic nuclei from laser spectroscopy of tin", *Communications physics*, vol. 3, no. 1, p. 107, 2020.

[143] J. J. Krauth, K. Schuhmann, M. A. Ahmed, *et al.*, "Measuring the α-particle charge radius with muonic helium-4 ions", *Nature*, vol. 589, no. 7843, pp. 527–531, 2021.

[144] J. Moreno, F. Schmid, J. Weitenberg, *et al.*, "Toward xuv frequency comb spectroscopy of the 1 s–2 s transition in he+", *The European Physical Journal D*, vol. 77, no. 4, p. 67, 2023.

[145] J. Tuli, *National nuclear data center: Nuclear wallet cards*, 2011.

[146] B. Seiferle, L. von der Wense, P. V. Bilous, *et al.*, "Energy of the 229th nuclear clock transition", *Nature*, vol. 573, no. 7773, pp. 243–246, 2019.

[147] A Yamaguchi, H Muramatsu, T Hayashi, *et al.*, "Energy of the th 229 nuclear clock isomer determined by absolute γ-ray energy difference", *Physical review letters*, vol. 123, no. 22, p. 222 501, 2019.

[148] T. Sikorsky, J. Geist, D. Hengstler, *et al.*, "Measurement of the th 229 isomer energy with a magnetic microcalorimeter", *Physical Review Letters*, vol. 125, no. 14, p. 142 503, 2020.

[149] L. von der Wense and C. Zhang, "Concepts for direct frequency-comb spectroscopy of 229m th and an internal-conversion-based solid-state nuclear clock", *The European Physical Journal D*, vol. 74, pp. 1–17, 2020.

[150] R. C. Cumming, "The serrodyne frequency translator", *Proceedings of the IRE*, vol. 45, no. 2, pp. 175–186, 1957.

[151] A.-L. Viotti, M. Seidel, E. Escoto, *et al.*, "Multi-pass cells for post-compression of ultrashort laser pulses", *Optica*, vol. 9, no. 2, pp. 197–216, 2022.

[152] M. Müller, J. Buldt, H. Stark, C. Grebing, and J. Limpert, "Multipass cell for high-power few-cycle compression", *Optics Letters*, vol. 46, no. 11, pp. 2678–2681, 2021.

[153] M. Hanna, F. Guichard, N. Daher, Q. Bournet, X. Délen, and P. Georges, "Nonlinear optics in multipass cells", *Laser & Photonics Reviews*, vol. 15, no. 12, p. 2 100 220, 2021.

[154] L. M. Johnson and C. H. Cox, "Serrodyne optical frequency translation with high sideband suppression", *Journal of lightwave technology*, vol. 6, no. 1, pp. 109–112, 1988.

[155] J. Buldt, M. Müller, R. Klas, T. Eidam, J. Limpert, and A. Tünnermann, "Temporal contrast enhancement of energetic laser pulses by filtered self-phase-modulation-broadened spectra", *Optics Letters*, vol. 42, no. 19, pp. 3761–3764, 2017.

[156] P. Balla, A. B. Wahid, I. Sytcevich, *et al.*, "Postcompression of picosecond pulses into the few-cycle regime", *Optics letters*, vol. 45, no. 9, pp. 2572–2575, 2020.

[157] C. Heyl, C. Arnold, A. Couairon, and A. L'Huillier, "Introduction to macroscopic power scaling principles for high-order harmonic generation", *Journal of Physics B: Atomic, Molecular and Optical Physics*, vol. 50, no. 1, p. 013 001, 2016.

[158] E. Peik, T. Schumm, M. Safronova, A. Palffy, J. Weitenberg, and P. G. Thirolf, "Nuclear clocks for testing fundamental physics", *Quantum Science and Technology*, vol. 6, no. 3, p. 034 002, 2021.

[159] R. W. Drever, J. L. Hall, F. V. Kowalski, *et al.*, "Laser phase and frequency stabilization using an optical resonator", *Applied Physics B*, vol. 31, pp. 97–105, 1983.

[160] T. Allison, A Cingöz, D. Yost, and J Ye, "Extreme nonlinear optics in a femtosecond enhancement cavity", *Physical Review Letters*, vol. 107, no. 18, p. 183 903, 2011.

[161] B. Franzke, "The heavy ion storage and cooler ring project esr at gsi", *Nuclear Instruments and Methods in Physics Research Section B: Beam Interactions with Materials and Atoms*, vol. 24, pp. 18–25, 1987.

[162] E. Tkalya and A. Nikolaev, "Magnetic hyperfine structure of the ground-state doublet in highly charged ions th 89+, 87+ 229 and the bohr-weisskopf effect", *Physical Review C*, vol. 94, no. 1, p. 014 323, 2016.

[163] V. Shabaev, D. Glazov, A. Ryzhkov, *et al.*, "Ground-state g factor of highly charged th 229 ions: An access to the m1 transition probability between the isomeric and ground nuclear states", *Physical Review Letters*, vol. 128, no. 4, p. 043 001, 2022.

[164] C Trageser, C Brandau, C Kozhuharov, *et al.*, "A new data acquisition system for schottky signals in atomic physics experiments at gsi's and fair's storage rings", *Physica Scripta*, vol. 2015, no. T166, p. 014 062, 2015.

[165] L. von der Wense and B. Seiferle, "The 229 th isomer: Prospects for a nuclear optical clock", *The European Physical Journal A*, vol. 56, no. 11, p. 277, 2020.

[166] P. Thirolf, B Seiferle, and L Von der Wense, "The 229-thorium isomer: Doorway to the road from the atomic clock to the nuclear clock", *Journal of Physics B: Atomic, Molecular and Optical Physics*, vol. 52, no. 20, p. 203 001, 2019.

Acknowledgements

During my PhD studies I met, worked with and received help from so many people at DESY, Universität Hamburg and Helmholtz Institute Jena that I cannot thank them enough. First and foremost I am extremely grateful to my supervisor Dr. Christoph M. Heyl for his guidance, constant support, patience and understanding. His vast knowledge and experience have encouraged and guided me during my academic research and daily life. I am also grateful to Prof. Dr. Franz X. Kärtner, who agreed to be my supervisor and enthusiastically contributed to the development of the project and the thesis.

I would like to thank Dr. Ingmar Hartl, who not only accepted me into his group, but also played the role of a teacher and guided me throughout my PhD. I consider myself lucky to have met Dr. Christoph Mahnke and Arthur Schönberg, who have always supported me unwaveringly in my academic and everyday life and broadened my horizons with their brilliant ideas and expertise.

I would like to thank Dr. Mingqi Fan and Prannay Balla, together we shouldered the weight of this heavy project and made it happen. It has been a great experience working and sharing office and lab space with Henrik Schygulla, Dominic Laumer, Yannick Schrödel, Önder Akcaalan, Chen Li, Dr. Henrik Tünnermann, Dr. Vinicius Silva de Oliveira and Dr. Hongwen Xuan. Thank you for making this 4.5 year process fun and keeping me sane.

I would like to mention and thank Dr. Yuxuan Ma, Dr. Yi Hua, Dr. Oliver Heckl and his group, as well as Dr. Gil Porat and his group for fruitful discussions. In addition, I would like to extend my sincere thanks to all my colleagues in the FS-LA group, especially the electronics team, for their assistance, support and understanding. I would also like to acknowledge Prof. Dr. Thomas Stöhlker and Dr. Carsten Brandau for offering me to be part of an exciting experiment at GSI.

Lastly, but most importantly, I would like to express my gratitude to my parents and my sister. Although we are far away from each other, I have always felt their support, without which it would have been impossible for me to complete my studies.

List of publications

Publications in peer-reviewed journals - first author

1. H. S. Salman, A. Bacıoğlu, S. K. Eken, "Crystallization of hydrogenated amorphous silicon thin film on glass by using ns-pulsed fiber laser operating at 1064 nm," *Materials Science in Semiconductor Processing*, vol. 95, pp. 20-27, 2019.

2. S. Salman, Y. Ma, K. Gürel, S. Schilt, C. Li, P. Pfäfflein, *et al.*, "Comparison of two low-noise CEO frequency stabilization methods for an all-PM Yb: fiber NALM oscillator," *OSA Continuum*, vol. 4, no. 6, pp. 1889-1896, 2021.

3. Manuscript in preparation: S. Salman, M. Fan, H. Tünnermann, P. Balla, *et al.*, "Tunable High-Power Frequency comb driver for VUV + XUV comb spectroscopy,"

Publications in peer-reviewed journals

1. E. A. Kipergil, A. Demirkiran, N. Uluc, S. Yavas, T. Kayikcioglu, S. Salman, *et al.*, "Development of a fiber laser with independently adjustable properties for optical resolution photoacoustic microscopy," *Scientific reports*, vol. 6, no. 1, pp. 38674, 2016.

2. V. Türker, M. E. Yağcı, S. H. Salman, *et al.*, "A Dual-Wavelength Pulsed Laser Processing Platform for a-Si Thin Film Crystallization," *Instruments*, vol. 3, no. 2, pp. 31, 2019.

3. A. S. Mayer, W. Grosinger, J. Fellinger, G. Winkler, L. W. Perner, S. Droste, H. S. Salman, *et al.*, "Flexible all-PM NALM Yb: fiber laser design for frequency comb applications: operation regimes and their noise properties," *Optics express*, vol. 28, no. 13, pp. 18946-18968, 2020.

4. Y. Ma, S. H. Salman, C. Li, C. Mahnke, Y. Hua, S. Droste, *et al.*, "Compact, all-PM fiber integrated and alignment-free ultrafast Yb: fiber NALM laser with sub-femtosecond timing jitter," *Journal of Lightwave Technology*, vol. 39, no. 13, pp. 4431-4438, 2021.

5. C. Mahnke, Y. Hua, Y. Ma, S. Salman, T. Lamb, S. Schulz, *et al.*, "Long-term stable, synchronizable, low-noise picosecond Ho: fiber NALM oscillator for Ho: YLF amplifier seeding," *Optics Letters*, vol. 47, no. 4, pp. 822-825, 2022.

6. V. Shumakova, V. F. Pecile, J. Fellinger, M. Leskowschek, P. E. C. Aldia, A. S. Mayer, L. W. Perner, S. Salman, *et al.*, "Spectrally tunable high-power Yb: fiber chirped-pulse amplifier," *Photonics Research*, vol. 10, no. 10, pp. 2309-2316, 2022.

7. P. Balla, H. Tünnermann, S. H. Salman, M. Fan, *et al.*, "Ultrafast serrodyne optical frequency translator," *Nature Photonics*, vol. 17, no. 2, pp. 187-192, 2023.

8. A. Schönberg, H. S. Salman, A. Tajalli, S. Kumar, I. Hartl, *et al.*, "Below-threshold harmonic generation in gas-jets for Th-229 nuclear spectroscopy," *Optics Express*, vol. 31, no. 8, pp. 12880-12893, 2023.

9. D. Laumer, S. Salman, Y. Ma, K. T. Zawilski, *et al.*, "Sub-Hz relative linewidths from an interferometrically stabilized mid-infrared frequency comb," *Optics Letters*, vol. 48, no. 48, pp. 3055-3058, 2023.

Conference publications - first author

1. S. Salman, Y. Ma, K. Gürel, S. Schilt, *et al.*, "Comparison of two low-noise CEP stabilization methods for an environmentally stable Yb:fiber oscillator," *Laser Congress 2019 (ASSL, LAC, LS&C)*, OSA Technical Digest (Optica Publishing Group, 2019), paper JTu3A.17, 2019.

2. S. Salman, M. Fan, H. Tünnermann, P. Balla, *et al.*, "Smart and agile 84 W fs Yb-fiber laser for spectroscopy," *Conference on Lasers and Electro-Optics*, Technical Digest Series (Optica Publishing Group, 2022), paper SF2M.1, 2022.

3. S. Salman, M. Fan, H. Tünnermann, P. Balla, *et al.*, "Smart and agile 88 W Yb-fiber frequency comb laser," *European Physical Journal Web of Conferences, EPS-QEOD Europhoton Conference*, vol. 267, pp. 01057, 2022.